

INFORMATION TO USERS

This manuscript has been reproduced from the microfilm master. UMI films the text directly from the original or copy submitted. Thus, some thesis and dissertation copies are in typewriter face, while others may be from any type of computer printer.

The quality of this reproduction is dependent upon the quality of the copy submitted. Broken or indistinct print, colored or poor quality illustrations and photographs, print bleedthrough, substandard margins, and improper alignment can adversely affect reproduction.

In the unlikely event that the author did not send UMI a complete manuscript and there are missing pages, these will be noted. Also, if unauthorized copyright material had to be removed, a note will indicate the deletion.

Oversize materials (e.g., maps, drawings, charts) are reproduced by sectioning the original, beginning at the upper left-hand corner and continuing from left to right in equal sections with small overlaps.

Photographs included in the original manuscript have been reproduced xerographically in this copy. Higher quality 6" x 9" black and white photographic prints are available for any photographs or illustrations appearing in this copy for an additional charge. Contact UMI directly to order.

**ProQuest Information and Learning
300 North Zeeb Road, Ann Arbor, MI 48106-1346 USA
800-521-0600**

UMI[®]

An Investigation into Pulsating Aurora

John Denis Williams

**A dissertation submitted in partial fulfillment
of the requirements for the degree of**

Doctor of Philosophy

University of Washington

2002

Program Authorized to Offer Degree: Geophysics

UMI Number: 3041071

UMI[®]

UMI Microform 3041071

Copyright 2002 by ProQuest Information and Learning Company.
All rights reserved. This microform edition is protected against
unauthorized copying under Title 17, United States Code.

ProQuest Information and Learning Company
300 North Zeeb Road
P.O. Box 1346
Ann Arbor, MI 48106-1346

In presenting this dissertation in partial fulfillment of the requirements for the Doctorial degree at the University of Washington, I agree that the Library shall make its copies freely available for inspection. I further agree that extensive copying of this thesis is allowable only for scholarly purposes, consistant with "fair use" as prescribed in the U.S. Copyright Law. Requests for copying or reproduction of this dissertation may be referred to University Microfilms, 1490 Eisenhower Place, P.O. Box 975, Ann Arbor, MI 48106, to whom the author has granted "the right to reproduce and sell (a) copies of the manuscript in microform and/or (b) printed copies of the manuscript made from microform."

Signature John Williams

Date March 21, 2002

University of Washington

Graduate School

This is to certify that I have examined this copy of a doctoral dissertation by

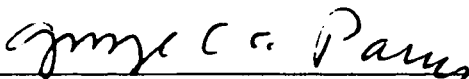
John Denis Williams

and have found that it is complete and satisfactory in all respects,

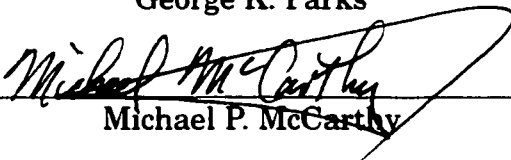
and that any and all revisions required by the final

examining committee have been made.

Co-Chairs of Supervisory Committee:

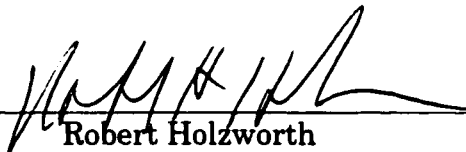


George K. Parks



Michael P. McCarthy

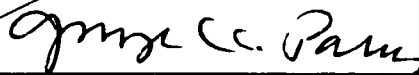
Reading Committee:



Robert Holzworth



Michael P. McCarthy



George K. Parks



Robert M. Winglee

Date:

MARCH 21, 2002

University of Washington

Abstract

An Investigation into Pulsating Aurora

by John Denis Williams

Co-Chairs of Supervisory Committee

Professor George K. Parks

Geophysics

Professor Michael P. McCarthy

Geophysics

On March 13, 1997 a sounding rocket equipped to study pulsating aurora was launched into the recovery phase of a small magnetic substorm. The launch originated from Poker Flat, Alaska and moved northward, reaching a apogee of 385 km and crossing field lines from $L = 5.6$ to $L = 8$. This sounding rocket was the first to have instruments designed to measure the upgoing and downgoing electron precipitation in the region over a pulsating auroral event. Nine pulsations were observed during the course of the 10 minute flight.

This dissertation discusses the design, fabrication and calibration of the particle detection instruments, which include solid state telescopes (SST's) and an electrostatic analyzer (ESA). Observations led to an inferred parallel electric field above the rocket, the first time such a field had been associated with pul-

sating aurora. The data showed that there were no pulsations for electrons with energies less than 5 keV for pitch-angles between 22° and 90° but pulsations were seen for electrons from 5 keV down to 1 keV for field aligned precipitating electrons and for all upgoing electrons. Furthermore, the greatest change between background and pulsation occurred for electrons between 10 and 20 keV with pitch-angles between 50° and 90° . Observations also showed anomalous pitch-angle distributions, with larger than expected fluxes of high energy electrons leaving the ionosphere. Also missing from the data is evidence of either velocity dispersed arrival of electrons or 3 Hz oscillations.

The data analysis of the measurements provided many new insights into pulsating aurora and has raised questions about the source of the pulsating mechanism and the mechanism itself. The data are compared to three current theoretical models and we find that they cannot adequately describe the observations. Other models are discussed and also discarded as being unable to explain all of the observations.

TABLE OF CONTENTS

List of Figures	iv
List of Tables	vii
Chapter 1: Introduction	1
1.1 Optical Observations and Characteristics of Pulsating Aurora . . .	2
1.2 In-Situ Observations and Characteristics of Pulsating Aurora . . .	4
1.3 Theoretical Models of Pulsating Aurora	10
1.4 Scope of This Dissertation	15
Chapter 2: Rocket Instrumentation	18
2.1 Instrument Counts and Particle Flux	18
2.2 Solid State Telescopes	21
2.3 Electrostatic Analyzer	25
Chapter 3: Electron Data Analysis	32
3.1 Rocket Flight and Data Summary	32
3.2 Differential Energy Spectra and Pitch-angle Distributions	37

3.3	Low Energy Electrons ($20 \text{ eV} < E < 1 \text{ keV}$)	42
3.4	Discussion of Low Energy Electron Observations	46
3.5	Intermediate Energy Electrons ($1 \text{ keV} < E < 5 \text{ keV}$)	51
3.6	Discussion of Intermediate Energy Electrons	54
3.7	High Energy Electrons ($E > 5 \text{ keV}$)	56
3.8	Maxwellian Fits to the High Energy Electrons	63
3.9	Discussion of High Energy Electron Observations	67
3.10	Velocity Dispersion	71
3.11	Three Hertz Modulation	75
3.12	Summary of Observations	77
Chapter 4: Evaluation of Pulsation Models and Requirements for A Physically Meaningful Model		81
4.1	Electron Cyclotron Wave-Particle Interactions	81
4.2	DC Electric Field	91
4.3	What a Model Must Incorporate	92
Chapter 5: Summary and Conclusions		99
5.1	Results	99
5.2	Further Research	100

Bibliography	102
Appendix A: Solid State Telescope Geometric Factor	109
Appendix B: Particle Flux, Distribution Functions and Moments	119
Appendix C: Solid State Telescope Electronics	134
Appendix D: Temporal Versus Spatial Dynamics	145
Appendix E: X-rays Produced by Bremsstrahlung	147
Appendix F: Local Production of Electrons	150
Index	154

LIST OF FIGURES

2.1	Block diagram of the solid state telescope electronic components .	24
2.2	Azimuthal scan of the Electrostatic Analyzer	29
3.1	Magnetic Field Components as Measured on the Ground	33
3.2	UltraViolet Imager(UVI) images during the rocket launch	34
3.3	Flight energy flux and pitch angle spectrogram	36
3.4	Plot of Distribution Function for Pulsation at 146 s and Back-ground at 135 s	38
3.5	Electron flux summary plot	40
3.6	Energy Spectra for the Particle Precipitation at 135 s and 146 s After Launch	41
3.7	Particle Flux as a Function of Time and Pitch-angle	43
3.8	Low energy spectra for pulsation and background	45
3.9	Pitch-angle Distribution of the Pulsation at 146 s and the Un-structured Background at 135 s	46
3.10	Particle Flux as a Function of Time for Different Pitch-angles . .	52

3.11 Intermediate Energy Spectra for Pulsation at 146 s and Background at 135 s	53
3.12 Intermediate Pitch-angle Distribution for Pulsation at 146 s and Background at 135 s	55
3.13 Particle Flux as a Function of Time and Pitch-angle for Selected Energies	57
3.14 Energy Spectra for electrons of $E > 5$ keV	58
3.15 High Energy Pitch-angle Distribution for Pulsation at 146 s and Background at 135 s	59
3.16 Ratio of the flux at 90° to 0° for the pulsation at 146 s	61
3.17 Plot of Anisotropy versus Time for Selected Energies	62
3.18 Energy Flux Difference as a function of Pitch-angle and Energy .	64
3.19 Difference Pitch-angle Distribution for Pulsation at 146 s	65
3.20 Energy Spectra of Pulsation and Background with Difference . .	66
3.21 Particle Flux Time series Showing Two Pulsations	72
3.22 Cross Correlation of two Energies for the Pulsation at 146 Seconds After Launch	73
3.23 Particle Flux versus time (highest resolution) for Pulsation at 146 s	76
3.24 Power spectral density estimate from 115 s to 200 s after launch	78

4.1 Resonant Energy as a function of Frequency for Various Number Densities	87
4.2 Resonant Energy as a function of Frequency for Various Latitudes	89
4.3 Power Law Parameter for Low Energy Electrons	93
A.1 Geometry of Solid State Telescope Field of View	110
D.1 Correlation between optical emissions and electron measurements	146
F.1 Electron transport model flux summary plot	152
F.2 Differential particle flux at 380 km	153

LIST OF TABLES

1.1	Table of Previous Pulsation Observations	11
2.1	ESA geometric factor as a function of rocket spin angle	31
3.1	Table of Characteristic Energy for all the Pulsations	68
4.1	Table of Number Density and Resulting Latitudes	88
C.1	The Preamp Charge Gains	135
C.2	0° detector energy bin setup	139
C.3	22.5° detector energy bin setup	140
C.4	45° detector energy bin setup	141
C.5	67.5° detector energy bin setup	142
C.6	90° detector energy bin setup	143
C.7	Proton detector energy bin setup	144

ACKNOWLEDGMENTS

There are many, many people I would like to thank. The completion of this work would not have been possible without the constant help and support of Dr. George Parks. George has given me the time to make mistakes and to learn from them. I have learned a great deal from you and will carry it with me for the rest of my life. To Dr. Michael McCarthy I owe a tremendous debt of gratitude. Michael have always been willing to go into the deep details, the subtleties, which is where the final data results were hidden. Dr. McCarthy's scientific method and attitude and deep knowledge have been a revelation to me and an inspiration.

I would like to thank the reading committee for their input and support. Dr. Robert Winglee was always willing to discuss science and theory and always had a happy outlook and a laugh. Robert was especially supportive and a pleasure to work with. Dr. Robert Holzworth was also very supportive and always willing to discuss science and some of the other things going on around the workplace.

Dr. Ruth Skoug has been a special help to me. She was also willing to discuss science and the nitty gritty details that were so necessary for getting the experiment to work correctly. She has been a friend and listened to my endless complaining and always had a smile for me.

The graduate students were a great bunch of people and I learned much from all of them. I would like to specifically thank my officemates, Dr. Ben Barnum, Dr. Kerry Deutsch, Dr. Kirsten Lorentzen and Andrew Meadows. You all have been awesome friends and I have enjoyed all of the discussions, both science and otherwise. I would also like to take this time to thank Dr. Laura Peticolas for her unfailing good spirits and excellent knowledge of auroral physics and electron transport, you have been a good friend. Dr. Curt Szuberla has been a constant source of fun and knowledge and I have learned many things from you.

Other graduate students and faculty members I would like to mention are Bill Schultz and Dr. LiJen Chen. Bill did most of the construction and calibration of the electrostatic analyzer and without his work this thesis would not be what it is. LiJen has been a remarkable example and friend who has always had a smile and a kind word. Dr. Bill Peria has been an excellent source of science and techniques and has always been willing to listen to my crazy theories and help me make them better, Bill you are an excellent scientist. I would also like to thank Dr. Mitch Brittnacher for your support and all of the work you did for George with respect to administering all of the grants. I would like to thank Liz MacDonald for her help and involvement in the particle data analysis as well as the work she did to make the rocket launch a success. She was always there to catch my mistakes and gently show me my errors. Finally I would like to take the time to thank John Chin for the work and attention to detail you give to all you do.

There are many other people who did not help directly in the production of this thesis but who were helpful in keeping me sane and happy. My sojourn

here in Seattle has taught me a great deal aside from just a whole lot of science and these are some of the people who are responsible for teaching me so many things. Firstly, I would like to thank the young adults from St. Benedict's Church. They have all been wonderful friends and huge supporters in my quest. I would like to thank Fr. Paul, you have been an inspiration and a blessing. Specifically I thank Suzanne Long, Dr. Denise Ferkey, Addy Froehlich, Cindy Ann and Brad Belanger, Sandra Matthews, Jason Amann, Erin Barry, Diane Reischling, Paul Hezel, June Gill, David Losoya, Rebecca and Mike Casson, Andie and Patty Miller, Dr's Kerry and Eric Deutsch, both young adults and fellow scientists. There are a few others who have been great friends. I would like to thank Molli Nordlund and Pat Kiser, I miss you both. I would like to thank Annie Yakshaw for unfailing good humor and providing a great place to live when I really, really needed it. I would like to also thank Catherine Shehan for constant support both from Seattle and from Virginia. Finally, I would like to thank Kim Follett for her help and support and understanding and patience.

I gratefully thank the members of my family. Mar and Mike and Tree and Frank and Mike and Jean and Matt, you have all been supportive and loving and I couldn't have done it without you. A big part of this achievement belongs to you. Revel in it with me.

Finally I thank God for all of the graces and strength to get me to where I am today.

DEDICATION

**In loving memory of my mother
Anna Patricia Williams
June 9, 1936 – July 18, 2000**

Chapter 1

INTRODUCTION

Lights in the polar sky have been observed for centuries. The visual displays in different colors and shapes, moving across the sky have filled people with such awe and wonder that the lights were considered to be signs from the gods. In recent years humans have begun the systematic study of these lights, called the aurora Borealis in the northern hemisphere and aurora Australis in the southern hemisphere.

Researchers have organized the visual aurora into different types. These types are often observed at similar local times and are related to the regions of space which are connected to the sky above the observer. Perhaps the most visually exciting case is the auroral breakup. This phenomenon is often seen around local midnight when the observer is in the most anti-sunward position and the sky above is connected to the magnetic lines of force that go back into the geomagnetic tail. The breakup is characterized by a sudden expansion of rapidly moving, bright displays of green and red emissions. Many wave-like forms and columns are observed during the midnight breakup and the physical causes of this phenomenon are extremely complicated and difficult to understand. The auroral breakup is composed of forms that are called discrete. These forms typically have strongly defined borders and are limited in size. Another common

type of auroral display is made up of diffuse aurora. The diffuse aurora does not have clearly defined shapes and may or may not have obvious borders.

Pulsating aurora is a kind of diffuse aurora with weak borders and will be the study of this dissertation. This auroral type is important because of the length in time of its occurrence and the amount of energy that it deposits into the ionosphere. The study of pulsating aurora has led to understanding of how electrons can, in general, be caused to precipitate into the ionosphere on the morning side and will be a major focus of the work in this dissertation.

1.1 Optical Observations and Characteristics of Pulsating Aurora

Pulsating aurora is a very beautiful and complex phenomena. During a pulsating auroral event the sky is filled with regions of light that can take the form of patches or arcs and can cover the entire sky or just small portions of it. The light seen from pulsating forms turns on and off in a quasi-periodic fashion. The generally accepted time periods [Johnstone, 1978] for the on to off cycle range from 2 seconds to 30 seconds. The on and off cycles are not sinusoidal in nature, rather the on period is often shorter than the off period.

Imposed on the slowly varying emissions of pulsating aurora is a more rapidly varying emission. This emission ranges from 2 to 10 Hz and is often simply called the 3 Hz modulation. This modulation is seen in 50 percent of all ground based pulsating auroral observations [Røyrvik and Davis, 1977] and are associated mostly with patch-like structures. One characteristic feature of pulsating patches is that they can illuminate from a central source. That is, the patch will grow in size from a single point and then shrink back in size until it becomes a single point. This form of pulsating aurora is called streaming by Cresswell

[1968] and happens fairly regularly [*Røyvrik and Davis, 1977*].

Pulsating aurora is typically a morning-side phenomena. The displays can be seen anytime from local midnight until dawn. In many instances a pulsating event will start shortly after an auroral breakup. They occur from 60° to 75° latitude and are usually found to the equator-ward side of any previous display [*Johnstone, 1978*]. The typical characteristic energy of electrons that precipitate during a pulsation event is around 8 – 10 keV and the events themselves last for upwards of several hours. The combination of the high characteristic energy and the long duration results in a significant amount of energy being deposited into the auroral ionosphere. Due to the high characteristic energy of the electrons, the emissions often occur at an altitude of 80 to 100 km, whereas for discrete aurora (which involve lower energy electrons, a few keV), the emission height is around 120 km.

Another interesting feature of some pulsating auroral forms is that many observations have shown them to be emitting in a very narrow altitude region, in some cases on the order of 2 km or less [*Stenbaek-Nielsen and Hallinan, 1979*]. Given the exponential decrease in particle density in the atmosphere, a monoenergetic beam of particles traveling into the ionosphere will deposit its energy over the range of at least 30 km [*Rees, 1989*]. The fact that observations show a much smaller emission thickness is unexplained by current theories. There also appears to be a connection between thin vertical auroral forms and streaming [*Stenbaek-Nielsen and Hallinan, 1979*], as if electrons precipitating into the ionosphere are trapped into a thin vertical region and must spread out from a point horizontally.

The energetic precipitating electrons rarely penetrate deeper into the atmosphere than 80 km. Hence, the most practical way to measure the energy

spectra and pitch-angle distributions is to send rocket instruments up into the ionosphere. The next section will review briefly some of the sounding rocket observations made of pulsating aurora during the past 30 years.

1.2 In-Situ Observations and Characteristics of Pulsating Aurora

Rocket observations are an excellent way of obtaining information about the phenomenon of pulsating aurora. Typical flights last about 10 minutes and result with 8 minutes or less of usable data. Overall though, much of the quantitative information known about pulsating aurora has been made by sounding rocket experiments. That quantitative information is the electron or proton flux as a function of time, energy and pitch-angle. All of the rocket measurements of pulsating aurora mention a combination of some or all of these quantities. Particle flux is determined from the count rate which is the actual measurement of the number of particles that hit the detector. In the case of pulsating aurora, abrupt changes in the particle flux are taken to indicate a pulsation event. In general, the change in flux between a pulsation and the unstructured background precipitation can range from 10 to 100 percent [*Nemzek et al.*, 1995].

The Canadian Pulsating Auroral Campaign was designed expressly to determine the relationship between optical emissions and particle precipitation. A series of flights [*Yau et al.*, 1981; *McEwen et al.*, 1981] were launched into the ionosphere directly above pulsating aurora with the idea of seeing the correlation between the two phenomena. The results showed that the electrons that precipitate into the ionosphere are directly responsible for the time varying emissions observed on the ground. Without these results it is not at all clear that the observations made by rocket instrumentation is correlated with the optical observations which had been made for decades.

1.2.1 Energy Spectra

Most of the work done on rocket launches into pulsating aurora include measurements of the energy spectrum and pitch-angle distributions of the precipitating electrons. These quantities give information about the distribution function from which the electrons were sampled. Understanding the distribution function and how it changes allows theories about the causes of pulsating aurora to be developed.

As far as measurements of the electron energy spectra, the general trend indicates that the energy spectra can be split into three different regions, that is, into low, medium and high energies. Low energies ($E < 1$ keV) have never before been observed to pulsate like higher energies. For energies between 1 and 15 keV, where the highest energy flux is usually measured, the energy spectra can be approximated by a Maxwellian. Only *Johnstone* [1971] was able to model the energy spectra as fitting to power law spectra. The characteristic energy of the Maxwellian are found to vary between 1.4 keV and 12 keV [*McEwen et al.*, 1981; *Smith et al.*, 1980]. Above 15 – 20 keV, the spectra are either power law or a kappa distribution [*Johnstone*, 1978]. In all of the different measurements made of pulsating aurora the energy spectra has shown the least amount of variation.

Measurements of proton energy spectra are not as common. *Smith et al.* [1980] has seen proton pulsations in energies only above 26 keV. *Johnstone* [1971] also measured protons (with 2 s time resolution) and found the energy spectra best fit a power law model. *Johnstone* [1971] also found a correlation in the particle flux between low energy ($E < 13$ keV) protons and 10 keV electrons.

The characteristic energy also seems to broaden during a pulsation with chang-

es up to 50 percent between pulsation on times and off times [Smith *et al.*, 1980]. Whalen *et al.* [1971] report that the spectrum softens during a pulsation maximum but most reports state that the spectrum hardens during a pulsation event. Assuming that the energy spectra can be described by a Maxwellian distribution over the range of 5 – 15 keV, these observations indicate the temperature increases during a pulsation as compared to the background precipitation.

1.2.2 Pitch Angle Distributions

A pitch-angle distribution is a way of measuring how the particles are distributed relative to the magnetic field direction. The pitch of a particle is defined as the angle between the velocity \vec{v} of the particle and the magnetic field \vec{B} . A charged particle moving along a field line undergoes circular motion around the magnetic field as well as translational motion along the field. The combination of these two types of motion produces a helical motion. There is a direct analogy between the motion of particles along a magnetic field line and the threads of a screw. The angle of the threads on a screw is called the pitch, thus the angle between \vec{v} and \vec{B} came to be called the pitch-angle.

The information on pitch-angle distributions for pulsating aurora is not as well known as the energy spectral content. Many of the early flights did not have the ability to sample both pitch-angle and energy spectra quickly enough (i.e. on the order of a pulsation period) to be able to say a great deal about how the electrons were distributed in pitch-angle.

In an early rocket flight Bryant *et al.* [1971] reported an isotropic pitch-angle distribution for 4 – 6 keV electrons which became more loss-cone like at higher energies ($E \geq 10$ keV). The loss cone corresponds to the pitch-angle of a particle, that has a high chance of being lost to the atmosphere before it mirrors and

returns back to the equatorial region. An isotropic distribution is one in which the flux at different pitch-angles is equal. A loss-cone type distribution is one in which the flux is peaked at 90° and drops off away from 90° . The losses at 0° and 180° are due to atmospheric absorption. In another flight *Bryant et al.* [1975] reported electron pitch-angle distributions for energies between 3.8 keV and 50 keV which changed little during a pulsation event and which were slightly peaked at 90° .

There is a certain amount of controversy in the measurement of the pitch-angle distribution. *Smith et al.* [1980] report that electrons ($9 \text{ keV} < E < 18 \text{ keV}$) were isotropic throughout the pulsation sequence, while the protons ($2 \text{ keV} < E < 20 \text{ keV}$) were anisotropic. *Whalen et al.* [1971] on the other hand, in observing electrons of energies greater than 24 keV and protons of energies greater than 60 keV, report that the pitch-angle distribution of the protons was isotropic while the lower energy electrons were highly anisotropic and peaked at 90° during non-pulsation time intervals but became isotropic during the peak of the pulsation. *Sandahl* [1984] reports a similar result for energies above 20 keV, while for electrons with energies below 20 keV the distributions are isotropic. Thus, there seems to be unpredictable observations about the change in the pitch-angle distributions during a pulsating event.

1.2.3 3 Hz Oscillations

Sandahl et al. [1980] noted that the 3 Hz oscillation was only seen in precipitating electrons above 25 keV. Relying on theoretical work by *Røyvrik* [1978], *Sandahl et al.* [1980] suggested that the 3 Hz oscillations were produced by whistler mode electromagnetic waves interacting with the precipitating electrons. For precipitating electrons of energy $E < 25 \text{ keV}$, which did not show the

3 Hz oscillations, *Sandahl et al.* [1980] invoked an electrostatic wave-particle interaction. *Lepine et al.* [1980] reported a 2.2 Hz modulation of the electron precipitation for electrons ranging between 4 and 25 keV. However, not all pulsation observations, either on the ground (seen in 50% of the observations) or by rocket (seen in less than 10% of the observations), have shown a 3 Hz modulation and so it is not clear how the modulation fits into any theoretical understanding of the pulsation phenomenon. Still the 3 Hz modulation is for now an unexplained component of pulsating auroral observations and any explanation for pulsating auroral will need to address what causes the 3 Hz modulation and why it is not present in all observations.

1.2.4 Velocity Dispersion

Of the one dozen papers about instruments launched into pulsating aurora, approximately one half are devoted almost exclusively to the topic of velocity dispersion. These observations are important because they allow (with a few simple assumptions) researchers to pinpoint the location of the modulation region, this in turn leads to a simplification of the types of mechanisms which may produce the pulsations. Velocity dispersion, in this sense, means that electrons of different energy arrive at the rocket at different times. For example, if some event caused a sudden flux of electrons into the loss-cone, some of which had a higher energy than others, the ones that traveled the fastest (ones with the highest energies) reach the rocket first. Under the assumption that all of the electrons left the modulation region at the same time and that the modulation region is located at the same place for the different energy electrons, the modulation region can be determined by simply noting the difference in arrival times of the different energy electrons.

This velocity dispersion was first observed for pulsating aurora by *Bryant et al.* [1967]. In at least four other papers [*Bryant et al.*, 1969, 1971, 1975; *Smith et al.*, 1980] the effects of velocity dispersion were examined exhaustively. The consensus of these measurements is that, with the assumptions given above, the source of the particle modulation can be found on or near the geomagnetic equator.

Examples of flights in which no velocity dispersion was observed include the high energy electron measurements in the 1980 flight of *Sandahl* [1984] and the rocket flight of *Johnstone* [1971]. These examples of “dispersionless” electrons show that the situation is likely to be more complicated than the simple assumptions made by *Bryant et al.* [1975]. Possibly there are two different regions which can produce the pulsations, one close to the ionosphere and one at the equatorial plane of the magnetosphere. Another possibility is that different energy electrons interact with different frequency waves at different times in just the right way to result in the electrons arriving at different times.

1.2.5 Summary of Past Observations

The pulsation measurements made by previous sounding rockets show many similar measurements but an equal number of anomalies. Table 1.1 gives information on the pitch-angle and energy spectral observations as well as whether or not velocity dispersion was observed. Not included in this table are the number of satellite measurements that have been made. The similarities in the energy spectral measurements allow pulsating aurora to be described by a Maxwellian distribution for energies between 2 to 25 keV with increasing temperature during the pulsation event itself. The pitch-angle results are not so easy to classify. There appears to be a trend toward isotropy during pulsation

events and when no pulsations are present the background may be isotropic or anisotropic. Given the work of *Bryant et al.* [1969, 1971, 1975] which shows the existence of velocity dispersion, the most probable source location for the modulation is in the equatorial region of the magnetosphere. These observational features have been used to create models which might explain the causes of pulsating aurora. The next section summarizes the basic theoretical understanding about the cause of pulsating aurora.

1.3 Theoretical Models of Pulsating Aurora

There are three theoretical models that are used to explain pulsating aurora. They all depend upon a wave-particle interaction mechanism to initiate the pulsation precipitation but they differ in how the interaction comes about. The wave mode which is invoked is the electron cyclotron “whistler” wave which come into resonance with electrons and results in the scattering of the electrons into the loss cone [*Kennel and Petschek*, 1966]. At typical rocket altitudes, the loss cone was approximately 70 degrees. This means that any electrons at the height of the rocket with pitch-angles of 70 degrees or less are likely to be lost to the atmosphere. The loss cone in the equatorial region which maps to the field line on which our rocket was traveling is calculated to be about 3 degrees using the first invariant. The general idea of the resonant wave-particle interaction is that waves grow or shrink by exchanging energy with the particles, in this case electrons. If the electrons lose or gain enough velocity, then they can move into the loss cone and be precipitated. The wave growth itself is initiated by phase space gradients in the particle distribution function. It is how these phase space gradients are initiated that differentiate the three different models of pulsating aurora.

Table 1.1: Table of previous rocket experiment pulsation observations. Information is given on pitch-angle distributions, energy spectra and velocity dispersion. All information is given for electron measurements unless otherwise noted.

Author	Pitch-angle Distribution	Energy Spectra	Velocity Dispersion
<i>Bryant et al.</i> [1967, 1969]	No information	Electrons at 2, 4 and 10 keV	yes
<i>Bryant et al.</i> [1971]	Isotropic – Loss cone at higher energies	Electrons at 4, 6 and > 22 keV	yes
<i>Bryant et al.</i> [1975]	Isotropic electrons Loss cone at higher energies	Maxwellian $E_0 = 2.5 -$ 3.1 keV	yes
<i>Whalen et al.</i> [1971]	Anisotropic (background) Isotropic (pulsation)	Spectra soften during pulsation	No information
<i>Johnstone</i> [1971]	Isotropic Protons-Low E Loss cone-Protons High E	Power Law $6.8 \times 10^7 E^{0.97}$	No dispersion
<i>Smith et al.</i> [1980]	Isotropic-Electrons Anisotropic-Protons	Maxwellian $E_0 = 4$ keV Min $E_0 = 9$ keV Max	yes
<i>Yau et al.</i> [1981]; <i>McEwen</i> <i>et al.</i> [1981]	Isotropic electrons with some loss cone due to atmospheric losses	Maxwellian $E_0 = 1.6$ keV Min $E_0 = 2$ keV Max	yes
<i>Sandahl</i> <i>et al.</i> [1980]	Isotropic electrons	No information	No information
<i>Saito et al.</i> [1992]	No information	Maxwellian $E_0 = 2.5$ keV	No information

1.3.1 *ULF Pulsations and Precipitation Pulsations*

Wave growth, γ , can be described by a simple product of three terms [*Coroniti and Kennel, 1970*]:

$$\gamma \approx \Omega A \eta.$$

Here, Ω is the gyrofrequency of the electron, A , is the pitch-angle anisotropy, which is a measure of the phase space gradient of the electron distribution and η is the number of electrons that are in resonance with the wave. The number of resonant electrons is related to the amplitude of the wave, with more resonant electrons giving rise to a larger wave amplitude and fewer resonant electrons resulting in a smaller wave amplitude. The anisotropy drives the wave growth, large values of the anisotropy feed growth. When the anisotropy is small waves will be either damped or unable to grow.

Coroniti and Kennel [1970] related the pitch-angle anisotropy to a changing magnetic field. The changing anisotropy, in turn, causes a change in the growth rate of the waves. Once the waves have grown large enough, they resonantly interact with the electrons in the region and cause precipitation. The changing magnetic field referred to by *Coroniti and Kennel [1970]* were Ultra-Low-Frequency (ULF) micropulsations. These are large wavelength, long period magnetic perturbations found throughout the magnetosphere. ULF pulsations have a range of periods and span the typical periods seen in pulsating aurora making them a possible candidate for inducing the electron precipitation.

There have been ground-based observations of magnetic pulsations which are correlated with electron precipitation pulsations [*McPherron et al., 1968*]. However, the magnetic pulsations may be caused by currents set up in the iono-

sphere in response to the precipitation of energetic electrons. *Oguti et al.* [1986] reported that while pulsations were observed on the ground, there were no hydromagnetic waves observed in the magnetosphere. Contrasting these observations, *Chisham et al.* [1990] and *Taylor et al.* [1989] report that optical pulsations were concurrently observed with giant pulsations (Pg) which they interpreted to have been caused by a proton drift instability. Furthermore, *Hillebrand et al.* [1982] also observed oscillations of electron flux in the equatorial plane with a comparable period to concurrently observed giant pulsations.

The Coroniti and Kennel (1970) model depends upon an outside influence, the ULF pulsations, to produce the electron pulsations. A different model proposed by *Davidson* [1979, 1986a, b, 1990] depends upon the changing pitch-angle distribution to cause the pulsations self-consistently. This model has been fairly well developed and is called the relaxation oscillator [*Davidson*, 1986a; *Davidson and Chiu*, 1986]. A variation of this model is called the cyclotron maser model [*Trakhtengerts et al.*, 1986; *Demekhov and Trakhtengerts*, 1994]. These models and their consequences will be explored in the next section.

1.3.2 *Relaxation Oscillator and Cyclotron Maser Models*

The relaxation oscillator model depends upon the changing distribution function or phase space density in the region in which the pulsations are produced. This is similar to the Coroniti/Kennel model but different in how the pitch-angle anisotropy changes. In the Coroniti/Kennel model the change is brought about by a magnetic field perturbation. In the relaxation oscillator model, the change in pitch-angle anisotropy is brought about by the electrons which are backscattered up the field lines out of the ionosphere. Backscattered electrons are electrons which have traveled into the ionosphere and collided with molec-

ular species. After collision, the electrons travel back out of the ionosphere into the equator along the magnetic field.

The cyclotron maser model of [Trakhtengerts *et al.*, 1986; Demekhov and Trakhtengerts, 1994] is similar to the relaxation model except that the electrons which modify the pitch-angle anisotropy ∇B drift into the interaction region. This drift is energy dependent so higher energy electrons will travel around the magnetosphere in shorter times than will lower energy electrons. The effects of such a drift would seem to blur out the velocity dispersion measured by Bryant *et al.* [1975] because different energy electrons would be arriving at the interaction region at different times and this is contrary to the assumptions of Bryant *et al.* [1971, 1975] that the electrons all leave the same area at the same time.

As in the Coroniti/Kennel model, both the relaxation oscillator and the cyclotron maser models depend upon a wave-particle interaction occurring in the equatorial region of the magnetosphere. To start the pulsation, the anisotropy has to grow large enough to start wave growth. This is accomplished by loss of electrons into the ionosphere. The backscattered electrons produced by the precipitated energetic electrons or the drifting electrons enter the equatorial region and fill the loss-cone and reduces the pitch-angle anisotropy. This results in damping of the wave which, in turn, results in fewer electrons being moved into the loss cone. In this way the pulsation is turned off.

In summary, the pitch-angle anisotropy increases initially due to electron loss to the atmosphere and waves are able to grow. These waves resonantly pitch-angle scatter electrons into the loss cone where they precipitate as pulsations. Backscattered or drifting electrons move back into the source region where they lower the pitch-angle anisotropy and the waves damp and precipitation

pulsations cease. The cycle is then repeated again.

The cyclotron maser model put forth by *Trakhtengerts et al.* [1986]; *Demekhov and Trakhtengerts* [1994] is a variation of the the relaxation oscillator model. Here the source of electrons which drive the instability are electrons which ∇B drift into flux tubes in which whistler waves are found. This model can predict the 3 Hz modulations that are often seen concurrently with the longer pulsations.

These theoretical models describe the basic understanding of pulsating aurora. Each depends upon an electron cyclotron wave-particle interaction in the equatorial plane of the magnetosphere and each is able to predict the pulsating aurora. None of the models addresses the recurrent physical shapes observed in pulsating auroral displays. Importantly, given the typical number density of electrons in the equatorial region of the magnetosphere, electron cyclotron waves are unable to resonate with electrons of energies below ~ 20 keV. Thus, neither of these models satisfactorily explains the low energy ($E \sim 5$ keV) electrons that are always seen in the pulsation measurements. Also no observations have ever been made of backscattered electrons modulating the pitch-angle anisotropy.

1.4 Scope of This Dissertation

The current available data set on pulsating aurora as shown in Table 1.1 indicates that not all of the information necessary to understand the phenomena has been collected. Information on the backscattered component of precipitating electrons does not exist and as such no understanding of the relaxation oscillator model is possible. Furthermore, the observed pitch-angle distributions

show different results for different events and are lacking in high temporal and spatial resolution. The observed velocity dispersion of the electrons could also be improved with higher temporal resolution.

For these reasons a sounding rocket experiment was launched from Poker Flat, Alaska on March 13, 1997 in order to make new and more complete observations of pulsating aurora. The scientific objectives of the experiment were aimed at obtaining a more complete set of wave and particle data with respect to pulsations. For the first time backscattered electrons were measured over a pulsating aurora. The high time resolution and pitch-angle coverage, along with the excellent energy range and resolution have enabled better understanding of the electron distribution which in turn allows better explanations about the physical causes of the pulsations to be advanced.

The research presented in this dissertation raises many new questions about the current understanding of pulsating aurora. Our observations show no discernible velocity dispersion, nor do we see a 3 Hz modulation of the electron precipitation. For the first time pulsations were observed in energies as low as 1 keV and pulsation signatures (not the same as pulsations) were seen down to 10's of eV. Careful analysis has shown that these low energy electrons are actually backscattered. These low energy observations have led to the inference of a parallel potential drop located above the rocket. This is the first time such a potential has been associated with pulsating auroras. The pitch-angle distributions of the high energy ($E > 5$ keV) electrons indicate that there is some kind of dynamic process occurring below the rocket. Furthermore, the pitch-angle distributions show no sign of becoming isotropic during a pulsation event. Finally we measured the electron characteristic energy for energies between 5 and 25 keV and show that it becomes larger during a pulsation event. With the new observations we are forced to discount both of the models discussed in

Section 1.3 for this event. Guidelines for what a new model must incorporate will be laid out and discussed.

Chapter two discusses the fabrication and calibration of the particle measurements. Chapter three discusses the analysis of the data obtained during the flight and Chapter four discusses why previous models are inadequate in describing our observations and presents results that any new model would have to address in order to explain our observations. Chapter five discusses some implications of the work and what we have to look for in future sounding rocket experiments.

Chapter 2

ROCKET INSTRUMENTATION

The rocket payload was equipped with six solid state telescopes and an electrostatic analyzer. These instruments were used to detect electrons over an energy range of 12 eV to 25 keV for pitch-angles from 0 to 180° (ESA) and electrons over an energy range of 25 to 500 keV for pitch-angles from 0 to 90° (SST's) and protons over an energy range of 90 keV to 600 keV. The payload also had electric and magnetic field antennas designed to operate in the very low frequency (VLF) range as well as instruments designed to detect the dc electric and magnetic fields. The field data are not discussed in this thesis. The purpose of such a broad array of instruments was to measure as completely as possible the physical environment in the region of space over a pulsating aurora.

2.1 Instrument Counts and Particle Flux

The output of both the solid state telescopes and the electrostatic analyzer are given in numbers of counts. We convert these counts into physically meaningful quantities by dividing the counts by the constraints of the instrument. This will enable our measurements to be compared to the measurements of other instruments. The conversion of counts into flux uses the geometric factor, the sample time and the energy range over which the sample was collected. In this way we have counts per sample time, per energy range, per detector surface

area and per solid angle through which the detector accepts particles.

The geometric factor depends only on physical parameters and for the electrostatic analyzer's curved geometry these quantities must be measured carefully. The geometric factor for the solid state telescopes is easier to both visualize and measure. Details of the solid state telescope geometric factor and theoretical derivation and calculation of the geometric factor for the solid state telescopes are included in Appendix A.

A detailed derivation of how particle counts are converted into flux and the distribution function is contained in Appendix B. However, a simple discussion of how the instrument counts are related to actual electron phase space densities is included here to facilitate discussion. The number of measured particles is related to the actual number of particles given by

$$\delta C = \Gamma \delta N,$$

where δC is the number of counts recorded by a particle detecting instrument, δN is the total number of particles in some region of phase space, and Γ is an instrument specific constant of proportionality. The quantity Γ consists of parts that are purely geometric and also a part that is related to the efficiency of how the detector reports counting events.

One way to determine a detector's counting efficiency is to determine how many particles are directed onto the detector's collecting area and to compare this number to the number that are actually recorded. The ratio of these two quantities is the efficiency. There are difficulties encountered when one tries to quantify how many particles are directed onto the detector surface area. Usually what is done is to figure out how many particles are hitting the detector by either using a detector with a known response or using a source with a

known output. These are then compared to theoretical models for the instrument throughput. In our case we used a combination of both of these procedures.

The efficiency calculation includes the angle of incidence of the particle hitting the detector. A particle that just grazes the detector surface area may not be recorded while the same particle on a more normal trajectory would be recorded as an event. Another factor that affects the efficiency is when large numbers of particles hit the detector. All instruments suffer from a period of “dead time” when the instrument is busy dealing with a previous count and cannot measure a count that comes in just afterward. If there is a large flux of particles, the ability of the detector to count is reduced and our estimate of the actual counts is in error. This means that the dead time correction is more important when the flux is large. For our event this was not a factor because the fluxes were over an order of magnitude smaller than expected. Another factor that may affect efficiency is the temperature at which the instrument operates. Electronics are designed to operate at some range of temperatures. The environment of a rocket can place the electronics under some extreme temperature changes and the instrument’s counting response must be understood.

Aside from the efficiency the factor, Γ also includes a geometrical effect. The geometric factor is intimately related to the design of the instrument and is used to restrict the number of counts to an amount that the instrument electronics can handle. This is something of a paradox since we build an instrument with a predetermined ability to measure particles but we do not know beforehand how many particles we will need to measure. The determination of the geometric factor is a very important part of the actual instrument calibration. The next few sections will contain a discussion of some of the pertinent factors in the calibration and construction of the particle detection instruments.

2.2 Solid State Telescopes

The solid state telescopes were designed to detect energetic particles over a range of 30–500 keV. The rocket carried 6 solid state telescopes. Five of them were dedicated to the detection of electrons and the last was used to detect protons. The proton detector was pointed upward along the magnetic field with the idea that precipitating protons along the magnetic field would show the greatest variation between background and signal, and so would show the clearest evidence of pulsations.

The proton detector was exactly the same as the electron detectors except that it was designed to exclude electrons by deflecting them with a strong magnetic field placed at the collimator. The Lorentz force supplied by the magnetic field turned the electrons away from the detector surface. The protons with their larger mass and respectively smaller Lorentz force passed through the magnetic field with very little trajectory change. Since the flux of protons was thought to be less than the flux of electrons, the geometric factor of the proton detector was approximately 5 times larger than the geometric factors of the electron detectors.

The static magnetic field supplied by the magnets was chosen to deflect electrons with energies up to approximately 400 keV. We assumed that the flux of 400 keV electrons would be small compared with the flux of lower energy protons and the electronics of the solid state telescopes were set so that any particle with an energy over approximately 400 keV would be rejected (see Appendix C).

Solid state detectors are basically silicon wafers [Knoll, 1989] that are held at a voltage bias. When an energetic particle enters the silicon wafer, the particle

loses energy and produces secondary electrons. These electrons are driven into the conduction band of the silicon. The applied voltage drives the freely drifting electrons onto the cathode where they appear as a current. In this way a measurement of energy is made since more energetic particles will produce more secondary electrons in the conduction band and generate a larger current. As a matter of convenience the current is changed into a voltage pulse which is then converted into counts.

The detectors were covered with an aluminum layer to shield the solar UV. Protons, with their larger collisional cross section, are not as efficient in getting through the aluminum layer as electrons. This resulted in proton detector being insensitive to any protons less than approximately 90 keV. The range of protons detected was 90 – 600 keV.

From all other observations of pulsating aurora we determined that, on average, typical fluxes of precipitating electrons in these energy ranges were no more than 1×10^4 Counts/(sec cm² sr keV). Using this rough estimate and the instrument geometric factor (see Appendix A for a theoretical derivation of the geometric factor for the solid state telescopes), one can determine the number of counts that the electronics should be able to handle. In our case, the electronics were designed to handle approximately 100,000 counts per second and a geometric factor of approximately 0.02 cm² sr was chosen to accommodate the maximum flux rate of approximately 1.25×10^4 (counts/s cm² sr keV).

The sample rate of the solid state telescopes is dictated by the dead time of each separate detector. For our detectors, this dead time was on the order of 600 nanoseconds. The instruments were set up to accumulate counts from each detector over increments of 10 milliseconds. This final sample rate was chosen as a balance between a limited telemetry rate and the need to be able

to distinguish possible variations in the 1 – 10 Hz range. With a sample rate of 100 samples per second we were able to detect variations of 50 Hz or less.

The solid state telescopes were arranged to observe particles with pitch angles of 0° , 22.5° , 45° , 67.5° and 90° with respect to the rocket spin axis. The field-of-view (FOV) for the solid state telescopes were approximately ± 11 degrees. The five solid state telescopes completely covered the range of pitch angles from 0° to 90° .

The electrons detected over the energy range of 30 – 500 keV, were binned into 32 separate energy bins. The width of these bins was variable, with higher energies having larger bin widths. The actual energy boundaries can be found in Appendix C.

2.2.1 Solid State Telescope Components

The components that go into the solid state telescope instrument are shown in Figure 2.1 as a block diagram. The detectors were biased with a 100 volt power supply. The output of each detector was fed to a preamp circuit which converted the charges into a voltage and then amplified the signal. The signal was then changed into the digital counts that were telemetered back to the ground.

The preamp was followed by the peak hold and detect circuit. This circuit supplied amplification and shaped the signal into one that could be digitized. Each pulse, which signified a single count, was shaped into a square pulse of a length of ~ 1200 nanoseconds.

The peak hold board included integral counters that counted all the pulses that came from the detector. The integral counters made no distinction between

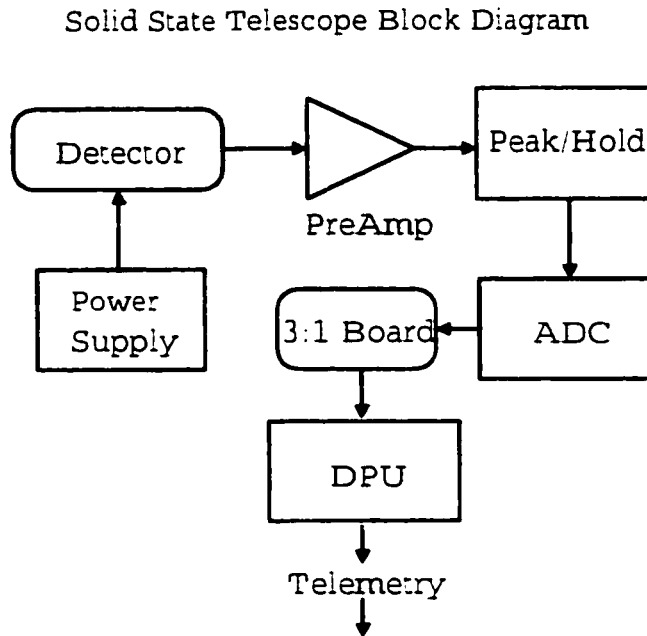


Figure 2.1: Block diagram of the solid state telescope electronic components

pulses of different energies. Their only job was to count everything that was detected. In this way, we had a check of how the electronics were working. If the counts reported by the integral counter equaled the sum of all the counts reported by the differential energy channels, we know that the electronics past the peak hold board were working correctly.

Once the pulses from the detector had been shaped, the signal went to the analog to digital converter (ADC). This circuit changed the analog voltage signal into a digital value and sent the results to the digital processing unit (DPU) board. The DPU binned the digital voltages into 29 separate channels. Thus, the original current set up by the collision of an electron with the detector has

now been changed into a count in a table of different voltages.

The solid state telescopes were calibrated in several ways. Of all of the variables that could be checked, the most important were: a) How each detector recorded the energy of an electron of known energy and b) How accurately each detector counted the number of electrons that impinged onto its surface. In order to understand how each instrument responded to electrons of known energies and flux, all the different parts in each of the circuits discussed above were carefully checked to see that operations went as expected. By building up information about how each instrument recorded the various energies and how each instrument counted the incoming electrons a complete calibration was established. The specific calibration information concerning the energy bin widths and dead time calibration can be found in Appendix C.

2.3 *Electrostatic Analyzer*

The electrostatic analyzer was designed to detect energetic electrons over an energy range of 12 eV to 25 keV, and uses a dc electric field applied over a curved surface to reject all particles other than those of a certain narrow energy width. The dc field is varied so that various energies are detected at different times. This is intrinsically different from the solid state telescopes which detect all energies at the same time.

The logarithmically spaced energy ranges of the detector were swept from high to low energies in 32 steps with a dwelling time of 1.5625 milliseconds. A full energy sweep is achieved every 50 milliseconds. With 20 complete samples per second, precipitation variations of up to 10 Hz were detectable.

The electrostatic analyzer field of view spanned 180°, enabling sampling of both

up-going and down-going electrons. The 180° field of view was split into 16 different sectors, each of which covered approximately 11.25 degrees. The sectors consisted of separate anodes which detected electrons coming from a particular direction.

The electrostatic analyzer works on a simple principle [Carlson and McFadden, 1998]. The applied electric field in a spherically shaped parallel plate geometry causes electrons to move in circular trajectories from the entrance aperture to the microchannel plates where they are detected. The force of the electric field is balanced by the centripetal acceleration the electrons undergo in moving along the trajectory. We can write this as:

$$\frac{mv^2}{r} = \frac{qk}{r^2}$$

where v is the particle velocity, q is the charge of the electron, m is the electron mass, k is a constant and r is the radius of the particle from the center of the instrument. This relation indicates

$$\text{Energy} \sim \frac{f(V)}{r}$$

The energy, E of the particle goes as a function of voltage $f(V)$ divided by radius. A small change in energy can be written as

$$\frac{\Delta E}{E} \sim \frac{\frac{f(V)}{r^2} \Delta r}{\frac{f(V)}{r}} \sim \frac{\Delta r}{r}$$

Δr is the distance between the concentric hemispheres and ΔE is the energy range which is detected by the instrument when it is set at a particular voltage.

After moving through the hemispheres the electrons collide with a set of microchannel plates. Microchannel plates are essentially stacks of electron mul-

tipling tubes. An electron enters one end of the tube and collides with the walls of the tube and new electrons are kicked off and travel down the tube. After many collisions, the single electron exits at the other end magnified approximately by a thousand fold.

This cloud of approximately one thousand electrons is then directed onto a second microchannel plate and the same process occurs again. At the other end of the second microchannel plate, approximately 1 million electrons stream out. This 10^6 -fold amplification allows for the detection of single input energetic electrons.

The cloud of electrons leaving the microchannel plates is collected by an anode which is connected to a preamplifier. The preamplifier boosts the signal and sends it to a digital device which converts it into a signal that is sent to the digital processing unit.

2.3.1 Calibration and Testing of the Electrostatic Analyzer

The calibration of the electrostatic analyzer was done before the flight. After the flight, we looked at the data and made further changes to the geometric factor for the electrostatic analyzer. Before the flight the instrument recorded energy spectra from a Ni-63 source of electrons. This source is a beta emitter with an end point energy of approximately 66.8 keV. This is an ideal source for testing the electrostatic analyzer since the emission range spans the energy range of the instrument. Aside from the Ni-63 spectra, the instrument was also calibrated by use of an electron gun. The electron gun produced electrons of a specific energy which are then directed into the electrostatic analyzer.

Both of these sources, the Ni-63 and the electron gun, have physical charac-

teristics which complicated the calibration. Since the careful calibration of the instrument requires complete understanding of the electron source a brief discussion of the sources will be included.

The Ni-63 source, a beta emitter, emits a continuous spectrum of electrons. The physics of β - decay are understood [*Frauenfelder, 1974*] well enough to be able to predict the energy spectra. Thus, one can compare a measured spectrum to a theoretically predicted one.

The electron gun produces electrons in the following manner. A source of ultraviolet (UV) photons is directed to the surface of a material which emits electrons through the photo-electric effect. The electrons which are produced are then accelerated to the desired energy by an electric field. This produces monoenergetic electrons in a fairly narrow beam and one can direct the beam onto the particle detecting surface of the electrostatic analyzer.

The difficulties in producing a steady monoenergetic beam of electrons are many. Perhaps the most difficult task is accurately assessing the output of the electron gun. Both the electron gun and the electrostatic analyzer itself were in need of independent calibration. The electrostatic analyzer can also detect the photons from the UV source. So care was taken to keep down the number of reflections by the use of non - reflective coatings in the testing chamber.

Another calibration anomaly which was accounted for was the background magnetic field of the earth. Magnetic fields are able to steer electrons toward or away from the instrument thereby skewing the measured counts. A Helmholtz coil was used to null out the background field but it could not get rid of the field from a stepper motor which was used to direct the pointing of the instrument in the chamber.

Angular Calibration

Figure 2.2 shows a single run of the electrostatic analyzer and the electron gun. The plot shows counts as a function of scan angle. The analyzer was moved through 2 degree angle steps and the counts were recorded for 400 milliseconds at every step. The gap in the data at $\sim 38^\circ$ is due to an anode that was burned out during previous testing. The scan corresponding to the 129 degree detector demonstrates a slippage of the stepper motor, resulting in a profile that is noticeably wider than those of all the others.

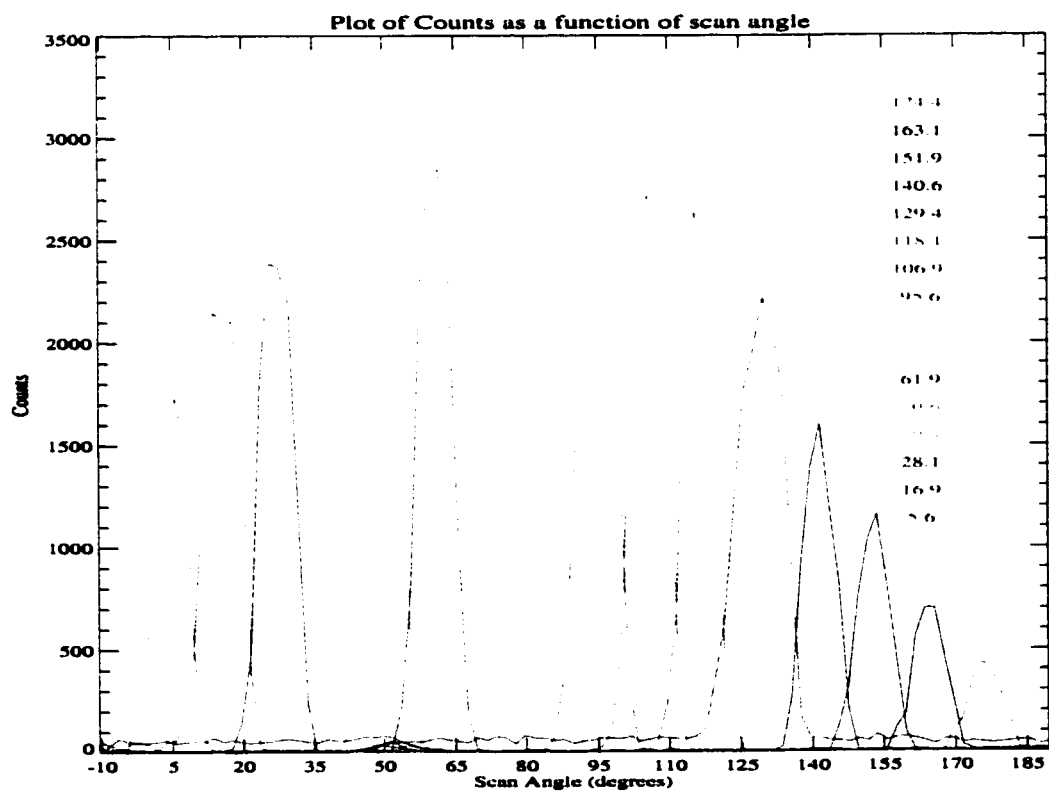


Figure 2.2: Azimuthal scan of the electrostatic analyzer. The energy of the incident electrons was approximately 1000 eV.

Further scrutiny of the figure shows that there is a distinct asymmetry about

the center of the scan. Since the electrostatic analyzer is symmetric about its axis, one expects the instrument response to be symmetric. However, the counts at the 173 degree anode are a factor of approximately 4 times less than the counts at the corresponding 5 degree anode. We have ascribed this asymmetry to the likelihood that the two hemispheres were imperfectly aligned, that is, they were not concentric. When this happens the field between the hemisphere is not constant which causes some variations in the number of electrons which get to the detector surfaces.

A further complication arose from the slit opening on the instrument. This opening was not the same size for all anodes. As the anodes moved further from 90°, the size of the entrance aperture became smaller. The response of the anodes as a function of scan angle was modeled as $\frac{1}{2}(1.0 + \sin(\alpha))$ where α is the pitch angle of each detector with respect to the rocket. Thus, the 5° detector should have a response that is one half of the response of the 90° detector and as is seen in Figure 2.2 this is approximately correct.

As can be seen from Figure 2.2, the response did not vary smoothly. The anodes at 73 and 84 degrees recorded less counts than expected. This dip in counts around these two detectors had to be accounted for in the geometric factor determination. The dip in the 84° detector was about 10 percent of the expected value and the dip in the 73° detector was about 6 percent of the expected value. Table 2.1 shows the geometric factors of the electrostatic analyzer in which all of the different factors coming from the calibration are taken into account. Appendix B shows sample calculations of how to turn counts into flux as well as methods for determining the moments of the distribution function.

Table 2.1: ESA geometric factor as a function of angle with respect to the rocket spin axis. The electronics at anode at 39° was burned out during calibration.

Angle (degrees)	Geometric factor $\text{cm}^2 \text{ sr}$
5.625	4.56×10^{-4}
16.875	5.35×10^{-4}
28.125	6.11×10^{-4}
39.375	-
50.625	7.36×10^{-4}
61.875	7.81×10^{-4}
73.125	8.12×10^{-4}
84.375	7.04×10^{-4}
95.625	8.28×10^{-4}
106.875	8.93×10^{-4}
118.125	7.03×10^{-4}
129.375	7.36×10^{-4}
140.625	6.78×10^{-4}
151.875	6.11×10^{-4}
163.125	8.29×10^{-4}
174.375	12.2×10^{-4}

Chapter 3

ELECTRON DATA ANALYSIS

3.1 Rocket Flight and Data Summary

On March 13, 1997 at 10:20:31 UT a rocket was launched from Poker Flat Research Range (Magnetic Latitude $59^{\circ} 05' 24.0''$, Magnetic Longitude $214^{\circ} 48' 36.0''$) into a pulsating auroral event. The physical environment at the time the rocket was launched was extremely complicated. There were fast auroral waves moving across the sky just prior to launch. At launch time pulsating patches covered much of the sky to the north of Poker Flat as indicated by the all-sky camera (not shown). Also the pulsations observed that night exhibited a streaming nature, that is, the illumination in a particular patch started from a point in the patch and then rapidly extended to incorporate the entire patch. Figure 3.1 shows a plot of the H, D, and Z components of the magnetic field of the Earth from both Poker Flat Research Range and Fort Yukon (Magnetic Latitude $60^{\circ} 22' 12.0''$, Magnetic Longitude $212^{\circ} 33'$). A 100 nT bay started around 0940 UT and the rocket was launched into the recovery phase of this small substorm. The beginning and end of the flight are marked by the vertical bars.

Figure 3.2 shows a sequence of global auroral images from the Ultraviolet Imager (UVI) aboard the POLAR spacecraft with the position of the rocket given by the red circles. The images were taken in the Lyman-Birge-Hopfield bands ($\sim 160 - 180$ nm) and are displayed in both geographic and geomagnetic coordi-

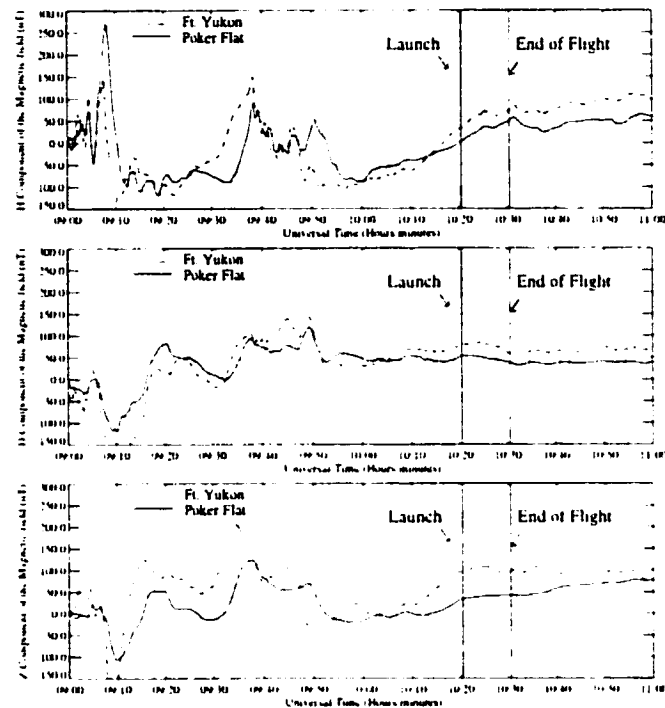


Figure 3.1: The H, D, and Z magnetic field components as measured by the stations at Poker Flat and Fort Yukon. The traces show that the flight took place during the recovery phase of a magnetic disturbance.

nate systems. The global auroral activity was subsiding and only dim discrete auroral structures were evident during the time the pulsations were observed. Pulsations are known to occur more frequently during the recovery phase and the subsiding global activity is consistent with these previous observations.

Figure 3.3 shows a summary plot of the electron data for energies between 0.01 and 26 keV. The topmost panel shows the precipitating differential energy flux displayed in the spectrogram format. This plot shows precipitation was centered on average around 10 keV. The pulsations are identified by increases of energy fluxes that extend beyond the 26 keV energy channel. About nine

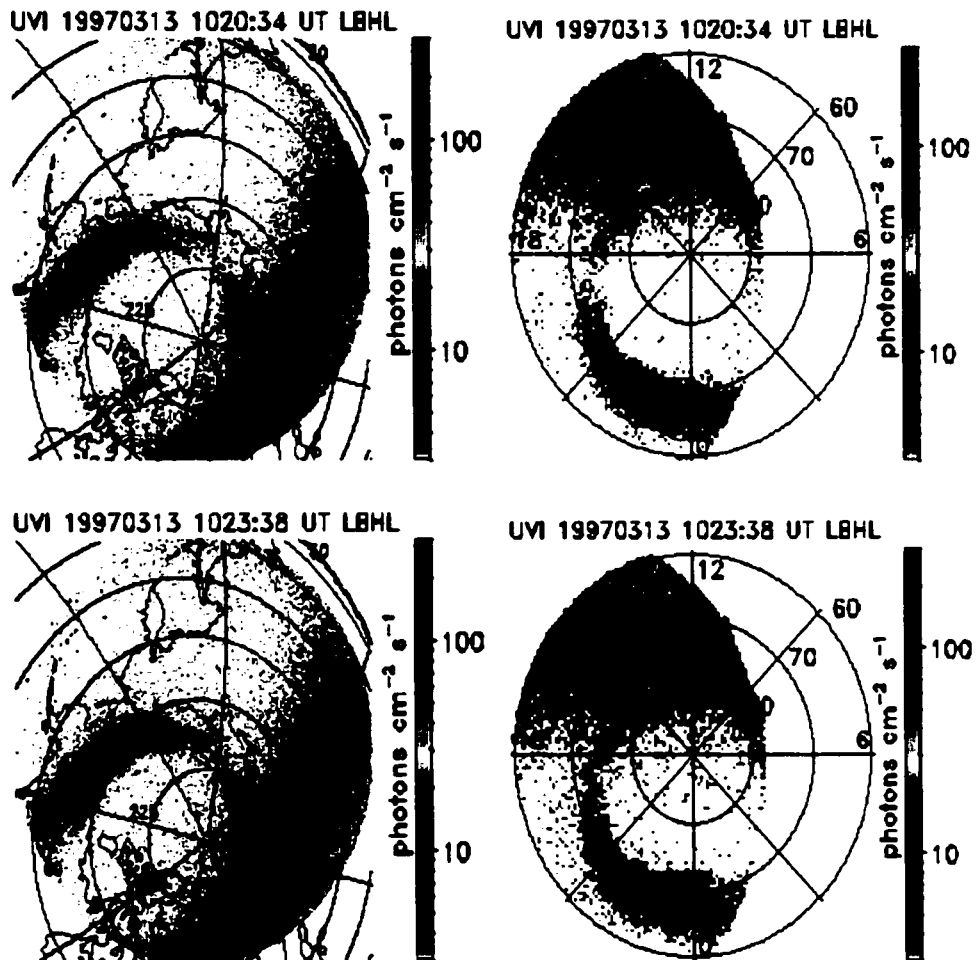


Figure 3.2: UltraViolet Imager(UVI) images taken just prior to and during the rocket launch on March 13, 1997. A weak auroral arc is observed over much of northern Alaska. The approximate position of the rocket is given by the red circle.

pulsations can be seen and the times when they occurred are identified by the solid triangles at the bottom of the plot. The second panel shows the pitch-angle spectrogram spanning from 0° to 180° . The peak energy flux occurred between 45° and 90° and the energy falls off as one goes to smaller and larger pitch-angles. During the pulsations, the energy flux enhancement is observed over a broader pitch-angle range, from less than 35° to greater than 170° . The bottom panel shows the energy flux integrated over all energies of upgoing ($90 - 180^\circ$) and downgoing ($0 - 90^\circ$) electrons. The downward fluxes exceed the upward fluxes by roughly a factor of 1.5, including the time when the pulsations were observed.

Electrostatic analysers are energy per charge detectors and one can obtain information on the distribution function of the pulsations. To illustrate the phase space features Figure 3.4 shows an example of the distribution function for the pulsations that occurred at 146 s (top panel) and the unstructured electron fluxes from 135 s. Phase space densities are displayed as isocontours in velocity space. The perpendicular (with respect to the magnetic field) velocity (in km/s) is plotted on the vertical axis and the parallel velocity on the horizontal axis. The dotted lines are used as a reference for an isotropic distribution.

The distribution function of both pulsation and background for $v_{\parallel} < 2 \times 10^4$ km/s ($E < 1$ keV) is nearly isotropic. However, for v_{\parallel} larger than this, the phase space contours are asymmetric and skewed. Instead the axis is shifted approximately 20 degrees from the normal. We have considered the possibility that this could be caused by the misalignment of the detector with respect to the magnetic field. However, analysis of the pitch-angle distributions shows no discontinuities in the flux as would be expected if the detector was misaligned. We are confident that the observed skewed distribution is real and is representative of the source.

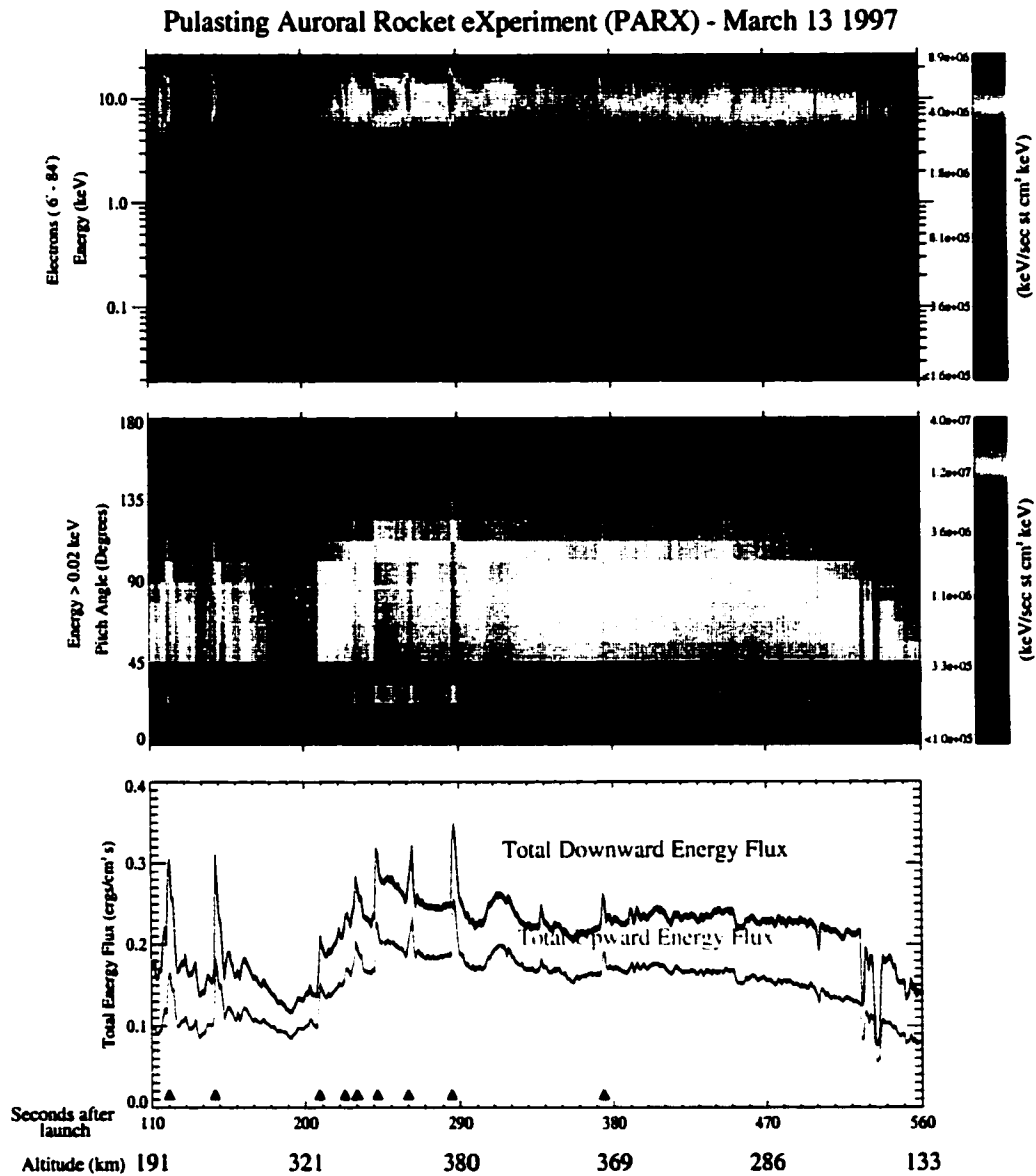


Figure 3.3: Energy flux and pitch angle spectrogram as a function of time. The top panel shows the differential energy flux spectrogram for the precipitating electrons. The middle panel shows the pitch angle spectrogram of the differential energy flux. The bottom panel shows the total upward and downward energy flux.

Important features shown here include the large gradients in the phase space for the electrons traveling into the ionosphere ($0 - 90^\circ$ pitch-angles), the isocontours near the field aligned direction (bottom right hand side of the plots) show a loss cone feature. The lower left hand side of the plots show that a considerable amount of electrons are traveling away from the ionosphere ($-v_{\parallel}$ direction). Note that there is an indication that the upgoing electrons have larger velocities (energies) than the downgoing electrons. These interesting features will now be examined in detail so that the source(s) of these electrons can be characterized.

3.2 Differential Energy Spectra and Pitch-angle Distributions

3.2.1 General Features

An effort was first made to ascertain whether or not the changes in flux we observed were of a temporal or spatial nature. Since the rocket was making a single point measurement, it is not possible to tell unambiguously if the changes were spatial or temporal. However, by looking at both the electron flux data as well as the all-sky camera images from that night, we confidently conclude that the changes in flux are due to temporal changes. A full description of how this was done is given in Appendix D.

The differential energy spectra and pitch-angle distributions of the observed electrons provide important information on the sources of these electrons and what mechanisms are responsible for the pulsations. Figure 3.5 is a stack plot of one second averages of the electron particle fluxes for times 115 seconds after the launch, when the instrument was turned on, until the end of the flight. Counts are shown from selected energies of the ESA and SST for electrons

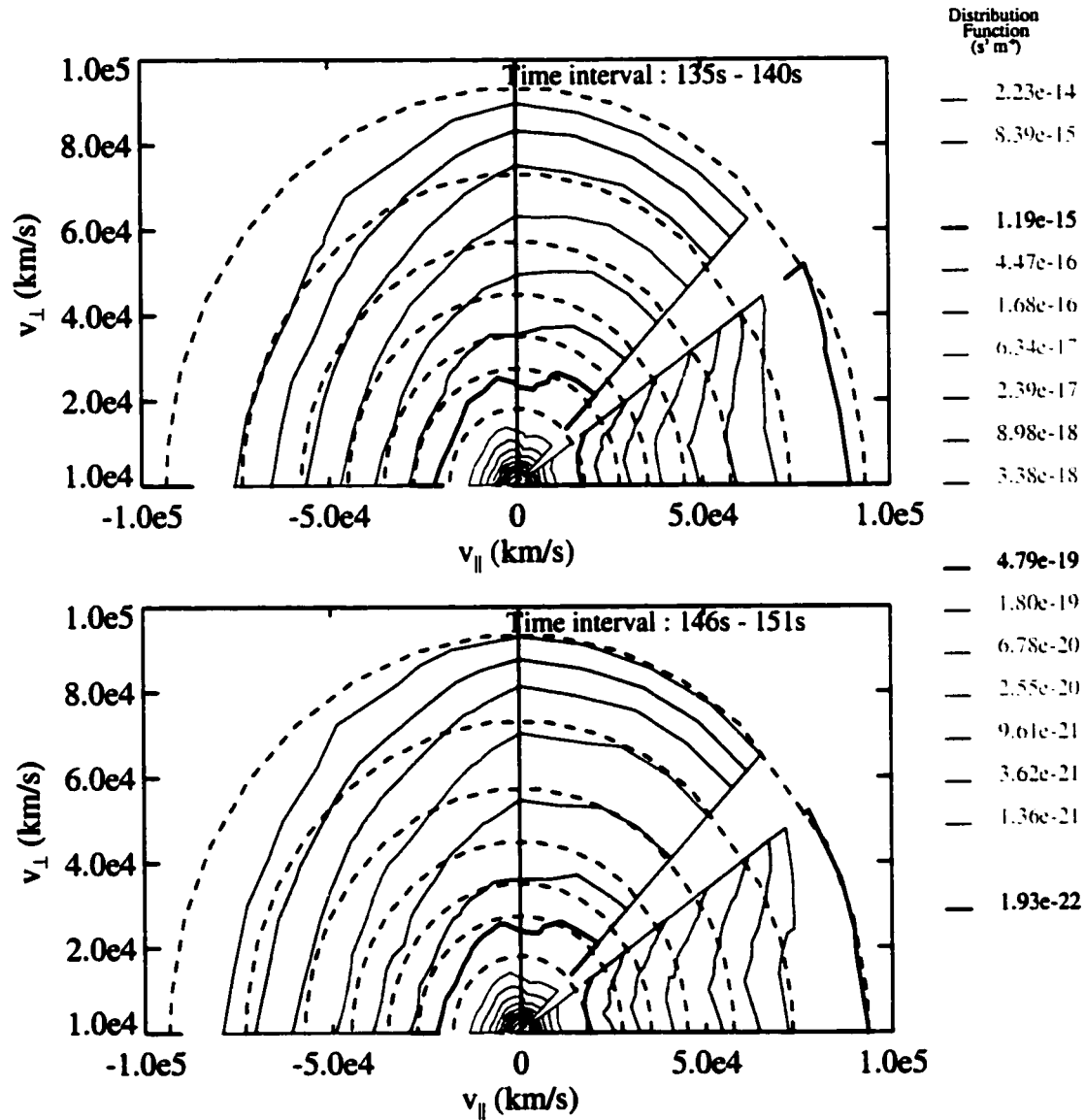


Figure 3.4: Plot of the electron distribution function for the pulsation at 146 s and the background at 135 s. The little wedge with no contours near 45° is due to the burned out anode.

with pitch-angles of $62^\circ \pm 6^\circ$.

Nine pulsations are evident on this plot by the sudden ($t < 0.5$ s) rapid rise and decay in particle flux. The highest energy channel that detected the pulsations was the 54 – 61 keV channel. The pulsations are absent in the energy range of 1 – 5 keV. (From now on these will be called the plateau or the intermediate energy range.) Three of the pulsations extend down to the lowest energy channel ($E = 20 - 30$ eV) and they are marked by solid arrows at the top of the figure. These low energy pulsations have never been seen previously and we will focus on their properties in more detail in Section 3.3 below.

To characterize these pulsations, we show in Figure 3.6 an example of the energy spectrum for the pulsation at 146 seconds after launch and a spectrum for the unstructured background precipitation during the time interval of 135 – 140 seconds. The uncertainty in the energy corresponds to the energy channel width and the uncertainty in the flux to the 1σ Poisson statistical uncertainty. The spectra are from two different pitch-angle directions, one at 6° and the other at 67.5° . The two different look directions show markedly different spectra. For example, while the spectral form for $E < 1$ keV is nearly the same, the behavior in the range 1 – 20 keV shows a strong pitch-angle dependence. There is a plateau for the 67° pitch-angles that is not seen at small pitch-angles.

The form of the energy spectra in the range 20 eV to 60 keV for both the unstructured background flux and pulsations is complicated and can not be fit to a single function. This suggests that several sources are contributing to the electron measurements. The analysis below will separately focus on the three different energy regimes: the low energy regime 0.01 keV to ~ 1 keV, the intermediate energies where no pulsations were observed ($1 \text{ keV} \leq E \leq 5 \text{ keV}$), and finally the high energy regime with energies $E > 5$ keV.

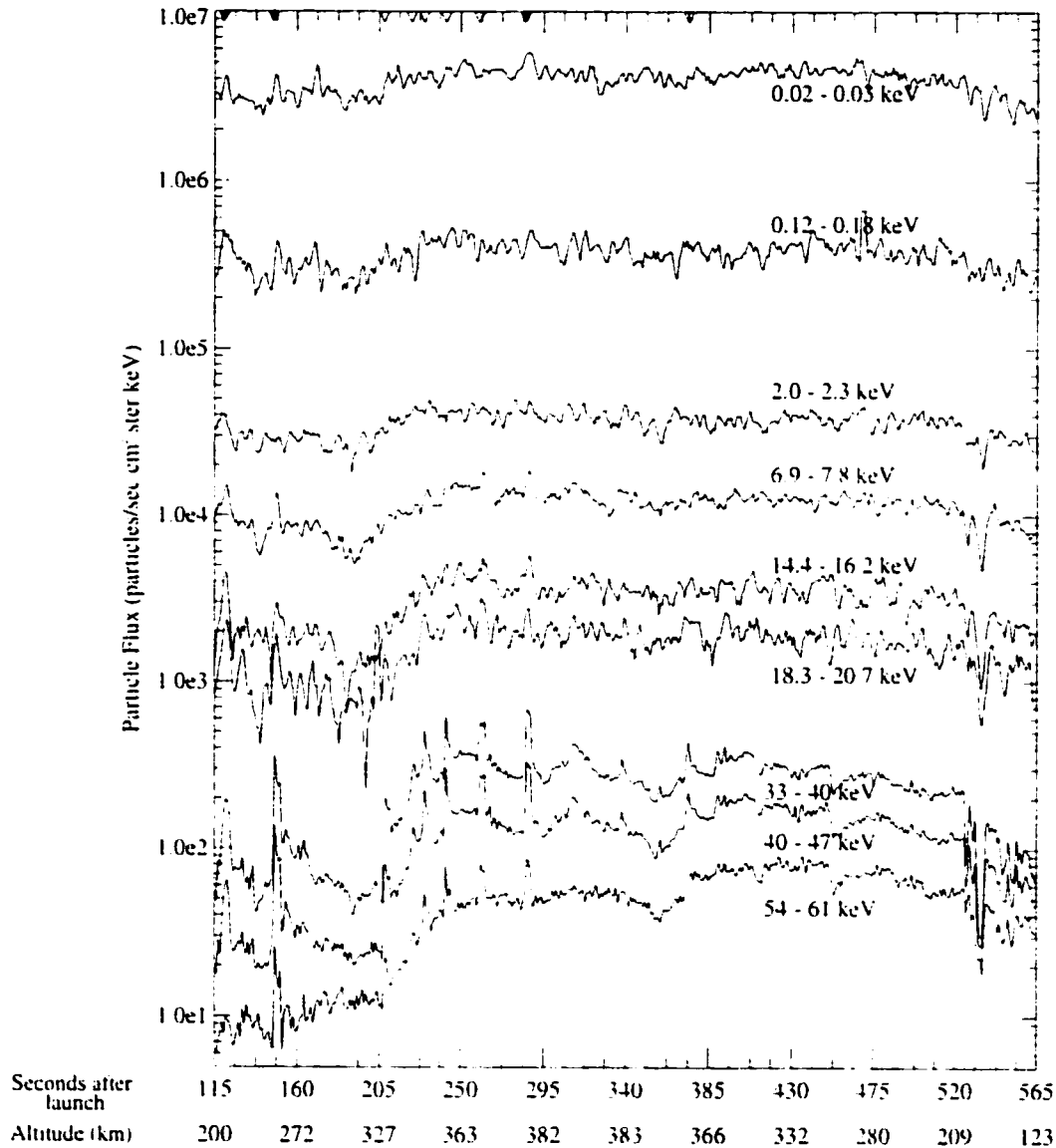


Figure 3.5: Summary plot of electron flux from the electrostatic analyzer and solid state telescope for the $62^\circ \pm 6^\circ$ electrons for selected energies. Nine pulsations are evident as large abrupt changes in the flux and are indicated by the arrows. Three of the pulsations, marked by the solid arrows, show pulsation signatures down to 20 eV. Indicated on the abscissa is the time in seconds after launch as well as the altitude in kilometers.

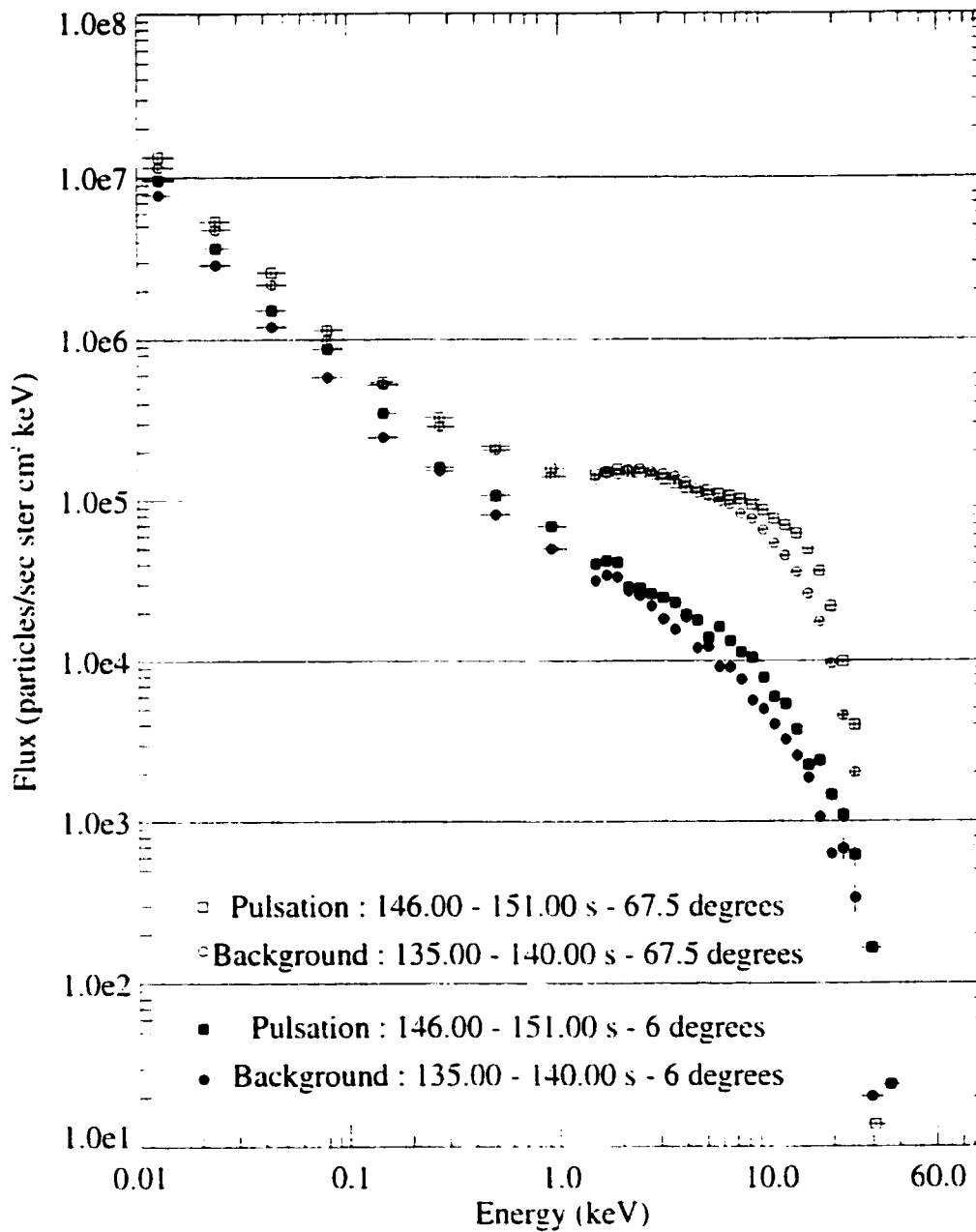


Figure 3.6: Energy spectra for the pulsation at 146 s after launch and the unstructured background at 135 s after launch for electrons at 6° and 67.5° directions. All spectra have multiple components and each differs from the other, indicating a change in the distribution function between the two time intervals and directions.

3.3 Low Energy Electrons ($20 \text{ eV} < E < 1 \text{ keV}$)

Before we performed the analysis of the low energy electrons, we first determined if the counts in the low energy electron channels were in fact electrons and not false counts produced by X-rays due to bremsstrahlung from energetic electrons. We have used the bremsstrahlung theory and using the rocket as a target showed that the counts in the low energy channels are most likely due to electrons and not X-rays. Appendix E gives details about how we are able to come to this conclusion.

Furthermore, a transport model was run using as input our data in order to determine whether or not the electrons we observed in the low energies could have been produced via collisions in the region local to the rocket. The results showed that such collisions were unlikely to have produced the observed fluxes and so we are assuming that the electrons which we observed were not produced at or above the rocket. Details on this analysis and modeling can be found in Appendix F.

Figure 3.7 shows electron flux versus time plots of a pulsation detected at 146 s for selected energies at different pitch-angles. The top four panels correspond to electrons going toward the ionosphere and the bottom four are for electrons going away from the ionosphere. Each data point represents two-second averages and the error bars are computed from Poisson statistics. (Two-second averages are a compromise between higher time resolution with its associated greater uncertainty and lower time resolution with its associated lesser uncertainty.) In each panel, the top four curves represent the low energy pulsations below 1 keV and the bottom curve corresponds to electrons with energies of 5.5 keV.

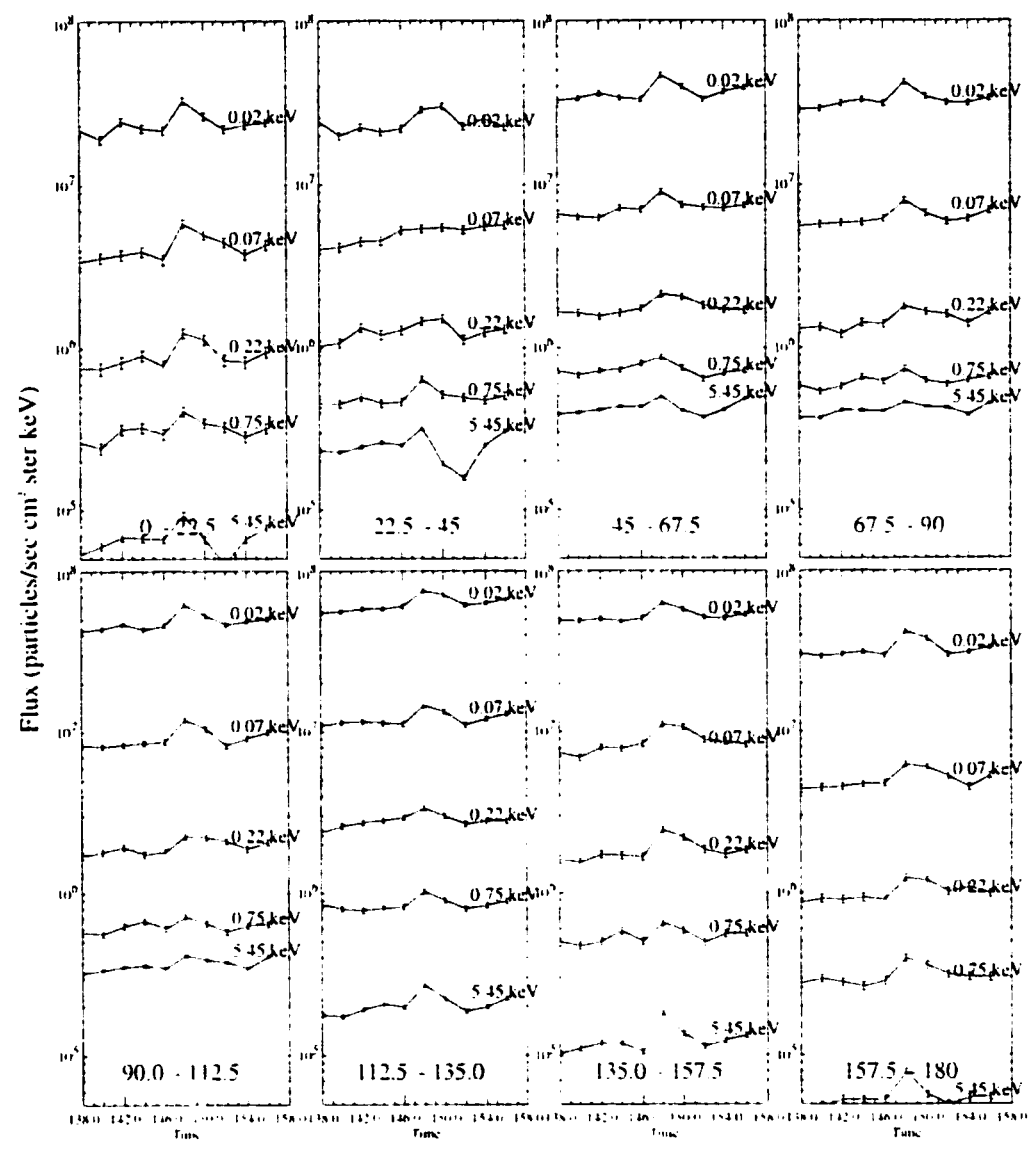


Figure 3.7: Particle flux as a function of time and pitch-angle for selected low energies. The points are 2 second averages and the error bars are computed from Poisson statistics.

The low energy pulsations are present in all the pitch-angle directions including the upgoing pitch-angles. We will show below that these upgoing fluxes indicate that the electrons at these energies and directions have had the downgoing higher energy pulsations imprinted onto them, that these upgoing low energy electrons are showing the response of the ionosphere to a flux of structured high energy electron precipitation. In other words, they are secondaries produced in the ionosphere via collisions of higher energy electrons. At larger pitch-angles, the pulsation feature diminishes at the intermediate plateau region ($E \sim 5.45$ keV) and this feature is more clearly seen for the downgoing than upgoing direction. The pulsation at 119 seconds after launch exhibits the same behavior in that all energies show pulsation signature in the downgoing direction. Likewise the pulsation at 285 seconds shows very similar behavior but is not as clear (not shown).

Figure 3.8 shows a plot of expanded energy spectra of electrons in the downgoing (6° pitch-angle) and upgoing (174° pitch-angle) directions for energies between ~ 10 eV and 3 keV. Each panel includes two curves, from 146 – 151 seconds when a pulsation was detected and from 135 – 140 seconds that cover the unstructured background just prior to the pulsation event. Except for small differences in the fluxes, the spectra are nearly identical for pulsation and background in both downgoing and upgoing directions. The four spectra all fit a power law spectral form, E^γ , with $\gamma \sim -1.3$.

The pitch-angle distributions of this pulsation and the same background time interval are shown in Figure 3.9 for four energies. The electrons are nearly isotropic but the fluxes of $90 - 180^\circ$ pitch-angles are slightly higher (up to a factor of 2) than the fluxes of $0 - 90^\circ$ pitch-angles. The distributions tend to become more anisotropic as the energy increases. Note also the fluxes for the pulsation are slightly higher ($\sim 20\%$) than those of the background.

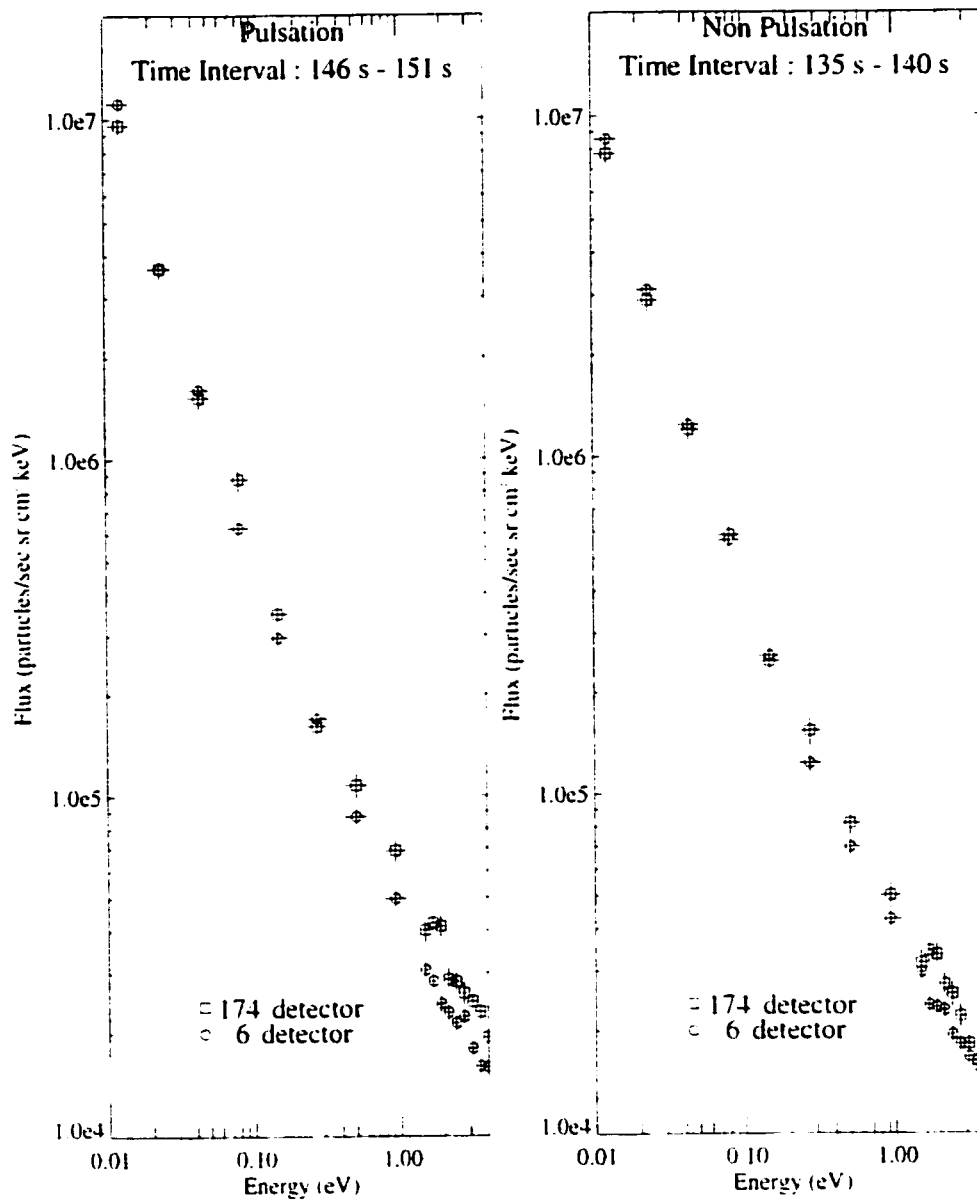


Figure 3.8: Low energy ($E < 3$ keV) spectra of the time intervals of 146 seconds (pulsation) and 135 seconds (background). The electrons are from 6° and 174° pitch angles. Power law fits show that the up and down going spectra are identical for both pulsation and background time intervals.

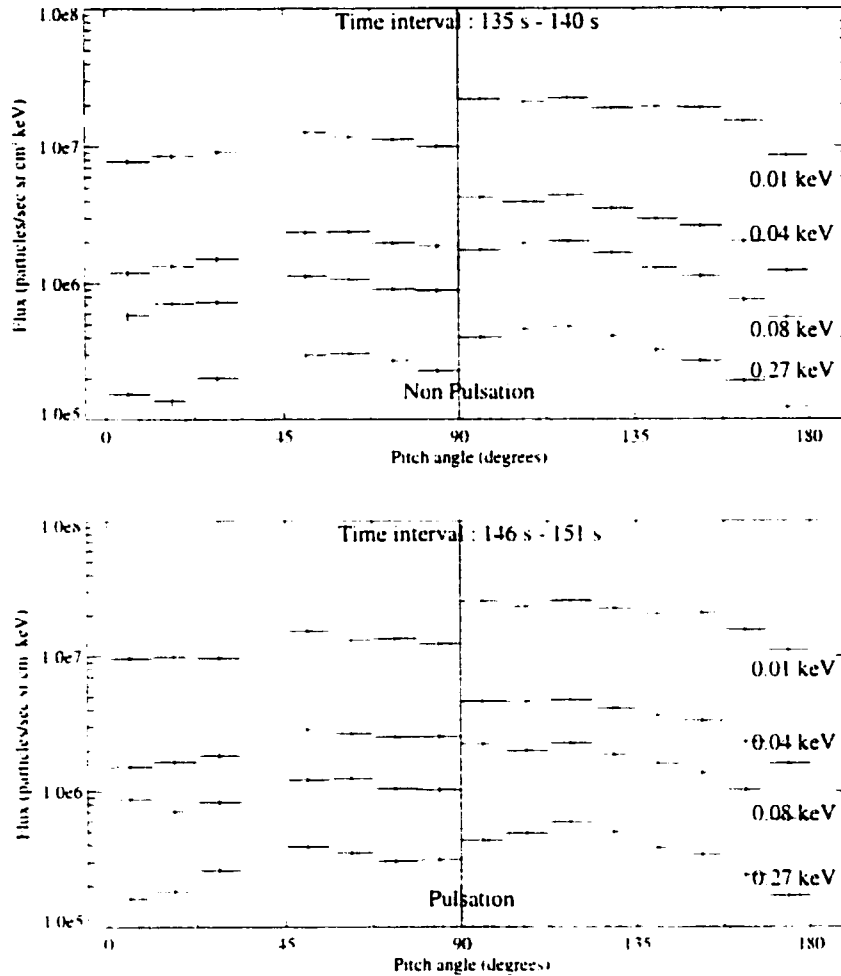


Figure 3.9: Pitch-angle distribution for the pulsation at 146 s after launch and the background at 135 s for energies below 1 keV. The distributions are nearly isotropic but with upgoing fluxes slightly higher than downgoing fluxes.

3.4 Discussion of Low Energy Electron Observations

There are two possible sources for the downgoing low energy (10 eV – 1 keV) electrons. They are either primaries from the magnetosphere associated with the pulsation precipitation or secondaries produced in the ionosphere by the

more energetic precipitated electrons. *Evans and Moore* [1979] have shown that they can account for the low energy ($E < 1$ keV) electrons as secondaries associated with the diffuse aurora. Even though our observations are of pulsating aurora, we also favor the interpretation that the low energy electrons are secondaries which were produced in the dense ionosphere below the rocket by the more energetic primaries. We believe this is the case for both unstructured background fluxes as well as pulsation events.

The examination of the low energy differential energy spectra and the pitch-angle distributions are key to drawing our conclusion. We note that the low energy up- and downgoing spectra are nearly identical, as shown in Figure 3.8. The energy spectra of the upgoing electrons fit a power law form ($\gamma = -1.3$) which is characteristic of secondary electrons that have been scattered off a diffuse gas (ionosphere) and travel upward [*Evans and Moore*, 1979; *Evans et al.*, 1987; *Prasad et al.*, 1983]. Measurements of low energy power law parameters in high latitudes range from $\gamma = -0.9$ to $\gamma = -1.46$ [*Evans and Moore*, 1979]. Our measurement of the energy spectra fall within this range.

We measure nearly identical energy spectra in the up- and downgoing electrons and, although the fluxes are slightly different, the pitch-angle distributions are isotropic and also nearly identical. These are features of secondary electron distributions and they lead us to conclude that the up- and downgoing electrons are both secondaries. The low energy pulsations are interpreted as signatures impressed onto the atmosphere by the high energy electrons, and retained by the low energy upward pulsations.

Evans and Moore [1979] suggested that the upgoing secondaries produced in the conjugate hemisphere can travel to the opposite hemisphere and appear as downgoing electrons. The downgoing electrons we observe could not have

originated in the southern hemisphere because pulsation structures in the low energies are detected at the same time (to within 1 second) as the electrons with energies greater than a few keV. For 20 eV electrons, the bounce period for $L = 6$, where the observations were made, is ~ 40 s and if the electrons came from the southern hemisphere, one would have observed time dispersion in the arrival of different energies, which was not observed. The simplest interpretation for the low energy downgoing electrons we observed is that they were originally produced below the rocket. We propose that the downgoing secondary electron fluxes we detected are due to a potential structure above the rocket that is reversing the trajectories of upgoing electrons which then travel back toward the ionosphere where they are detected as downgoing electrons.

An estimate of the farthest distance from the parallel potential drop to the rocket is given as $x = \frac{1}{2}v\delta t \pm \frac{1}{2}(\delta t^2\sigma_v^2 + v^2\sigma_{\delta t}^2)^{1/2}$, where v is the electron velocity for the 0.02 keV electrons, δt is the difference in arrival time between the up- and downgoing electrons, which from Figure 3.7 is zero, σ_v is related to the energy bin width and $\sigma_{\delta t}$ is the uncertainty in the arrival time of the pulsation and is ~ 1 second. Using the above relation and the energies from Figure 3.7 we estimate the parallel potential region to be not greater than 1300 km from the rocket.

Having hypothesized that a potential is present above the rocket, we can estimate the strength of this potential. First note that the pitch-angle distributions of electrons with energies < 1 keV are slightly anisotropic whereas higher energy electrons ($E > 2$ keV) show a loss cone type distribution (see Section 3.2.4). Secondly, the similarity between the upgoing and downgoing energy spectra only occurs for energies less than ~ 1 keV. These features suggest that the potential is 1.5 ± 0.5 kV.

We base this assertion on the similarity of the low energy up- and downgoing electron spectra. This is a departure from the interpretation of *Evans* [1974]; *Evans and Moore* [1979]. Our data show no evidence of a localized intensity maxima in the energy spectrum but the 1.5 ± 0.5 kV potential is smaller than typically seen in inverted V structures (a few keV) and the small peak may be buried in the rising flux of low energy electrons.

Although the potential drop was observed during pulsation events, it is unlikely to be associated with the pulsation precipitation mechanism itself for two reasons. The first is because the energy spectra of both up- and downgoing electrons are similar for pulsation times as well as for non-pulsation times. Secondly, the low energy spectra do not change shape, only magnitude during a pulsation event. We speculate that the potential is very likely to be associated with the weak auroral structure (As seen in the UVI images of Figure 3.2) which persisted during the time pulsations were detected.

Finally, given that the pulsations were seen in all energy channels in the field aligned direction, it becomes clear that even if there were no potential drop and our explanation is completely incorrect, the pulsation mechanism modulated electrons down to at least 1 keV. This statement is due to the following line of reasoning. Firstly, if there is no potential drop, then the simplest explanation for the changes in the low energy downgoing precipitation is that whatever source mechanism responsible for modulating the higher energy electrons is also modulating the low energy electrons. The reason for this statement is that the timing of the pulses in the low energy channels rules out backscattered electrons from the conjugate hemisphere as the source. We have also ruled out a local source for the electron modulation. So, if there is no potential, then we still think that the modulation mechanism is responsible for modulating the low energy electrons all the way down to 10's of eV.

If, on the other hand, there is a potential structure located above the rocket then the potential drop accelerated all electrons which went through it. In that case, the low energy electrons ($E < 1 \text{ keV}$) really are due to reflections between the lower ionosphere and the potential drop. It is possible that the modulation mechanism is in fact, modulating electrons down to 10's of eV's but we cannot distinguish between the reflected secondary electrons and any low energy electrons which came through the potential since they both have the same energy and the same temporal structure.

In order to find the energy of the electrons before they were accelerated by the potential, we subtract the energy that the potential gave to the electrons. Thus, if the potential was 1 kV and we measured modulated electrons at 1.5 keV, the electrons were modulated all the way down to 0.5 keV. Since the energy bin width of the ESA around the energy of the potential drop is roughly 400 eV, we can estimate that the modulation occurred for electrons of energy down to 100's of eV. Since we have not actually measured the magnitude of the potential drop, prudence dictates that we give our estimate of the lowest modulated energy as 1 keV. While this line of reasoning cannot provide exact low energy boundaries for modulation mechanism, we are confident that low energy electron modulations occurred.

It is difficult to see other mechanisms that can produce these modulated electrons. Any upgoing electrons with an energy that is larger than the potential will pass through the potential barrier and not be reflected. Therefore, any electrons with energies just above the potential must have come straight from the magnetospheric source above the rocket. If this is the case, then the electrons have to be modulated by the source mechanism (still unidentified).

3.5 Intermediate Energy Electrons ($1 \text{ keV} < E < 5 \text{ keV}$)

Figure 3.10 shows a plot of selected energies for the pulsation time at 146 s for all of the downgoing directions. Once again, the error bars indicate 1σ uncertainties due to Poisson statistics. Since the fluxes in this energy regime are so similar we have multiplied the flux at each energy by a factor. For the field aligned direction, these energy channels show evidence of the pulsation but for the non-field aligned directions these energy channels show no pulsation signature.

Figure 3.11 shows a portion of the energy spectra for the intermediate energies for pitch-angles of 6° and 174° for both the pulsation at 146 s and the background at 135 s after launch. Unlike the energy spectra in Figure 3.8, the downgoing electrons have a higher flux than the upgoing electrons for both the pulsations and the background. We note however, that the difference between the upgoing and downgoing flux is very small (a factor of 2 or smaller). This feature is somewhat surprising since the flux of these upgoing intermediate energy electrons is expected to be much smaller than the downgoing flux. The reason for this is that the cold ionosphere does not contain electrons of this energy and so they are either coming from somewhere else or somehow the ionosphere is producing them.

Figure 3.12 shows the pitch-angle distribution for the intermediate energies for the pulsation time at 146 s and the unstructured background precipitation at 135 s for energies between 1 and 5 keV. The pitch-angle distribution is highly anisotropic. For $0^\circ - 90^\circ$ pitch-angles, the fluxes decrease sharply, (by nearly an order of magnitude) from $\sim 50^\circ$ to 0° . For pitch-angles greater than 90° the distributions are less anisotropic. Note also the fluxes for both the pulsation and the background show small variations among the different energies which

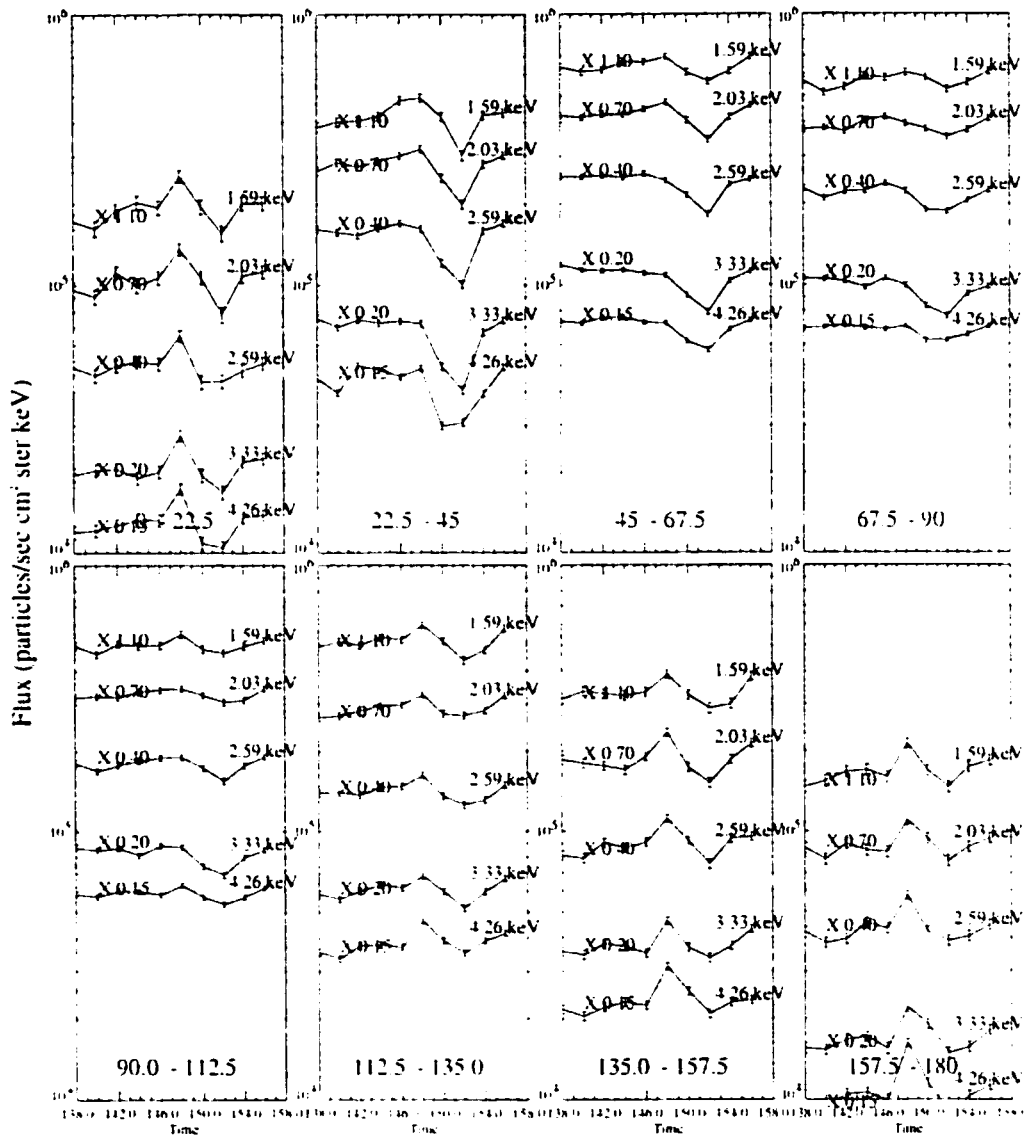


Figure 3.10: Particle flux as a function of time for downgoing pitch-angles and selected energies for the pulsation at 146 s. The fluxes in this energy were so similar that we have multiplied the energy channels by constants so that they could be more easily inspected. The factor multiplying each flux is shown on the left side of each trace.

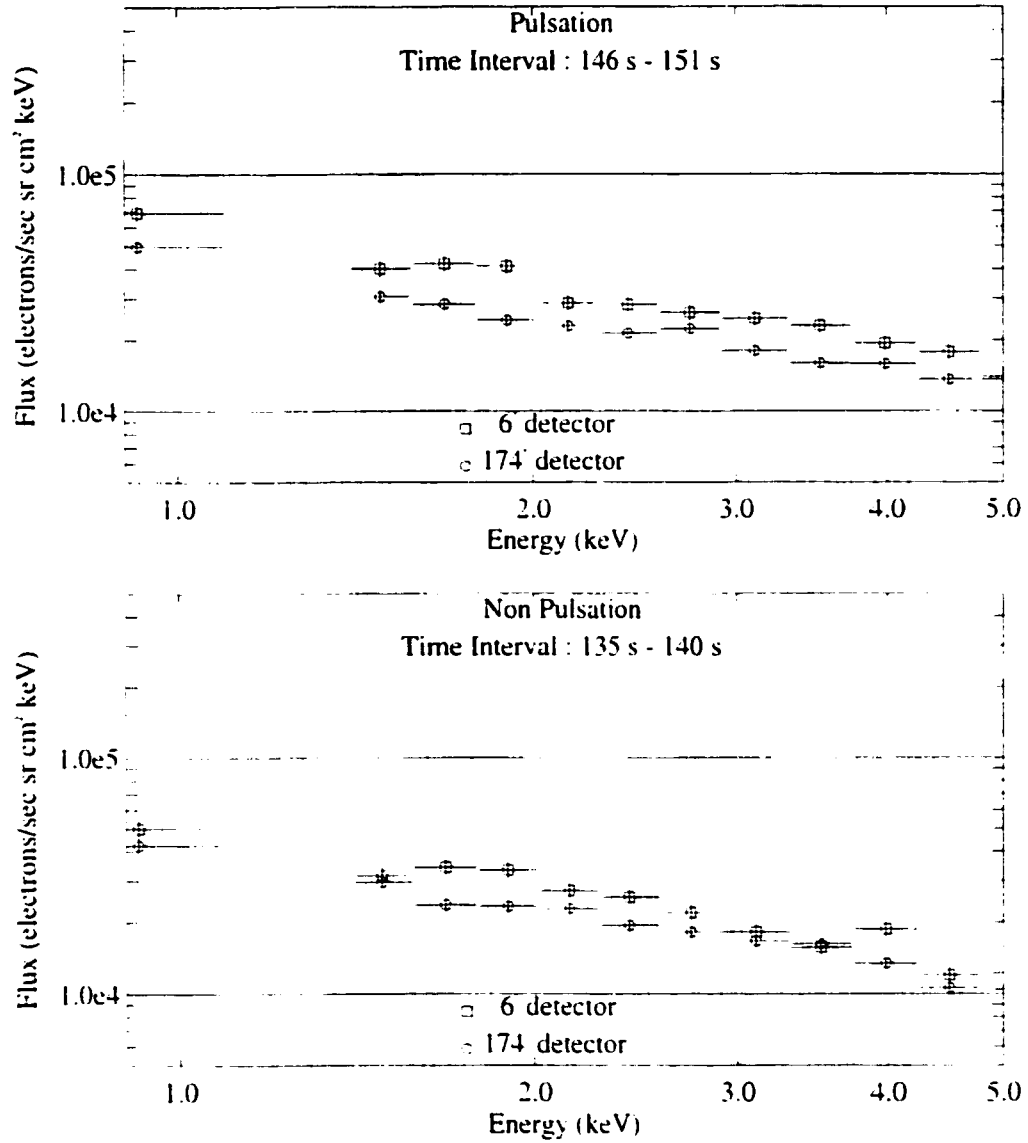


Figure 3.11: Intermediate energy spectra for pulsation at 146 s and the background at 135 s for the 6° and 174° pitch-angles.

is consistent with the energy spectra shown in Figure 3.11.

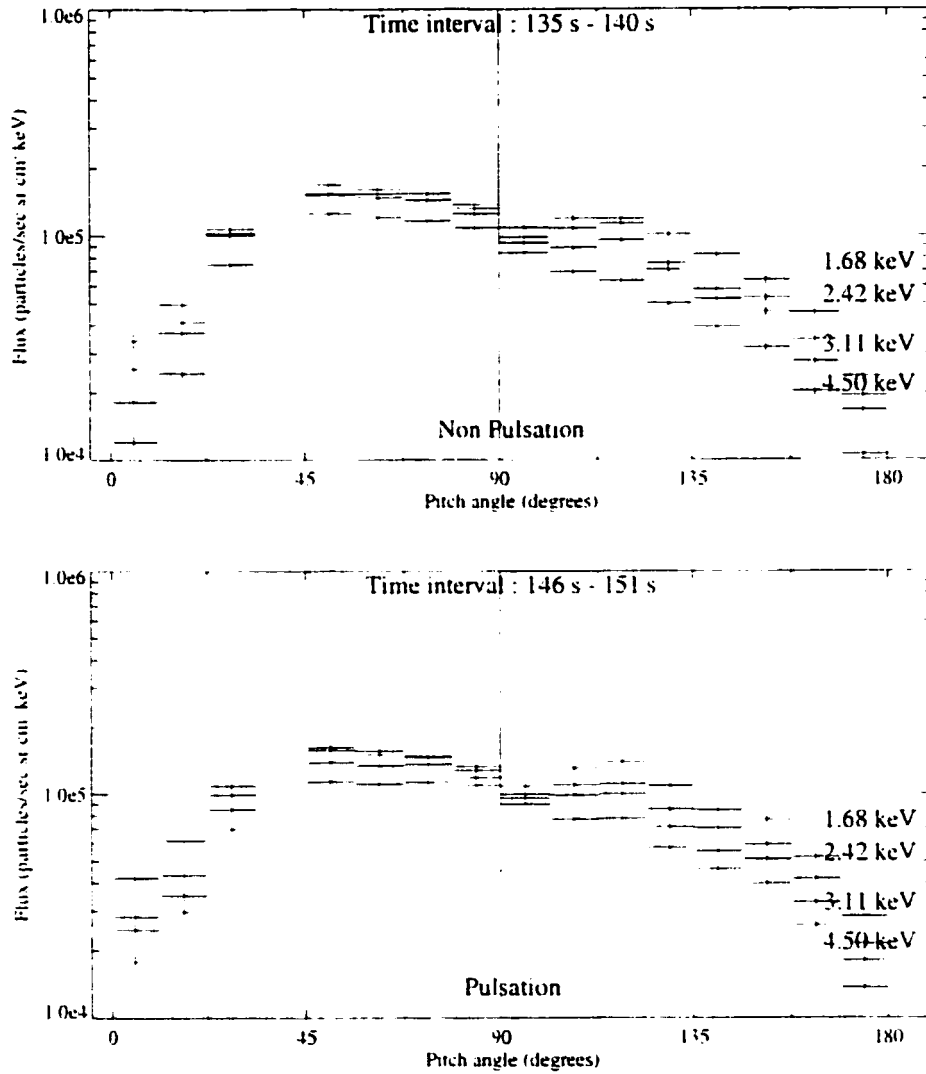


Figure 3.12: Intermediate pitch-angle distribution for pulsation times at 146 s and the background at 135 s. The fluxes from the different energies at large pitch-angles are nearly equal, which is consistent with the plateau feature in the energy spectra

3.6 Discussion of Intermediate Energy Electrons

The intermediate energy electron flux shows no pulsation modulations for any downgoing pitch-angles that are not field aligned, while the field aligned electrons show modulation for all of the intermediate energies. We do not understand why pulsations are observed in the field aligned direction but not in any of the other downgoing pitch-angles. It is possible that there are multiple processes occurring and this possibility will be further developed in Chapter 4.

The upgoing electrons show pulsation modulation at all pitch-angles. This feature is seen in the higher energies ($E > 5$ keV) as well. We do not know why we see pulsations (or even the unstructured background flux levels that were observed) at these high energies. Secondary and backscattered electrons (here we simply call them upgoing electrons) are expected to have an order of magnitude less flux than downgoing electrons [*Lummerzheim and Lilensten, 1994*] at these altitudes, yet the fluxes we see only differ by a factor of two or less. Some dynamical process appears to be operating in the ionosphere below the rocket to cause these features and whatever it is does not depend on the pulsations themselves since we see the same feature in the background as well.

The spectra here are basically flat, but do show variation with pitch-angle as is seen by comparing the top and bottom panels of Figure 3.6. The pitch-angle distributions for this energy range appear to be a sort of transition between the nearly isotropic pitch-angle distributions at low energies and the more highly anisotropic pitch-angle distributions seen at higher energies ($E > 5$ keV).

3.7 High Energy Electrons ($E > 5$ keV)

Examples of pulsations with energies from 5 keV to 26 keV are shown for eight different pitch-angles in Figure 3.13. Fluxes from six different energy channels are shown in each panel. The fluxes are two second averages and the error bars are due to Poisson statistics. The upper left panel shows electrons traveling along the magnetic field direction (pitch-angle of $0^\circ - 22^\circ$) and the bottom right shows electrons with pitch-angles of $157^\circ - 180^\circ$. The amplitude of the pulsations is strongly dependent on the pitch-angle and energy. For example, the largest peak to valley ratio for this pulsation is seen in the $22.5 - 45^\circ$ detector. Of extreme interest is the observation of pulsation structure in the electrons coming out of the ionosphere at nearly anti-field aligned directions with energies up to 26 keV. While the peak-to-valley ratio for these electrons is not as high as for the precipitating electrons, that upward going pulsation exist at all for this energy is quite extraordinary. Note also the pulsations appear promptly in all energy channels without observable time delay (to be discussed further in Section 3.10 on velocity dispersion).

Figure 3.14 shows a plot of the energy spectra for energies $5 \text{ keV} < E < 25 \text{ keV}$ obtained during the pulsation at 146 s for the 6° and 174° electrons as well as for the unstructured background at 135 s. The spectra in this energy range are steeply falling. The pulsations in the downward direction are slightly higher than the upward fluxes. Note also that the fluxes of the background upgoing electrons are nearly equal to the downgoing pulsation flux.

To study this feature further, we show the pitch-angle distributions for the pulsation at 146 s and the background at 135 s in Figure 3.15. The distributions for the four selected energies show a large anisotropy with fluxes decreasing rapidly for pitch-angles less than 50° and less rapidly for pitch-angles greater

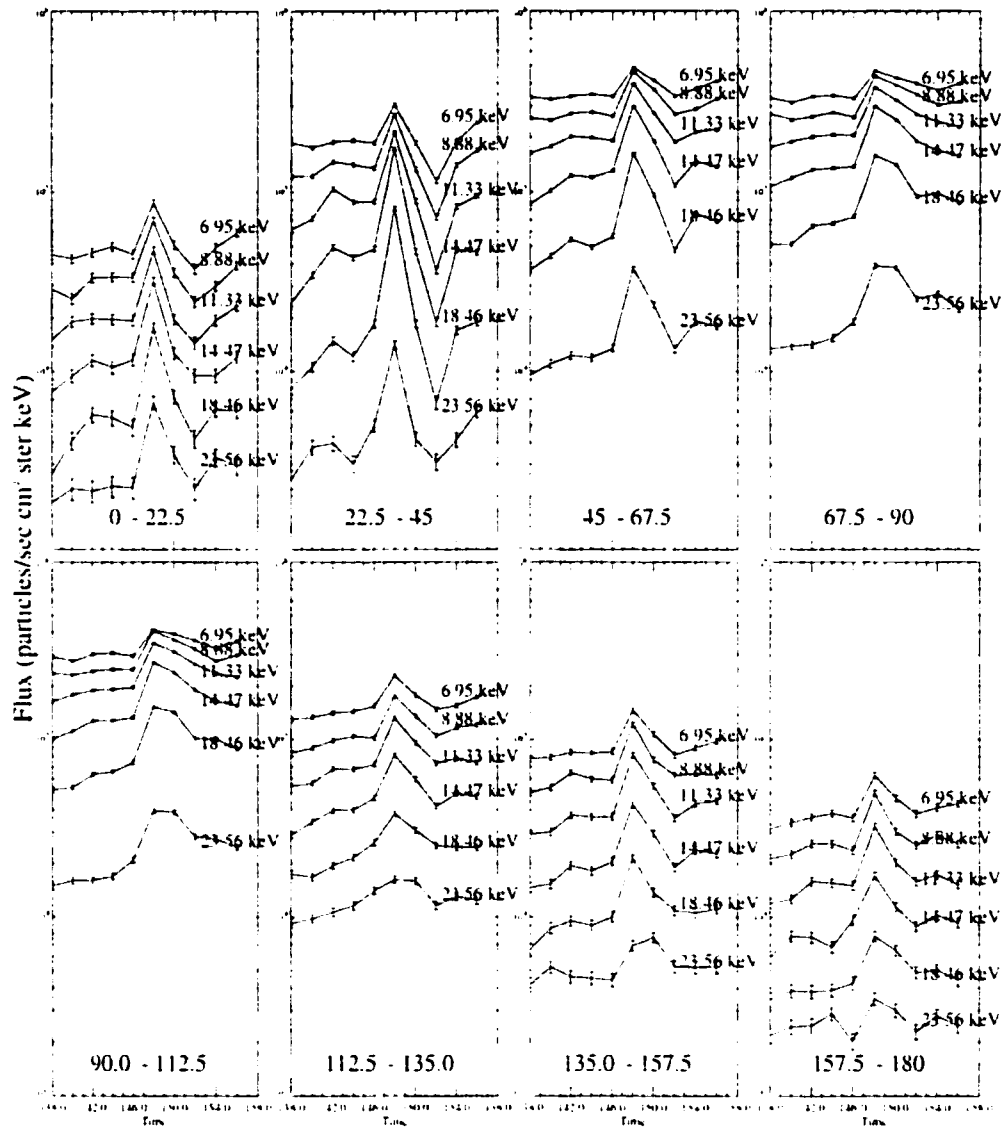


Figure 3.13: Particle flux as a function of time and pitch-angle for selected energies ($E > 5$ keV).

than 90° . The high energy pitch-angle distribution for electrons $< 90^\circ$ is characteristic of the loss cone distribution with the loss cone estimated at $\sim 50^\circ$.

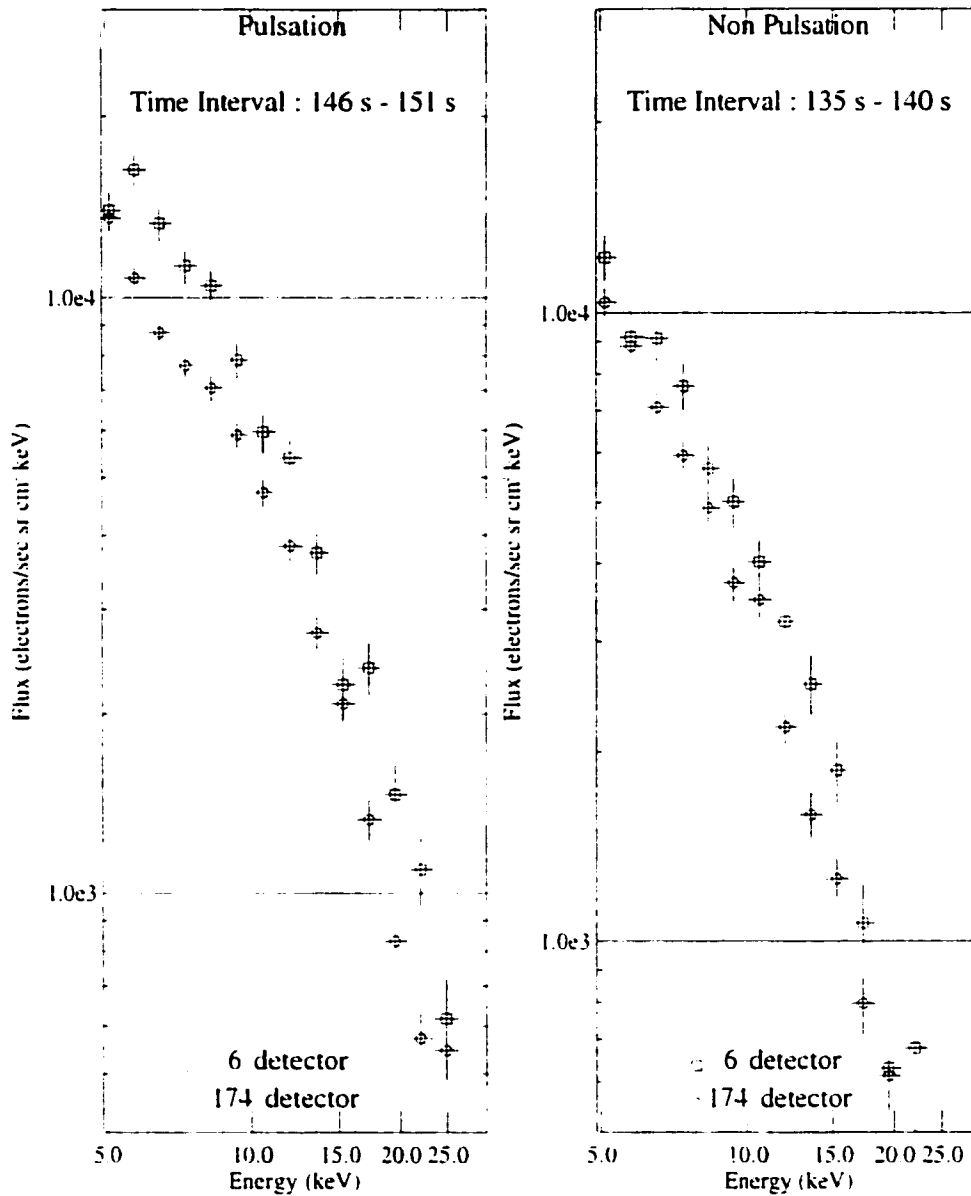


Figure 3.14: Energy spectra for electrons at 6° and 174° for the pulsation at 146 s and background at 135 s for energies between 5 and 25 keV.

There are substantial fluxes of electrons moving upward away from the ionosphere. In normal situations, the particles in the loss cone mirror below the

ionosphere and thus these electrons are absorbed by the atmosphere and there should not be electrons with pitch-angles greater than 130° . Our observations of significant flux moving away from the ionosphere indicates the ionosphere below the rocket was dynamic, more than normally expected. This topic will be discussed in more detail in Section 3.9.

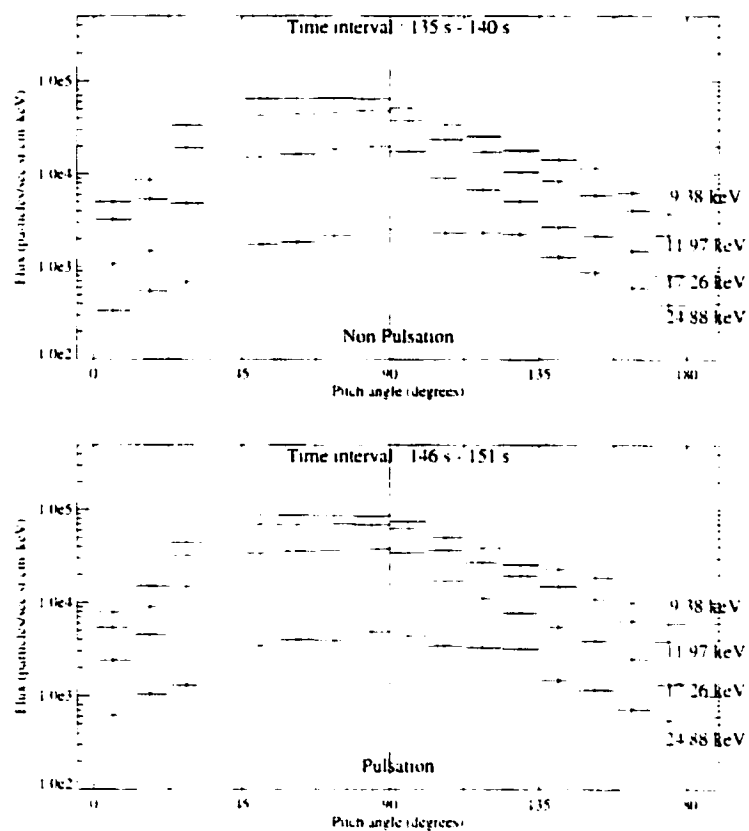


Figure 3.15: High energy pitch-angle distribution for the pulsation at 146 s and the background at 135 s. The flux of electrons out of the ionosphere is almost as large as the flux going into the ionosphere.

To quantify the anisotropy of the pitch-angle distributions for the downgoing electrons, Figure 3.16 shows a plot of the anisotropy during the pulsation at 146 s. We define the anisotropy as

$$A = F_{\perp}/F_{\parallel} - 1$$

where F_{\perp} represents the flux of electrons with 90° pitch-angles and F_{\parallel} the flux traveling along the magnetic field with 0° pitch-angles. The ratio is roughly one for energies up to approximately 1 keV and corroborates the observations shown earlier that the low energy electrons are nearly isotropic. The departure of isotropy occurs around 1 keV and maximizes around 10 keV. It then decreases rapidly to less than 5 at 30 keV. These results indicate that anisotropy in pulsations is energy dependent and at energies greater than 10 keV, the pitch-angle distribution tends toward isotropy.

The behavior of the anisotropy is illustrated another way in Figure 3.17, which shows the pitch-angle anisotropy as a function of time from 138 s to 158 s, which includes the pulsation at 146 s. The behavior of the three energies shown here are characteristic of all energies above 5 keV. The vertical error bars are due to Poisson statistics. The fourth panel shows the total energy flux integrated over all the downgoing electrons. What is important here is that the anisotropy always drops down during a pulsation event and then slowly climbs back to pre-pulsation values. This lessening of the anisotropy during pulsations is indicative of a process such as a wave-particle interaction which partially fills the loss cone.

Figure 3.18 shows a plot of the difference in count rate (or energy flux) between the pulsation at 146 s and the background at 135 s as a function of energy and pitch-angle in the spectrogram format. This figure shows that the largest change between pulsation and background occurs between 50° and 90° for energies between 10 and 20 keV. The dark area located at pitch-angles between 22° and 90° and energies from 2 to 5 keV is the plateau region discussed in the

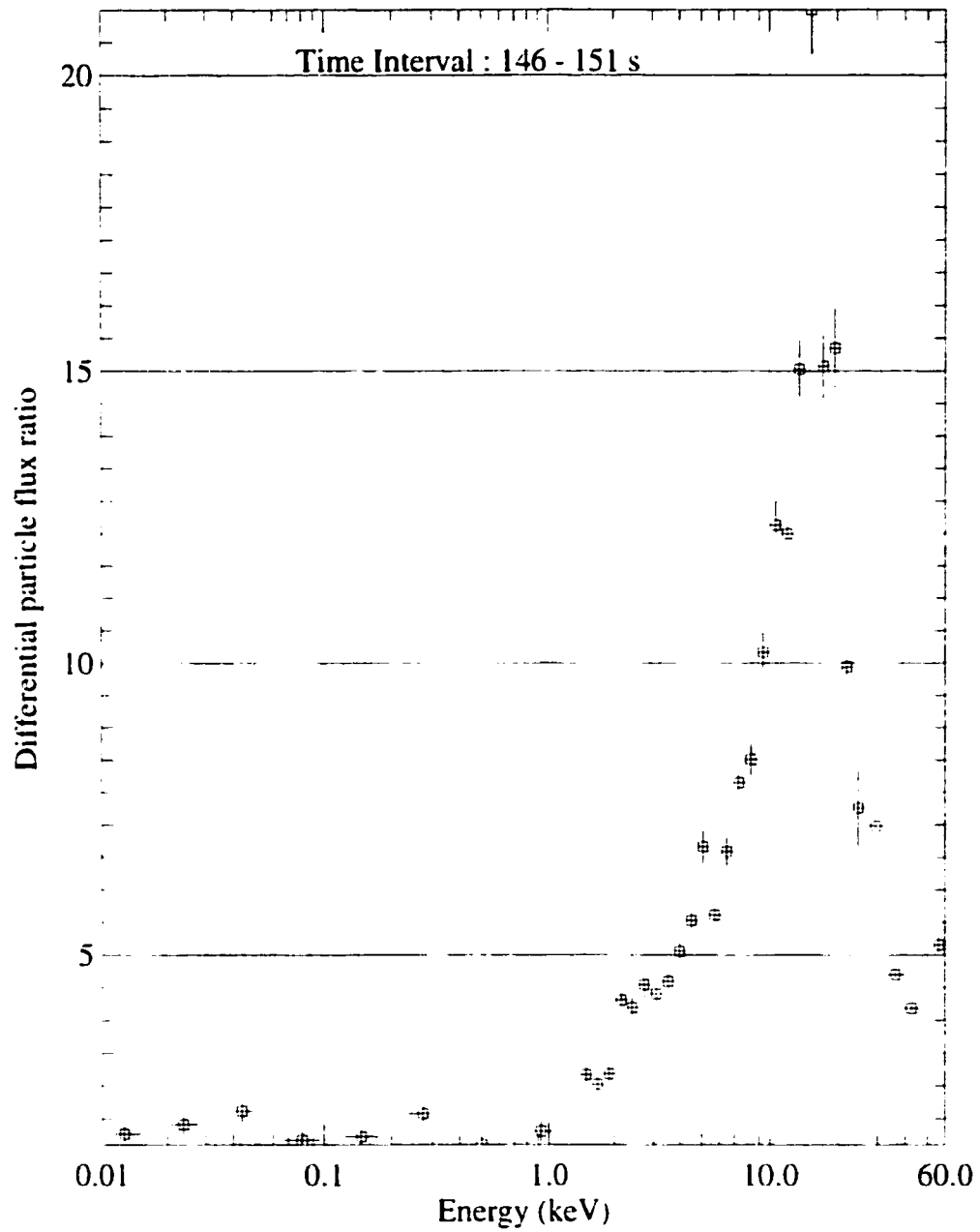


Figure 3.16: Ratio of the flux at 90° to 0° for the pulsation at 146 s. This plot shows a measure of the pitch-angle anisotropy

previous section. Similar plots were made for all of the pulsations and in eight of the nine cases, the results were very similar to what is shown here. Only

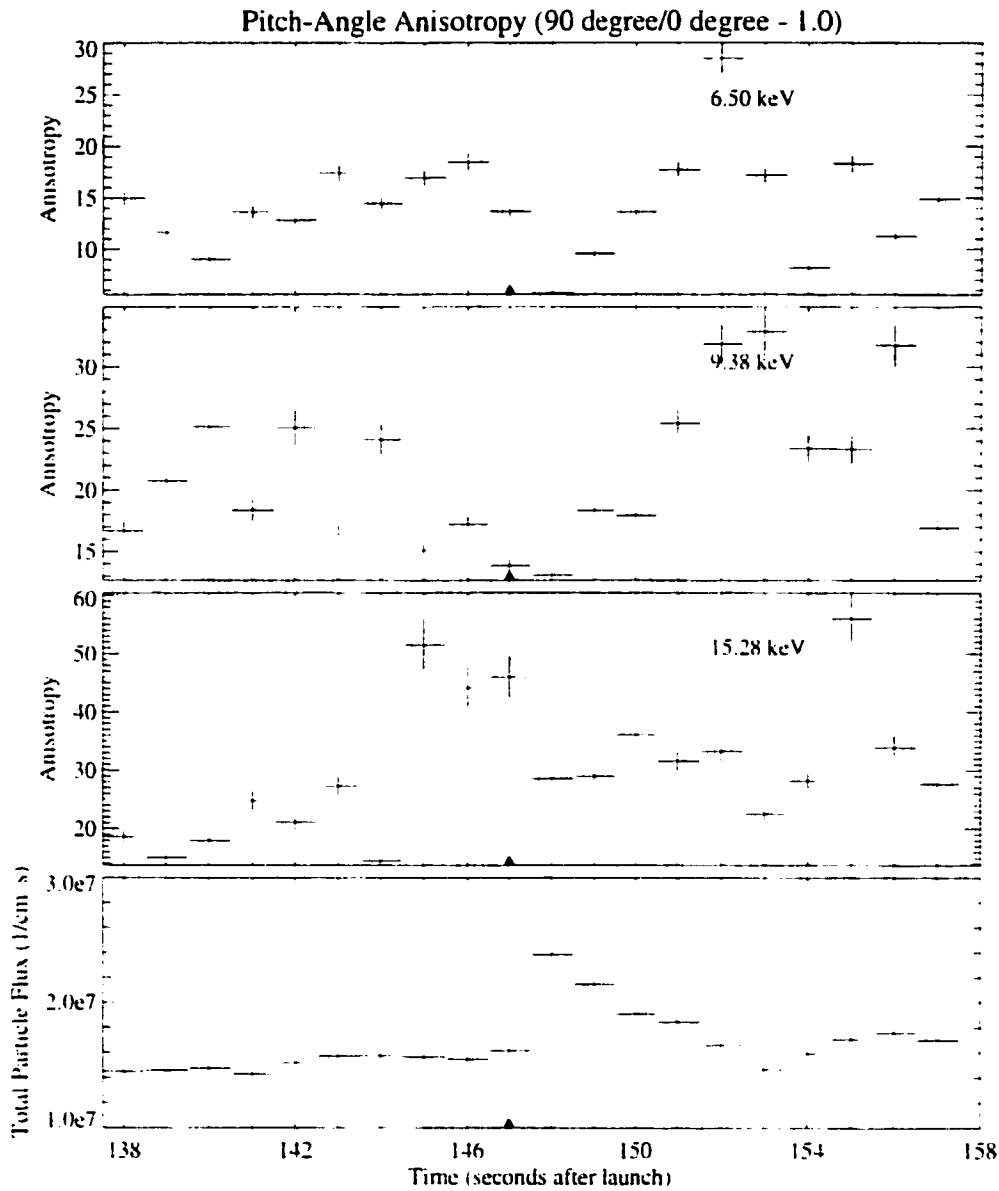


Figure 3.17: Pitch-angle anisotropy versus time for selected energies for the time interval of 138 s to 158 s. The bottom panel shows a plot of the total downward particle flux so that the changes in the anisotropy may be compared with the changes in particle flux. The start of the pulsation is marked by the upward pointing triangle.

the last pulsation, which was the weakest and most difficult to identify, did not show this behavior. This plot compactly shows what pitch-angles and energies are most modulated during a pulsation event.

Figure 3.19 shows a plot of the difference between the pulsation at 146 s and the unstructured background precipitation at 135 s for selected energies. This plot is produced by taking vertical cuts in Figure 3.18 and shows the quantitative change between pulsation and background as a function of pitch-angle. The largest changes all of the energies occur for pitch-angles between 50° and 90°. Comparison of the difference at 24.88 keV with the other energies shows that the magnitude of the difference is dropping off for the higher energies.

3.8 Maxwellian Fits to the High Energy Electrons

Figure 3.20 shows energy spectra from the 62° direction for both the pulsation at 146 s and the unstructured background at 135 s. Included on this plot is the difference spectra obtained by subtracting the background flux from the pulsation flux for energies between 5 and 25 keV. This is a quantitative measure of a cut taken in the horizontal direction of Figure 3.18. The resulting spectra is a quantitative measure of the particle flux as a function of energy for the pulsation itself. The peak of this difference spectra occurs at ~ 15 keV. Similar results are obtained for other pulsations and also in other look directions.

Figure 3.20 also shows fits of the spectra to Maxwellian particle flux distributions of the form:

$$j(E) = AEE_0^{-3/2} \exp(-E/E_0).$$

where $j(E)$ is the energy dependent particle flux, “=” is the symbol denoting

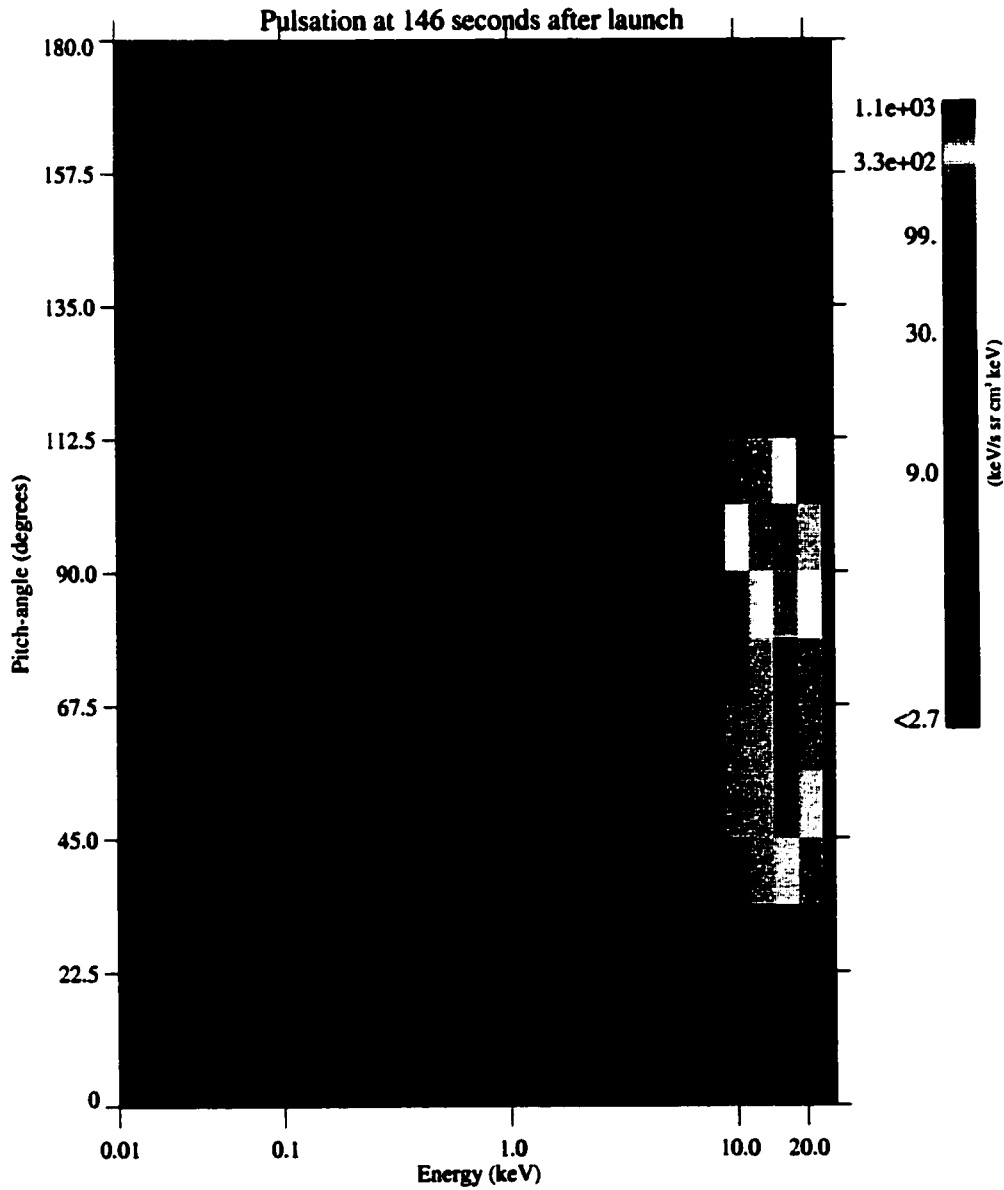


Figure 3.18: Energy Flux difference between the pulsation at 146 s and the background at 135 s as a function of pitch-angle and energy. The greatest change occurs for energies between 10 and 20 keV for pitch-angles between 50 and 90°.

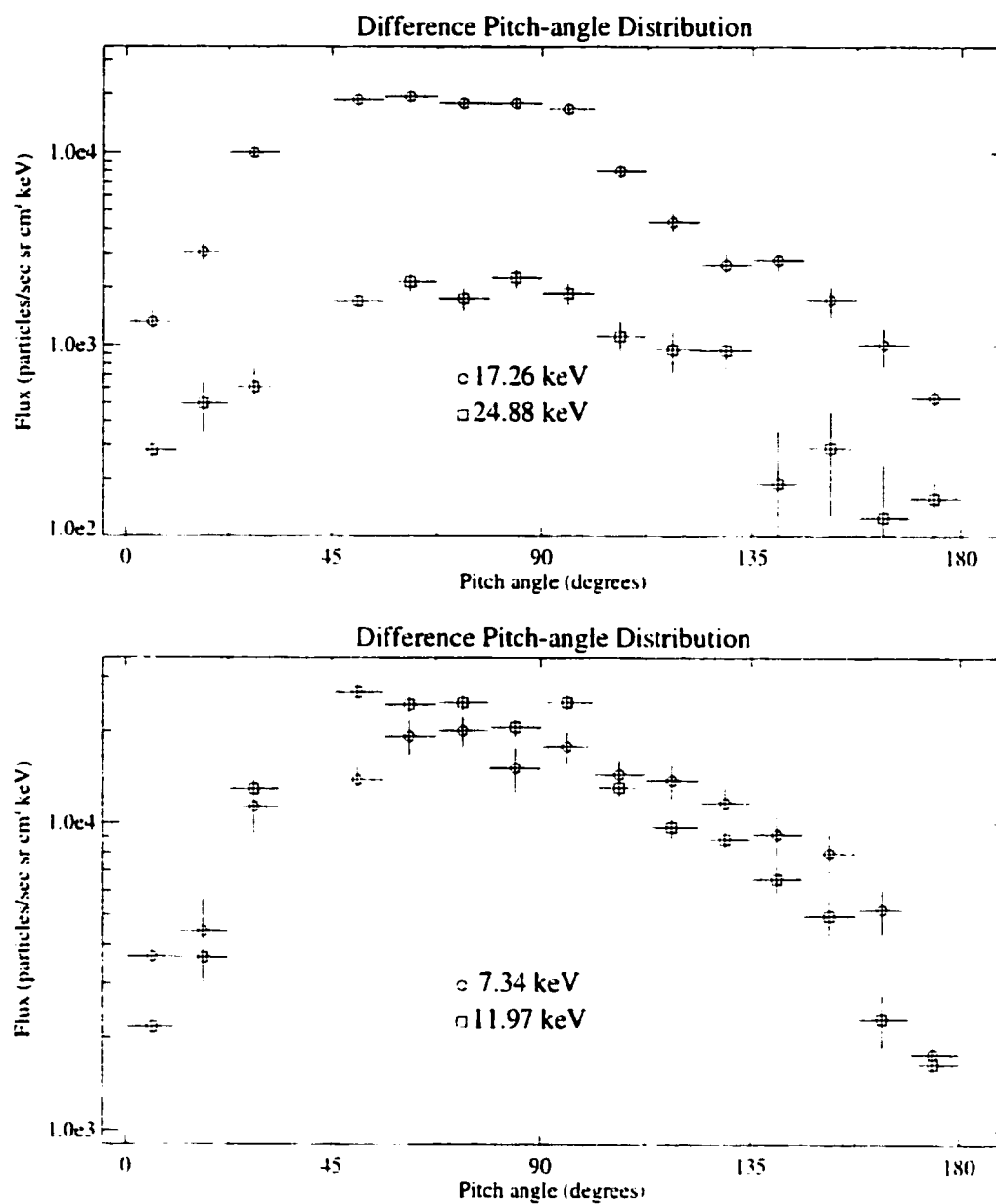


Figure 3.19: Difference pitch-angle distribution for selected energies for the pulsation at 146 s. The largest change occurs for electrons between 50° and 90° pitch-angles.

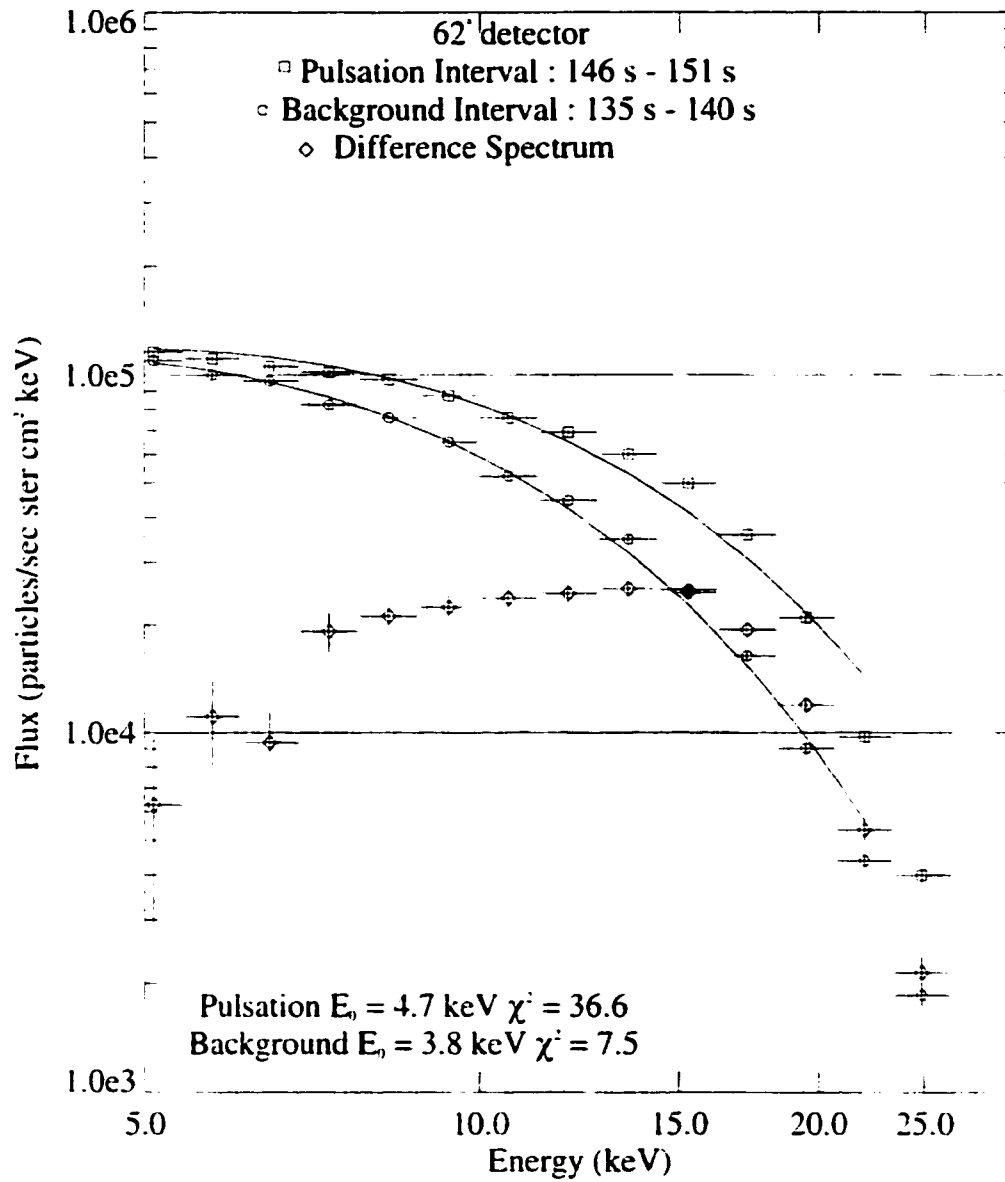


Figure 3.20: Energy spectra from 5 to 25 keV for the 62° direction for both the pulsation at 146 s and the background at 135 s. The plot also contains the difference spectra as well as fits to Maxwellian distributions.

equality, A is the flux and E_o is the characteristic energy. The fitting procedure was done by a non-linear least squares fit using a gradient-expansion algorithm. The characteristic energy values for both the background and pulsation are given on the plot. Overall E_o increased during a pulsation by approximately 25 percent. The chi-squares χ^2 , to the fits are also given on the plot.

The same fitting procedure was done for all nine pulsations. The results are shown in Table 3.1. This table shows that E_o increased not only between the background and the pulsation event, but also as a function of pitch-angle, where the higher the pitch-angle the higher the characteristic energy. In all of the fits, 15 per pulsation (one fit per pitch-angle bin, only the downgoing are shown in the table) and nine pulsations, the background always had a smaller χ^2 statistic than the pulsation. Basically, this means that while the background energy spectra fit well to a Maxwellian model, the pulsation energy spectra did not fit as well. Nevertheless, the results of the characteristic energy increases are qualitatively correct.

3.9 Discussion of High Energy Electron Observations

The high energy electrons exhibit some very complicated but informative behavior about the pulsations. First, we will discuss the characteristic energy information gained from the energy spectra, next we will discuss the pitch-angle distributions themselves and what they indicate is happening below the rocket and then finally we discuss the downgoing pitch-angle distributions and what they say about the mechanism causing the pulsations.

The characteristic energy fits of the data showed that E_o for the pulsation events always increased in comparison with the background. An increase in

Table 3.1: Table of characteristic energies for all of the pulsations and the background as a function of pitch-angle. All of the values are given in units of keV. The characteristic energies of the pulsations show an increase over the background. The characteristic energy also varies as a function of pitch-angle, with larger pitch-angles having a higher E_o .

Event	Start Time (s)	6°	17°	28°	51°	62°	73°	84°
Background	110	3.29	3.27	3.17	3.55	3.72	3.83	3.94
Pulsation	119	3.84	3.89	4.05	4.32	4.39	4.44	4.56
Background	135	3.57	3.17	3.15	3.71	3.84	3.98	4.17
Pulsation	146	3.77	4.07	4.09	4.58	4.74	4.83	5.01
Background	212	3.52	3.40	3.53	3.93	4.08	4.21	4.35
Pulsation	208	3.92	4.11	4.35	4.64	4.74	4.73	4.93
Background	217	3.65	3.51	3.76	4.12	4.21	4.29	4.37
Pulsation	223	4.01	4.11	4.26	4.62	4.75	4.79	4.97
Background	225	3.91	4.13	4.27	4.65	4.69	4.77	4.84
Pulsation	230	3.96	4.40	4.76	4.98	5.05	5.02	5.13
Background	235	3.91	4.07	4.29	4.48	4.54	4.54	4.63
Pulsation	242	4.04	4.46	4.97	5.20	5.17	5.17	5.25
Background	255	4.01	4.29	4.61	4.83	4.87	4.90	5.01
Pulsation	260	4.14	4.34	4.99	5.29	5.27	5.24	5.37
Background	275	3.81	4.12	4.36	4.68	4.64	4.70	4.79
Pulsation	285	4.11	4.52	5.02	5.27	5.29	5.33	5.41
Background	365	3.94	4.10	4.34	4.70	4.60	4.55	4.72
Pulsation	373	4.30	4.32	4.83	5.32	5.08	5.03	5.14

characteristic energy, or heating, is consistent with a mechanism that compresses the distribution function in the source region. The characteristic energy fits also show that the energy spectra changed as a function of pitch-angle. The energy spectra at low pitch-angles had a smaller characteristic energy than those at high pitch-angles. Examination of Figure 3.6 shows the same feature, the field aligned electron energy spectra have a less pronounced plateau region, which is indicative of a lower E_0 . The characteristic energy information seems to indicate that whatever process is causing the pulsations seems to have a preferred direction, namely at large pitch-angles. Compression of the magnetic field can produce this behavior.

The pitch-angle distributions in Figure 3.15 shows that the high energy particle flux out of the ionosphere is comparable to the flux into the ionosphere. Reports of similar observations [McDiarmid *et al.*, 1961; Cummings *et al.*, 1966] have been rare. These authors reported on reflection ratios for electrons with energies over 40 keV. A reflection ratio can be considered to be the ratio of flux at 180° to 0° . In some cases [Cummings *et al.*, 1966] reflection ratios over one were observed. These authors considered radial diffusion from higher density nearby flux tubes, ionospheric currents, and upward moving bremsstrahlung as a way to produce the observed fluxes.

In our observations we can rule out these mechanisms. Our experiment took place during a diffuse auroral event and from looking at the all-sky camera images we saw that there are no high density flux tubes located next to lower density tubes, as would be the case for discrete auroral events. Therefore, we do not think that high upward flux to be caused by radial diffusion applies to our observations. Likewise, the magnetometer data showed no evidence of strong current systems overhead, either at Poker Flat or Ft. Yukon.

The ionosphere itself is too cold to actually contain electrons of these energies. It is possible that some kind of strong electromagnetic field may cause the electrons to be reflected out of the ionosphere. Such a field might be produced by the flux of electrons into the ionosphere. The flux of electrons into the ionosphere would excite a localized plasma instability which could conceivably produce electromagnetic waves of high enough amplitude to cause the reflections. *Hallinan et al.* [1985] has suggested that a beam-plasma instability may be excited in this region of the ionosphere under just these circumstances. The frequency of the excited waves is similar to the plasma frequency in this region (frequencies on the order of a MHz).

The pitch-angle distributions in Figure 3.15 shows that the loss cone of the downgoing electrons appears to be around 50° . The loss cone for a dipole magnetic field at this altitude is approximately 70° . The magnetic field that night was not highly disturbed and we were on field lines that would normally be considered dipolar. The difference cannot be attributed to the 1 kV potential above the rocket, since the pitch-angle distributions at $E > 5$ keV all showed the same feature and a 1 kV potential does not affect these high energy electrons enough to change the distribution to what was observed. The fact that the loss cone appeared at 50° for all of the higher energies indicates that whatever changed the loss cone was not energy dependent.

Examination of Figure 3.19 shows that the largest change in the pitch-angle distribution between the background and the pulsation came at approximately $50^\circ - 90^\circ$. Many observations [*Bryant et al.*, 1975; *Smith et al.*, 1980] have shown that the pitch-angle distribution becomes isotropic during a pulsation. This means that starting with a loss cone type distribution the greatest change would have to be in the field aligned direction, which is not what we observed. While we see a change in the field aligned direction (see Figure 3.17), it is not

as large as that at 50° .

The large change at 50° , which is near the observed loss cone, may indicate that whatever mechanism is causing the pulsations only weakly affects the electrons so that they cannot diffuse enough to fill in the entire loss cone, that is, the mechanism must be weakly diffusive. Figure 3.17 corroborates this assertion, since the anisotropy during pulsations never goes to values close to one.

3.10 Velocity Dispersion

Figure 3.21 shows a plot of the particle flux from 138 – 158 seconds after launch for five different energy channels for electrons 67.5° from the magnetic field. During this time period the pulsation at 146 seconds occurred. The plot shows that the leading edge of the pulsations all start at the same time. The peak is also reached at the same time. As stated in Chapter 1 many workers [*Bryant et al.*, 1967, 1975] have seen evidence of velocity dispersion, that is, high energy particles arrive before low energy particles. For this pulsation and the others we detected, all energy channels show the same initial rise time and no evidence of velocity dispersion.

In order to quantify the arrival times of the pulsations, a cross correlation of the different energy channels was performed. Computing the cross correlation of two different energy channels allows the determination of how the two time series are related in terms of lag time. Then, using the time lags obtained from the cross correlations, the distance from the source of the modulation to the rocket can be found.

Figure 3.22 shows a plot of the computed cross correlation between two differ-

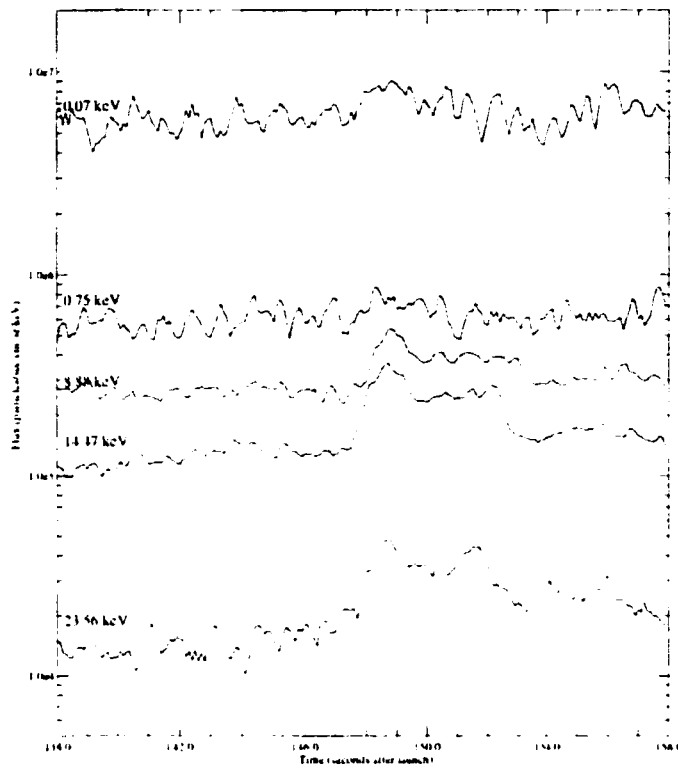


Figure 3.21: Plot of the particle flux for the pulsation at 146 s after launch. The plot shows five different energy channels ranging in energy from 0.07 keV to 24 keV. This figure shows no evidence of velocity dispersion.

ent energy channels ($E_1 = 24$ keV and $E_2 = 8$ keV) for the pulsation observed at 146 seconds after launch. The highest time resolution available is used so as to get the best estimate of any possible time lag. In order to correlate the two different time series each was filtered using a 3 point running average and the pitch-angle channels centering on 67.5° were added together in order to improve the statistics.

Figure 3.22 shows that for the two different energies the peak correlation corresponds to a zero time lag. This means that the pulsations arrived within the time resolution of the detectors, which is 50 milliseconds. The same correlation

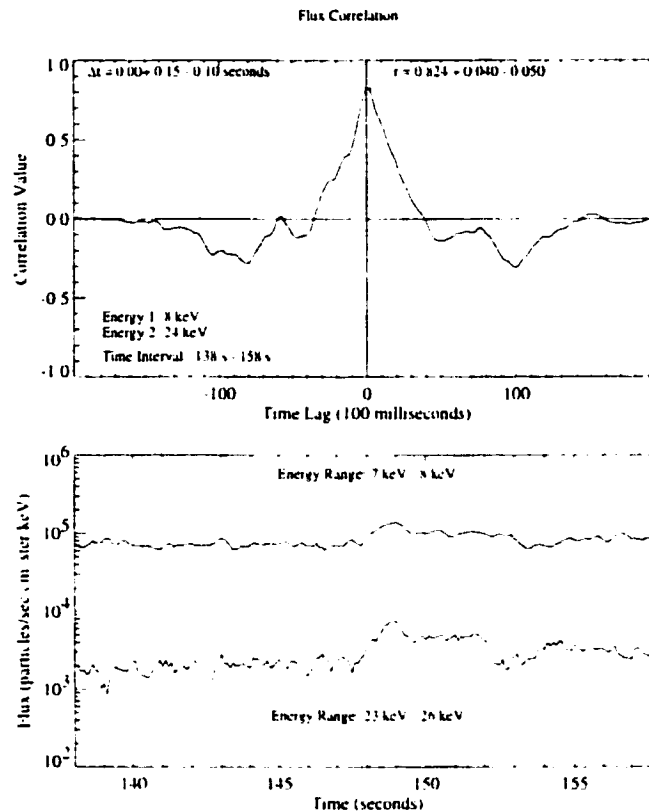


Figure 3.22: Cross correlation for two energy channels for the pulsation at 146 seconds after launch for electrons 67.5° from the magnetic field. The upper panel shows the correlation integral and both the correlation coefficient and the time lag. The uncertainties are calculated as described in the text

analysis was performed for each of the nine pulsations. In no single case was there a clear signature of a velocity dispersion.

In order to assess the validity of the cross correlation coefficient the z-transform method of Fisher [Steel and Torrie, 1960] has been implemented. As this method is only valid on normally distributed data we further checked that the data were sampled from a normal distribution. The uncertainty in the lag time is estimated by finding all lags that have a higher value for the correlation coefficient than the lowest value of the peak correlation coefficient. For example,

if a particular peak of the correlation integral is 0.9 ± 0.05 then we find all time lags which have a correlation of 0.85 or higher. In this way, a conservative estimate of the largest time lag possible is obtained.

The Fisher method gives a measure of the uncertainty in the correlation coefficient by transforming the sampled cross correlation values back to the parent population. In the parent population we are able to accurately determine the uncertainty of the correlation coefficient, then we simply transform the uncertainties back to the sampled population.

Given that a time lag between two different energy channels can be measured then the distance from the source of the modulation to the rocket can be determined. This procedure requires a few assumptions. The most important are that the modulation region is small in size and that the electrons are all modulated simultaneously. Given these two assumptions it is a simple task to find the distance from the modulation source to the rocket. The relation which determines this is given as:

$$\text{distance} = \frac{\left(\frac{2}{m}\right)^{1/2} (E_1 E_2)^{1/2}}{(E_1^{1/2} - E_2^{1/2})} \left(\Delta t \pm \left[\frac{m(\Delta t)^2}{2} K + \sigma_{t_1}^2 + \sigma_{t_2}^2 \right]^{1/2} \right).$$

where

$$K = \left(\frac{\sigma_{E_1}^2}{E_1} + \frac{\sigma_{E_2}^2}{E_2} + \frac{\sigma_{E_1}^2 + \sigma_{E_2}^2}{(E_1^{1/2} - E_2^{1/2})^2} \right).$$

E_1 and E_2 are the different energy channels, Δt is the difference in arrival time for the pulsation between the two energy channels, m is the electron mass, σ_{E_1} and σ_{E_2} are the uncertainties in energy and σ_{t_1} and σ_{t_2} are the uncertainties in the sampling time.

When there is no time lag between the two different energy channels, the above relation reduces to:

$$\text{distance} = \frac{\left(\frac{z}{m}\right)^{1/2} (E_1 E_2)^{1/2}}{(E_1^{1/2} - E_2^{1/2})} [\sigma_{t_1}^2 + \sigma_{t_2}^2]^{1/2}$$

Using the above relationship, the distance from the source of modulation to the rocket, under the previously stated assumptions is approximately 4000 km for all of the pulsations. This figure is a factor of ten times smaller than those results reported by *Bryant et al.* [1967, 1975] and places the modulation near the auroral electron acceleration region in the magnetosphere.

3.11 Three Hertz Modulation

Figure 3.23 shows the particle flux versus time at the highest time resolution available for four energies in which pulsations were most clearly seen (67.5° pitch-angle). There appear to be high frequency structures in the high resolution data. Other directions showed a similar response but not as clearly. There are reports in the literature of a measured 3 Hz oscillation associated with the precipitation of electrons during pulsating aurora. Our data was investigated to determine if there were any coherent oscillations in the 1 – 10 Hz range. The ESA sampled at 20 Hz thereby limiting the highest frequency resolution to 10 Hz. Any lower frequency components are on the order of the length of at least some of the pulsations and so were not investigated. To quantify the variations, the power spectral content of the precipitating electrons was calculated.

Figure 3.24 shows the power spectral density estimates for four different energies for the 67° pitch-angle for the time period between 115 s and 200 s after launch. The 67° direction is chosen because this direction showed the largest signal to noise ratio. During this time interval two pulsations were observed,

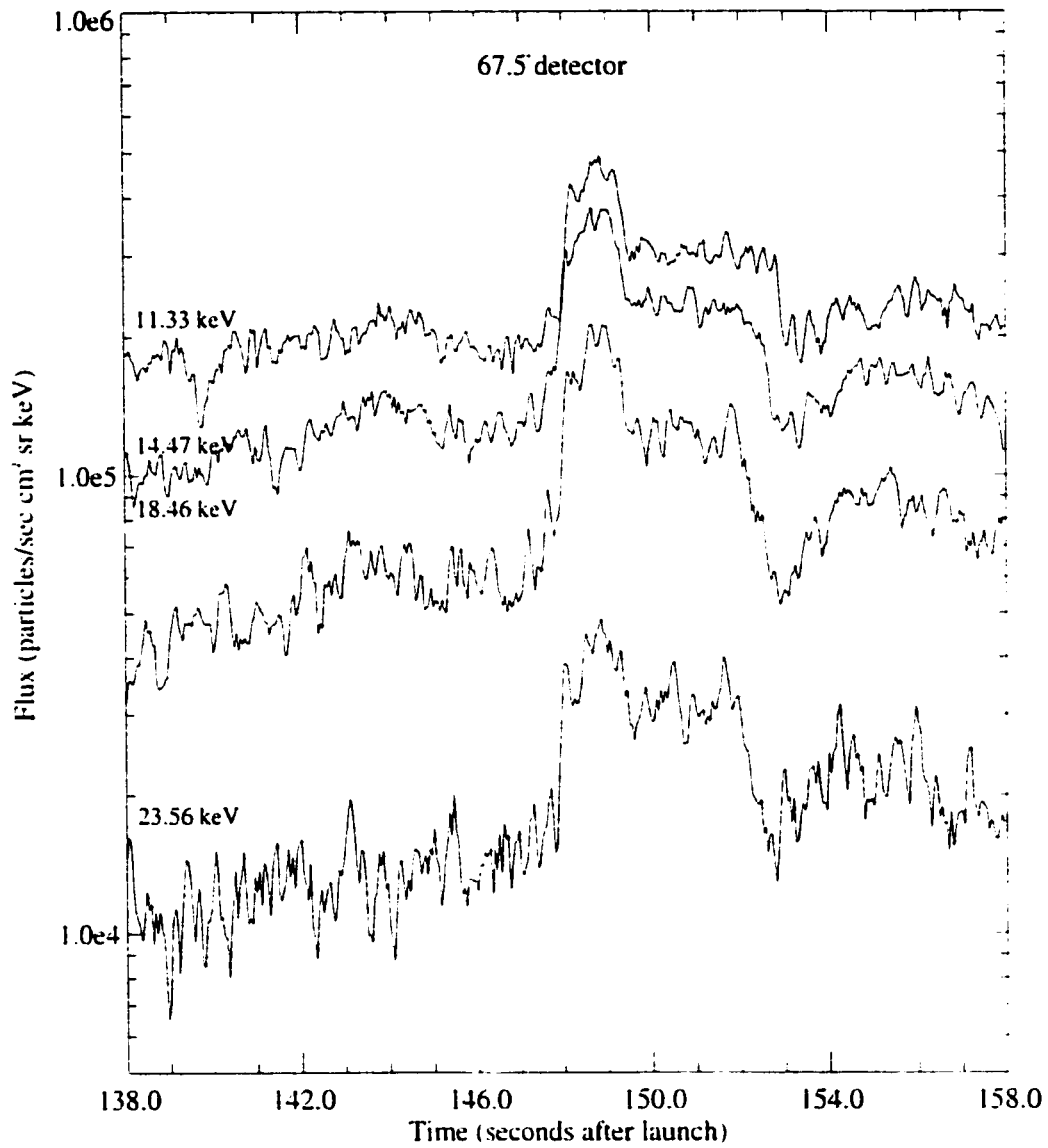


Figure 3.23: Plot of particle flux versus time with highest time resolution possible. Coherent wiggles on the order of three Hertz appear to be present in the data.

the first at 119 s and the second at 146 s. The data were summed in both energy and pitch-angle in order to improve counting statistics. This was very necessary since we wanted the highest time resolution possible. In order to calculate the power spectral density estimates the data were segmented into chunks, windowed with a Bartlett window (which is basically a triangle) and overlapped by one half of each data segment length. The overlapping reduced the number of degrees of freedom but allowed for better error estimates.

As can be seen there is no significant power in any frequencies during a pulsation event. There appears to be some power at frequencies centered around 1 Hz but this is an artifact of the rocket spin period which was approximately 0.8 Hz. None of the pulsations in any of the pitch-angles or energies showed any significant power and so we can say that there were no 3 Hz variations present in the pulsating auroral event we observed.

3.12 Summary of Observations

The data obtained by the electron instruments during the roughly 10 minute flight were complex and difficult to analyze. The signal-to-noise ratio was not very large and only by increasing the sample length could statistically meaningful data be obtained. Further complicating the analysis was the fact that multiple processes were occurring and separation of the different processes was difficult to do without further corroborating data. However, there are many observations which were made about the data.

Low Energy Electrons ($20 \text{ eV} < E < 1 \text{ keV}$)

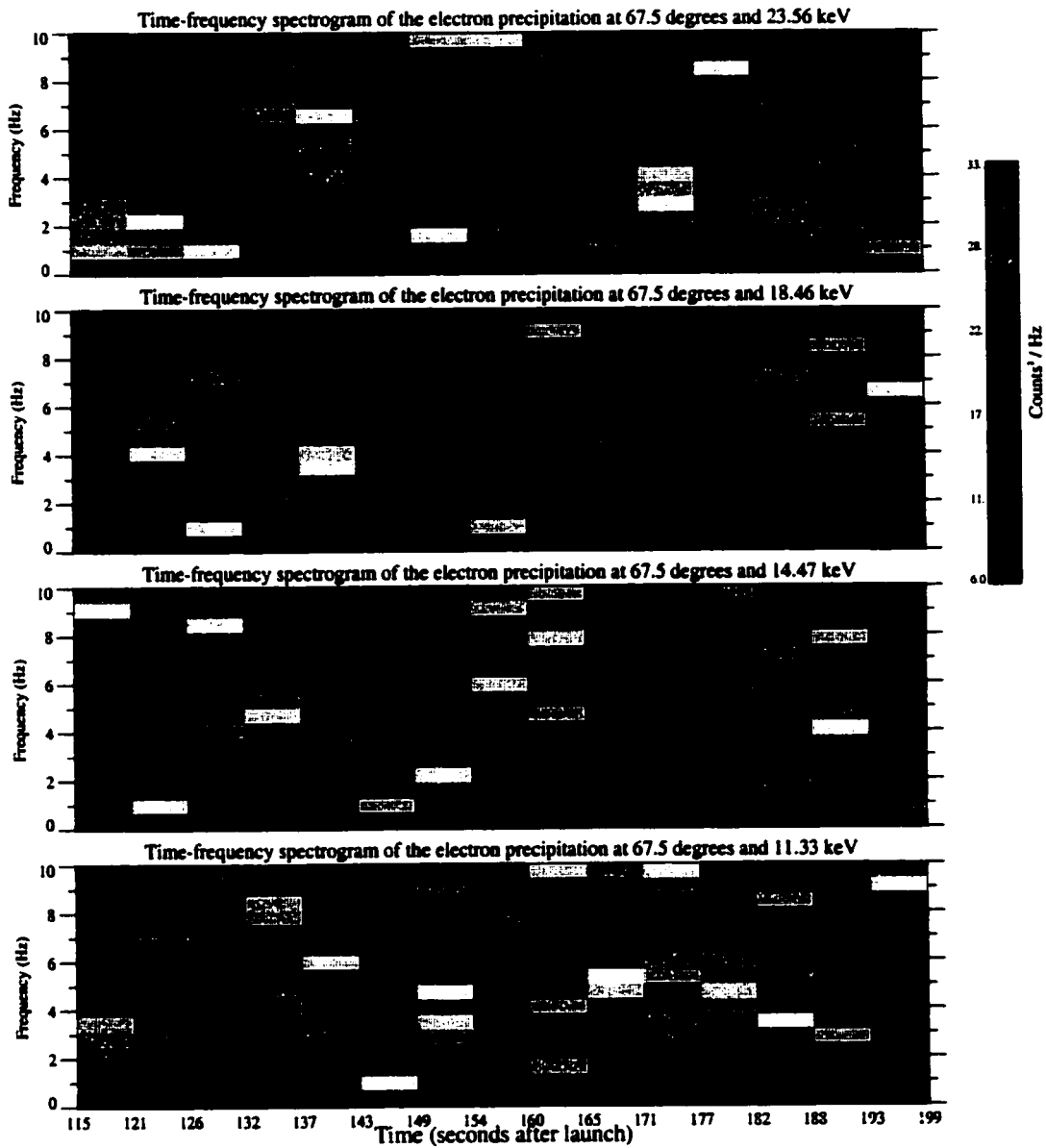


Figure 3.24: Power spectral density estimate for the time period of 115 s to 200 s after launch. The different panels correspond to different energy channels and all panels are from the 0° detectors. The power has units of counts² per Hz.

Low energy electrons show isotropic pitch-angle distributions and similar energy spectra for up and downgoing electrons. We deduced that the best explanation for these observations is to postulate the existence of a potential above the rocket, which reflects upgoing secondaries back to the rocket where they are detected as downgoing electrons.

Pulsations were observed at energies just above the potential energy. This implies the source is modulating and producing pulsations at all energies, from at least 1 keV to 60 keV. Previous observations indicated pulsations only occur at energies above a few keV [Johnstone, 1983].

Intermediate Energy Electrons ($1 \text{ keV} < E < 5 \text{ keV}$)

Intermediate energy electrons show a plateau in the energy spectra. This region shows little change in fluxes and except for small downgoing pitch-angles there are no pulsation structures. In the upward direction pulsations were observed and it was postulated that these pulsations are due to some ionospheric phenomena which is not at this time understood. Related to this observation is that all of the upgoing flux, regardless of time (pulsation or unstructured background) showed greater than expected flux..

High Energy Electrons ($E > 5 \text{ keV}$)

High energy electrons show a steep pitch-angle dependent spectrum. Pulsations are largest in these energies. Pitch-angle distributions are anisotropic for all energies. The flux of high energy electrons out of the ionosphere is greater than normally expected. Pitch-angle anisotropy decreases at pulsation onset and then increases toward pre-pulsation values. The largest change in flux is

in the range of 50° to 90° . This leads to the conclusion that the pitch-angle distribution did not become isotropic. The observations indicate that the region below the rocket was not passive. Energy spectra were fitted to Maxwellian distributions with resulting characteristic energies of ~ 5 keV for the pulsations and ~ 4 keV for the background, suggesting that the pulsation mechanism includes heating and modulation of electrons.

Velocity Dispersion

Velocity dispersion analysis shows no measurable time delay in the arrival of the electrons with different energies. This result indicates the source is located close to Earth, ~ 4000 km above the rocket. This result is different from previous observations that indicate the source is located on the equator.

3 Hz Oscillations

High time resolution data show structures with time scales of a few hundred milliseconds. However, power spectral analysis did not reveal any significant frequencies. These results are different from previous results that indicate the presence of a 3 Hz substructure.

Chapter 4

EVALUATION OF PULSATION MODELS AND REQUIREMENTS FOR A PHYSICALLY MEANINGFUL MODEL

The preceding chapter presented important features about the pulsating aurora. This chapter will discuss the important features of these observations to evaluate the various models which have previously been used to explain pulsation mechanisms. We will show that none of the existing models can account for all of the features in our data. We conclude with some suggestions for an alternative model.

4.1 Electron Cyclotron Wave-Particle Interactions

The three pulsating aurora models presented in Chapter 1 rely on the electron cyclotron wave-particle interaction to cause electrons to be rapidly moved into the loss cone. Once in the loss cone these electrons travel along the magnetic field into the ionosphere where they deposit their energy through collisions resulting in the changes in illumination that are called pulsations.

The electron cyclotron wave-particle interaction is most effective at the point in the magnetosphere where the ambient magnetic field is weakest, that is, in the equatorial region [Kennel and Petschek, 1966]. This is because the charac-

teristic energy an electron needs in order to be able to resonate with the waves increases rapidly as the electron moves away from the equator. If the resonance interaction is to proceed far from the equator then larger anisotropies are needed. Such large anisotropies are not usually seen and so it is thought that the electron cyclotron wave-particle interaction occurs mostly in the equatorial region of the magnetosphere.

The models of *Coroniti and Kennel* [1970] and *Davidson* [1979, 1986a, b, 1990] and *Trakhtengerts et al.* [1986]; *Demekhov and Trakhtengerts* [1994] rely on the results of *Bryant et al.* [1967, 1969, 1971, 1975] which used the observed velocity dispersion to locate the modulation region at the magnetic equator.

The model of *Davidson* [1979, 1986a, b, 1990] depends upon backscattered low energy electrons from the ionosphere to modulate the pitch-angle anisotropy, which in turn causes either wave growth or decay. If there is no way for low energy electrons to get to the interaction region, then the Davidson mechanism is not viable as a method for causing the pulsations. Our low energy electron observations have led to the inference of a parallel potential drop above the rocket that reflects low energy electrons back into the ionosphere. Thus, the Davidson model is inappropriate for use in explaining the pulsations we observed.

Likewise, there are observations [*Oguti et al.*, 1986] of pulsating aurora without hydromagnetic waves as would be required if the Coroniti/Kennel theory were responsible for the pulsations. During the rocket flight, no hydromagnetic waves were observed on the ground. Furthermore, none of the pulsations that were observed had a periodic nature, that is, there was no single length of time between pulsations as would be expected if they were caused by a global oscillation such as a hydromagnetic wave. While aperiodic magnetic pulsations are possible we will not discuss them since the *Coroniti and Kennel* [1970] model

was developed, in part, to explain the periodic nature of the observed pulsations. This lack of periodicity combined with the lack of velocity dispersion means that most probably the Coroniti/Kennel theory is also not appropriate for explaining our observations. There is one observation that favors the Coroniti/Kennel mechanism and that is the increase in characteristic energy of the energy spectra during a pulsation. Such an increase can be caused by a compression of the magnetic field which is expected in connection with this type of mechanism. However, while the rise in temperature may be due to a compression we will show below that the Coroniti/Kennel mechanism cannot explain the lack of velocity dispersion in our observations.

While no magnetic pulsations were observed and there is an inferred electric potential which would deny low energy electrons access to the equatorial region, it is still possible that the pulsations we observed were caused by electron cyclotron wave-particle resonance in the equatorial region. Even though comparison of our observations with the specifics of both the Davidson model and the Coroniti/Kennel model seem to rule out these mechanisms, the basic whistler mode resonance might still be a valid way to produce pulsations. Therefore, the cyclotron maser model of *Trakhtengerts et al.* [1986]; *Demekhov and Trakhtengerts* [1994] cannot be ruled out as long as it is possible for electrons to have come from the equator.

The arrival timing of the different energy electrons makes it improbable for the electrons to have left from the equator at the same time. It is still possible however, that the interaction region at the equator is large or that the electrons left the production region at different times or a combination of both of these circumstances. It will be argued, by using a reasonable estimate of the extent of the interaction region, that it is not possible to model our observations as emanating from a large region. Therefore, the most plausible explanation is

that the electrons left the equatorial region at different times. While this is possible in principle, such a physical arrangement is highly unlikely. This leads to the conclusion that the whistler mode electron interaction is not a candidate for explaining our observations.

Inan et al. [1982] showed that the region in which electron cyclotron wave-particle interactions can occur is spread out over a range of distances away from the magnetic equator. If there is a non-localized source mechanism then it is possible that different energies resonate with different wave frequencies in such a way that the electrons all arrive at the ionosphere (i.e. the rocket) at the same time. For instance, as the electron cyclotron wave passes through the equatorial region and travels toward the conjugate hemisphere, it will resonate with higher and higher energy electrons. These electrons will be farther away from the rocket but because of their higher energy, will need less time to travel to the rocket. So what needs to be shown is that no single source region, no matter how spread out, could result in the observations made by our instruments.

We define the largest possible region in which electrons may interact with whistler waves. To do so, we start with the dispersion relation for whistler mode waves traveling at a small angle θ with respect to the magnetic field [*Helliwell*, 1967; *Inan et al.*, 1978]. It can be written as:

$$n^2 = \frac{c^2 k^2}{\omega^2} = 1 + \frac{\omega_{pe}^2}{\omega(\omega_{ce} |\cos \theta| - \omega)}. \quad (4.1)$$

where n is the index of refraction, c is the speed of light in vacuum, k is the wave number, ω is the angular frequency, ω_{ce} is the electron cyclotron frequency and

$$\omega_{pe} = \left(\frac{4\pi N_e q_e^2}{m_e} \right)^{1/2}$$

is the electron plasma frequency. N_e is the electron number density, q_e is the charge of the electron and m_e is the electron mass. The electron cyclotron frequency is written as

$$\omega_{ce} = \frac{q_e B}{cm_e}$$

where B is the ambient magnetic field. The resonance condition for electrons to resonate with the whistler wave is given as

$$\omega - kv_{\parallel} \cos \theta = \omega_{ce}. \quad (4.2)$$

In order for resonance to occur the parallel velocity of the wave must match the Doppler shifted parallel velocity of the electron. The parallel resonant energy is given by (non-relativistic):

$$E_{\parallel} = \frac{1}{2} m_e v_{\parallel}^2.$$

Combining the resonance condition from Equation 4.2 with the parallel energy and assuming propagation along the magnetic field gives:

$$E_{\parallel} = \frac{m_e}{2} \left(\frac{\omega - \omega_{ce}}{k} \right)^2$$

We use the whistler mode dispersion relation from Equation 4.1 (Assume that $\omega \ll \omega_{ce} \ll \omega_{pe}$) to eliminate the wave number and obtain:

$$E_{\parallel} \cong \frac{m_e c^2}{2} \left(\frac{\omega}{\omega_{pe}} \right)^2 \left(\frac{\omega_{ce}}{\omega} - 1 \right)^3. \quad (4.3)$$

This equation gives the energy of the electron as an explicit function of the wave frequency and implicit functions of the magnetic field and the electron number density. Figure 4.1 shows how the resonant electron energy varies as a function of the frequency, where $f = 2\pi\omega$. Plotted are five different curves, each depending on a different number density for $L = 5.6$ (A dipole magnetic field at $L = 5.6$ is assumed, for which $|\vec{B}| = 310$ nT at the equator). Also plotted in the figure is a horizontal line showing the minimum energy in which pulsations were observed. (We are looking at the low energy electrons at the equator because, as is shown in Figure 4.2 below, as the wave travels away from the equator it will interact with higher and higher energy electrons.) The points on the line show what frequency range ($f = 2850 - 4400$ Hz) would be responsible for resonating with 1 keV electrons at the equator. We assume that some particular frequency ($f_{res} = f \pm \delta f$) within this range is responsible for causing the observed pulsations and that as that band limited wave travels along the field line it interacts with electrons of different energies causing them to precipitate.

Next, we choose a number density model. This enables us to determine to what latitude we can expect our frequency limited wave to interact with the highest energy electrons for which pulsations were observed (60 keV). Given our geomagnetic conditions, a typical number density observation [Chappell *et al.*, 1970] for the equator, at $L = 5.6$, is $N_e = 1/\text{cm}^3$.

Our purpose is to find the largest region in space over which we can confidently expect whistler mode waves to resonantly interact with electrons in the energy range over which pulsations were observed. After having chosen a frequency range which corresponds to the observed electron precipitation, we can assume a number density model in order to find how far away from the equator the resonance interaction can take place. A number density that varies as r^{-1} is found to be generally representative of the number density variations [Angerami and

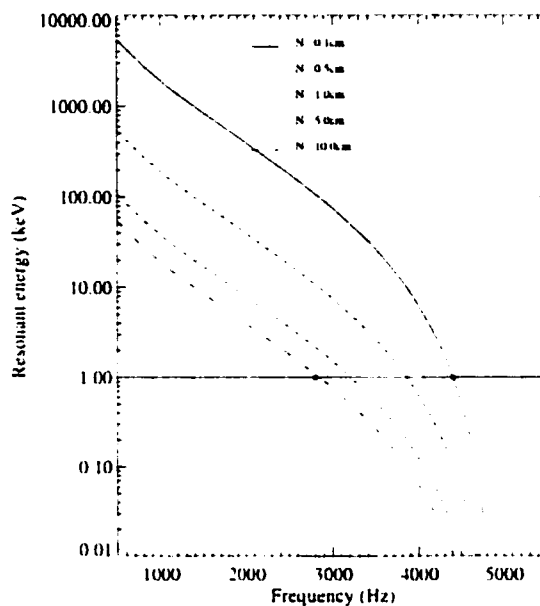


Figure 4.1: Resonant energy for the whistler mode wave as a function of frequency. Different number densities representing different equatorial conditions show how the resonant energy as a function of frequency can vary. The horizontal line represents the lowest energy in which we can be certain that pulsations were observed. The magnitude of the magnetic field is $|\vec{B}| = 310 \text{ nT}$.

Carpenter, 1966] measured in this part of the magnetosphere.

Having chosen a number density model, Figure 4.2 shows a plot of the resonant energy as a function of frequency for various latitudes. Shown on the plot is the maximum energy for which pulsations were observed. Also shown on the plot is the frequency range determined from Figure 4.1 for which the low energy electrons were resonant. For latitudes much higher than 24° , it is not possible for the whistler wave to resonate with the 60 keV electrons given the frequency range which we have chosen. Therefore, we will restrict our interaction region to be 24° off the equator in either direction. Assuming the interaction region is within 24° of latitude from the equator, we find the length along the field line

Table 4.1: Table of the number density and the resulting maximum latitudes given the initial frequency range obtained from the 1 keV electrons.

	$n \text{ (cm}^{-3}\text{)}$	latitude (degrees)
1	0.1	15°
2	0.5	20°
3	1.0	24°
4	5.0	–
5	10.0	–

within this region (from 0° to 24° $\sim 1.28 \times 10^4$ km).

Table 4.1 shows results of the same procedure carried out above for different number densities at the equator. The table shows that a number density of 1 per cc gives the largest possible interaction region. Densities which are higher than 1 per cc do not allow whistler mode resonance with the 60 keV electrons within the possible frequency range that can resonate with the 1 keV electrons. Densities which are lower than 1 per cc indicate that for the same frequency range a smaller region is necessary.

This interaction region gives the largest possible distance over which the whistler wave may interact with the electrons that were observed. The choice of the frequency range, which led to the latitude range was made with the purpose of finding the largest interaction region allowed, given our starting assumptions. It is likely that if this mechanism were active, the actual interaction region would be smaller.

Having now estimated the length of the possible interaction region, we ask the

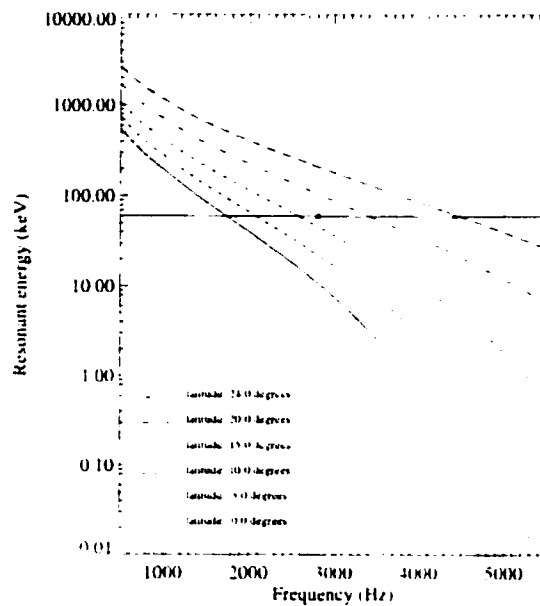


Figure 4.2: Resonant energy for the whistler mode wave as a function of frequency. Different latitudes are plotted to demonstrate how the resonance energy changes with distance from the equator. The number density goes as r^{-4} and the magnetic field is assumed to be dipolar. The horizontal line represents the highest energy in which pulsations were observed.

question of whether or not that interaction region could produce the electron arrival times we observed.

We start a whistler wave at the equator and allow it to interact with the lowest energy electrons we observed, i.e. 1 keV electrons. As it travels toward the furthest end of the region, it interacts with higher and higher energy electrons. We ask if it is possible that a 1 keV electron which left the equator at time t_0 can arrive at the rocket at the same time as a 60 keV electron which interacted with the same whistler wave at time t_1 at latitude $\lambda = -24^\circ$, where the difference between t_0 and t_1 is the wave travel time between these two points and is approximately 0.2 s. The time needed to travel from the equator to the rocket,

a distance of $\sim 4.3 \times 10^4$ km, for the 1 keV electron, is 2.3 seconds. The time needed to travel from latitude $\lambda = -24^\circ$, a distance of ~ 53000 km (4.3×10^4 km + 1.28×10^4 km), for the 60 keV electron is 0.4 s. This means that even given an extended source region, it is not possible for electrons to leave the equatorial region of the magnetosphere and arrive at the rocket at the same time.

The only possibility left for electrons to have interacted in the equatorial region is if they left the region (either extended or small) at different times. We argue that such an occurrence is extremely unlikely. In order for this to happen, a large number of improbable steps must occur in sequence. Firstly, whistler waves of a certain frequency will interact with an electron of a certain energy. In order for the electrons to have left the equatorial region at different times to get to the rocket at the same time, then different frequency waves have to be active at different times and only for the duration of the pulsation. No wave that is very close in frequency can be excited or else electrons will arrive at different times. The scenario would then be something like this: A whistler wave with a narrowly defined frequency spectrum resonates with certain energy electrons. The low energy electrons must go first, long before the high energy electrons. A specific while later, a different narrowly defined frequency spectrum from a whistler wave must resonate with higher energy electrons and send them onto the ionosphere. This process continues until all electrons between 1 keV and 60 keV have been in resonant contact with their respective whistler waves.

We observed nine pulsations and none of them showed evidence of velocity dispersion. The nine different observations occurred at different times (over 200 s of separation in time) over the ranges of L-shell $L = 5.6 - 6.5$. The likelihood of all of those electrons arriving at the rocket in the way they did, given the scenario as just described, is highly improbable and will not be considered further.

The whistler mode wave-particle interaction has been examined in great detail. This was necessary because so many others [*Coroniti and Kennel, 1970; Davidson, 1990; Demekhov and Trakhtengerts, 1994*] have discussed this process. We believe we have demonstrated that whistler mode waves in the equatorial region are not candidates for causing the pulsations we observed. If whistler mode waves are not a viable candidate for causing the pulsations, then another wave mode must be searched for. The next section discusses another candidate model.

4.2 DC Electric Field

Since the ion cyclotron model is unlikely to have produced our observations, another model is investigated. A possible mechanism for producing the pulsations is the parallel electric field which was inferred from the low energy electron data. If this parallel electric field was somehow modulated, its effect on the electrons might be to cause some electrons to be moved into the loss cone, where they precipitate as pulsation events. Specifically, an increase in the field strength would result in electrons being moved in phase space so that they will precipitate.

In order to see if the electric field could be responsible, we need to see how the field changes in time. Since the electric field was inferred and not measured, we investigate how the slope of the low energy spectra changed with time. We assume the slope of the low energy is tied to the parallel electric field, and that changes in the slope of the spectra are tied to changes in the parallel field. For instance, if the parallel electric field suddenly vanished, we would expect the low energy slope of the upgoing electrons to be different from the low energy slope of the downgoing electrons. The reason behind this statement is that the

downgoing electrons would have a source that was not necessarily the same as the upgoing electrons. We expect that reflection off either ionosphere results in similar upgoing spectra [Evans and Moore, 1979] but in going from one hemisphere to the other it is very difficult to believe [Evans and Moore, 1979] that the electrons pass adiabatically through the equatorial region. Passage through the equatorial region would result in some change to the low energy spectra. While the example of a vanishing parallel electric field is a little extreme we still expect that changes in the parallel electric field will show up as changes in the slope of the low energy electron spectra. Specifically, if the field changes in magnitude (larger/smaller) we would expect up and downgoing electrons to have similarity over either a (greater/lesser) energy range.

The low energy electrons ($E < 1$ keV) were very well modeled as a power law spectra. The fits to the data were made with a non-linear least squares fit using a gradient-expansion algorithm. Figure 4.3 shows the fitted power law parameter as a function of time for the 6° and 174° detectors. We choose these directions because the 174° shows what the flux looks like leaving the atmosphere and the 6° shows what it looks like coming back down. These two directions should be most sensitive to changes in the electric field. The values range from -1.2 to -1.35. There is no change in the power law parameters that is correlated to a pulsation event. Nor is there a change in how many energy channels are described by the power law fits. Therefore, we conclude that a slowly modulated parallel electric field is not likely to be responsible for causing the pulsations.

4.3 What a Model Must Incorporate

Our observations do not fit in with other pulsation reports. The first of these is the lack of pulsations in the 1 – 5 keV range for electrons between 22° and

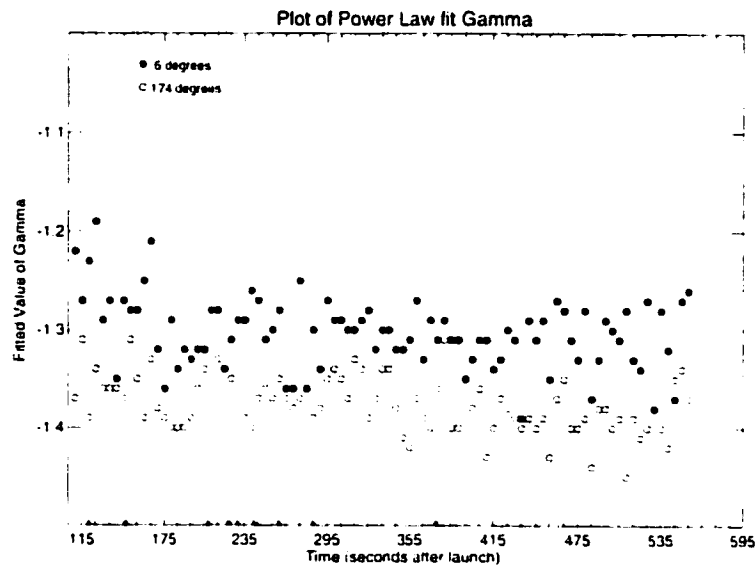


Figure 4.3: Plot of the low energy fitted power law parameter as a function of time for the pitch-angles of 6° and 174° . Pulsation events are indicated by the upward pointing arrows. There is no relation between the change in the power law and the presence of a pulsation event.

90° . Another important new result is that we see electron modulation down to at least 1 keV and possibly lower. A third observation is the anomalous pitch-angle distributions, we measured at high electron energies ($E > 5$ keV).

In the following discussion, we will address the observations and the physical mechanisms that might cause them separately, always keeping in mind that in order to fully understand the pulsations of that night, a synthesis of all the different mechanisms must be made.

4.3.1 *No Pulsation Observations for Energies between 1 and 5 keV*

We first address the lack of pulsations in the 1 – 5 keV range for electrons between 22° and 90° . It is physically difficult for a single step process to modu-

late electrons over a broad range of energies and pitch angles while somewhere in the middle of these ranges no modulation occurs. Instead, this observation suggests that a multi-step process is most likely to be involved.

In order to make sense of these processes, we must first separate out the low energy ($E < 1$ keV) pulsations in the non field-aligned directions. We have concluded that these are caused by the parallel potential drop which was inferred from the energy spectral measurements. Since this potential does not appear to be associated with the pulsation mechanism (see the discussion in Chapter 3 and in the proceeding section), we disregard these low energy electron observations when trying to explain the pulsation mechanism. We are however left with the pulsations in the low energy field aligned electrons and the high energy electrons that were observed at all pitch-angles.

We now focus on a couple of possible mechanisms. One is that the pulsation mechanism is a purely field aligned process which operates over all the observed energies. After the pulsations have been produced, they spread out or diffuse in pitch-angle space. From Chapter 3 we learned that pulsations occur down to roughly 1 keV and that these low energy pulsations are field aligned. This spread in pitch-angle is therefore energy dependent since there are no pulsations in the higher pitch-angles for the 1 – 5 keV electrons. Therefore, one model possibility is to describe a mechanism which produces only field aligned pulsations and then another mechanism which diffuses them in pitch-angle but not for energies below about 5 keV.

A second possible mechanism we consider is that there is a process which produces pulsations at all pitch-angles over the energy range of 5 – 60 keV. These electrons then excite some other mechanism which produces electrons of low energy ($E < 5$ keV) in only the field aligned direction. This second mechanism

might be similar to the one which produces supra-thermal electrons [*Johnstone and Winningham, 1982*].

The observations of *Lepine et al. [1980]*; *Smith et al. [1980]*; *Sandahl et al. [1980]*; *McEwen et al. [1981]*, in which pulsations have a low energy cutoff, point toward the second mechanism as the more likely one to investigate. Given the range of energies over which pulsations are seen, it seems difficult to find a single wave mode with a broad enough frequency spectrum to be able to resonate with all of the observed electron energies. However, if a secondary mechanism, which acted primarily in the field aligned direction and on electrons with energies below 5 keV, could be excited then the observations would be explained. One of the constraints on this secondary mechanism is that it would have to act rapidly, or close to the Earth, since the arrival of the low energy electrons occurred within 1 second of the higher energy electrons.

4.3.2 *Anomalous Pitch-angle Distributions*

The observations of the flux of high energy electrons out of the ionosphere are now addressed. There are only a few observations which have seen similar results [*McDiarmid et al., 1961*; *Cummings et al., 1966*]. In both cases, observations of anomalous pitch-angle distributions (i.e. greater than expected flux of electrons out of the ionosphere) were discussed, but no quantitatively satisfactory conclusions have been drawn [*Cummings et al., 1966*].

One point to note is that we see the high upward flux regardless of whether or not a pulsation occurred. This points toward the idea that whatever is causing this large flux of upward moving high energy electrons is unrelated to the pulsation mechanism itself. However, other observations have shown that the ionosphere does play a role in the production of pulsating aurora [*Stenbaek-*

Nielsen, 1980].

There is another phenomena that may be related to these observations. That is, the observation of enhanced layers in auroras [*Stenbaek-Nielsen and Hallinan, 1979; Hallinan et al., 1985, 1997*]. *Stenbaek-Nielsen and Hallinan* [1979] focused on pulsating auroral observations while *Hallinan et al.* [1985, 1997] included discrete auroral observations as well. These observations show that auroral luminosity can occur in extremely thin (< 3 km) layers. Typically electrons which impinge on the atmosphere deposit their energy over a range of altitudes. This means that some electrons are able to travel farther into the atmosphere than others before interacting with ionospheric species and producing light. The distance over which electrons deposit their energy is itself energy dependent with lower energy electrons depositing over longer distances [*Rees, 1989*]. Given that there is a distribution of electrons entering the atmosphere one would typically expect the luminosity to extend over long vertical distances of at least one scale height [*Stenbaek-Nielsen and Hallinan, 1979; Shepherd and Falthammar, 1980*], which for heights of 100 km and for these electrons is roughly 12 km.

The observations made by the all-sky cameras during the PARX launch showed that the luminosity of the pulsating patches extended over vertical distances of ~ 1 km (private communication, Liz MacDonald and Tom Hallinan). Thus, we were in a situation which had previously been observed but never before in conjunction with a rocket experiment. *Shepherd and Falthammar* [1980] discuss two possible mechanisms which could cause the thin layers of illumination. Both depend upon the existence of electric fields. The first is a dc electric field of magnitude ~ 7 V/m. The next is an ac field, which, because of its varying intensity and phase would necessarily have to be much larger to accomplish the same results. *Shepherd and Falthammar* [1980] suggest that the rms value of

the ac field should be at least a factor of 10 larger than the dc field.

The rocket experiment had on board both dc and ac electric field antennas. These instruments worked during the entire flight and did not record any fields that were near to 7 V/m, much less a factor of 10 or higher. However, when the rocket passed through the height of the illumination ($z \approx 100$ km) the pulsating patches were to the north of the rocket, that is, the rocket did not measure the region in which the pulsations occurred. When the rocket was over the pulsation region on magnetic field lines which mapped down to the patches the distance between the rocket and illumination region was at least 100 km and up to 300 km. Thus, if one postulated an instability which had a interaction volume strictly confined to say the area and vertical extent of a pulsating patch, one might not have been able to measure either the dc or ac electric fields associated with it.

Thus, there are two separate observations, the anomalous pitch-angle distributions and the thin vertical extent of the illumination which seem to be connected and which obviously are important aspects of the pulsating auroral event. While we do not have an explanation for these observations, it has been speculated that the thin vertical extent may be produced by a turbulent electromagnetic field which is located within a small region of space and which is capable of producing fields which are strong enough to both stop the precipitating electrons within a ~ 1 km distance (private communication with Tom Hallinan).

Finally, we need to connect all of the varying requirements together. This task is not possible given the measurements we have. We would need to have had measurements in both the region in which the pulsations were produced and also in the region below the rocket where the illumination was observed. Since

the pulsations were observed over such a broad range of energies it is most likely that a global process needs to be considered.

Chapter 5

SUMMARY AND CONCLUSIONS

5.1 Results

We designed and built a rocket experiment which measured the electron precipitation associated with a pulsating auroral event. This was the first experiment that measured backscattered electrons. Our low energy electron observations led to the inference of an electric potential which accelerated electrons toward the ionosphere and which caused upgoing backscattered electrons to be reflected. Thus, we conclude that, at least for this event, backscattered electrons play no role in causing the pulsations.

One result of this experiment is that pulsations were seen in energies down to 100's of eV's. This is the first time that such observations have been made. Any new theory must take into account the fact that, at least for some pulsation events, low energy electrons are modulated. All-sky camera images indicated the pulsations exhibited a streaming effect. It is believed that this is the first time a rocket was ever launched into a pulsating event in which such streaming occurred. Very little or no velocity dispersion was observed. A simple interpretation is that the source is close to the Earth. This feature is different from other observations that showed dispersion. Our observations show a region of energy - pitch-angle space in which pulsations are not observed. This space includes electrons with energies less than ~ 5 keV for pitch-angles between 22°

and 90° . The greatest change between pulsation and background occurred for electrons between 10 and 20 keV and for pitch-angles around 50° . Finally, we observed larger than expected fluxes of high energy electrons ($E > 10$ keV) out of the ionosphere.

In the course of investigation into possible causes for explaining the pulsations we observed, detailed comparisons with data led us to disregard the currently accepted theories of *Coroniti and Kennel* [1970], *Davidson* [1986a] and *Trakhtengerts et al.* [1986]; *Demekhov and Trakhtengerts* [1994]. We also considered models that involved ion cyclotron electron resonance interaction and time varying dc electric field. Again, these models were not able to explain the data to any great extent. We have thus made progress in narrowing down the mechanisms which may be responsible. A rough synthesis model relying on our results has been constructed and presented.

5.2 Further Research

This rocket experiment has raised several important questions about auroral pulsations. Of the questions that are not answered, the most important about the pulsation mechanism itself concerns the low energy cutoff (~ 5 keV) for pulsations with pitch-angles between 22° and 90° and the new observation that pulsations are seen in energies down to roughly 1 keV.

Questions about the flux of high energy electrons out of the ionosphere are also important. We do not know if the high energy electron fluxes out of the ionosphere are always present during pulsating auroral events. Future experiments should extend our observations by including high energy electron measurements in both up and down directions. Such measurements will yield

information on the high energy limit of upward fluxes.

Another important question is whether the result of no velocity dispersion is unique to our observations. This feature needs to be verified since it implies where the source is located and also about the mechanisms of pulsations.

One way to address some of these questions is to design a rocket experiment which had two separate rockets, one with a apogee at altitudes just over 100 km and one which flew up to 400 km. This way electron and electric and magnetic field measurements could be taken both above the illumination region and in the illumination region itself.

Other experiments that might be worthwhile to consider would be to have observations at the conjugate field point from which a rocket was launched. The results from such an experiment might help to decide if the pulsations were produced in the equatorial region. Having satellite coverage on the same magnetic field line would go a long way to answering questions about whether the pulsation mechanism is operating in the equatorial region of the magnetosphere.

BIBLIOGRAPHY

Angerami, J. J., and D. L. Carpenter, Whistler studies of the plasmopause in the magnetosphere 2. electron density and total tube electron content near the knee in magnetospheric ionization, *JGR*, 71, 711 – 725, 1966.

Bryant, D. A., H. L. Collin, G. M. Courtier, and A. D. Johnstone, Evidence for velocity dispersion in auroral electrons, *Nature*, 215, 45 – 46, 1967.

Bryant, D. A., G. M. Courtier, and A. D. Johnstone, Modulation of auroral electrons at large distances from the earth, *J. Geomag. Geoelectr.*, 31, 579 – 592, 1969.

Bryant, D. A., G. M. Courtier, and B. Bennett, Equatorial modulation of electrons in a pulsating aurora, *J. Geomag. Geoelectr.*, 33, 859 – 867, 1971.

Bryant, D. A., M. J. Smith, and G. M. Courtier, Distant modulation of electron intensity during the expansion phase of an auroral substorm, *Planet. Space Sci.*, 23, 867 – 878, 1975.

Carlson, C. W., and J. P. McFadden, Design and application of imaging plasma instruments, in *Measurement Techniques in Space Plasmas: Particles*, vol. 102, pp. 125 – 140, American Geophysical Union, 1998.

Chappell, C. R., K. K. Harris, and G. W. Sharp, A study of the influence of magnetic activity on the location of the plasmopause as measured by ogo 5, *JGR*, 75, 50 – 56, 1970.

- Chisham, G., D. Orr, M. J. Taylor, and H. Luhr, The magnetic and optical signature of a pg pulsation, *PSS*, 38, 1443 – 1456, 1990.
- Coroniti, F. V., and C. F. Kennel, Electron precipitation pulsations, *J. Geophys. Res.*, 75, 1279 – 1289, 1970.
- Cresswell, G. R., Fast auroral waves, *Planet. Space Sci.*, 16, 1453 – 1464, 1968.
- Cummings, W. D., R. E. LaQuey, and B. J. O'Brien, Rocket-borne measurements of particle fluxes and auroral light, *JGR*, 71, 1399 – 1407, 1966.
- Davidson, G. T., Self-modulated vlf waves-electron interactions in the magnetosphere: A cause of auroral pulsations, *J. Geophys. Res.*, 84, 6517 – 6523, 1979.
- Davidson, G. T., Pitch angle diffusion in morningside aurorae 1. the role of the loss cone in the formation of impulsive bursts of precipitation, *J. Geophys. Res.*, 91, 4413 – 4427, 1986a.
- Davidson, G. T., Pitch angle diffusion in morningside aurorae 2. the formation of repetitive auroral pulsations, *JGR*, 91, 4429 – 4436, 1986b.
- Davidson, G. T., Pitch-angle diffusion and the origin of temporal and spatial structures in morningside aurorae, *Space. Sci. Rev.*, 53, 45 – 82, 1990.
- Davidson, G. T., and Y. T. Chiu, A closed nonlinear model of wave-particle interactions in the outer trapping and morningside auroral regions, *JGR*, 91, 13,705 – 13,710. 1986.
- Demekhov, A. G., and V. Y. Trakhtengerts, A mechanism of formation of pulsating aurorae., *JGR*, 99, 5831 – 5841, 1994.
- Evans, D. S., Precipitating electron fluxes formed by a magnetic field aligned potential difference, *J. Geophys. Res.*, 79, 2853 – 22,858, 1974.

Evans, D. S., and T. E. Moore, Precipitation electrons associated with the diffuse aurora: Evidence for electrons of atmospheric origin in the plasma sheet, *J. Geophys. Res.*, *84*, 6451 – 6457, 1979.

Evans, D. S., G. T. Davidson, H. D. Voss, W. L. Imhof, J. Mobilia, and Y. T. Chiu, Interpretation of electron spectra in morningside pulsating aurorae, *J. Geophys. Res.*, *92*, 12,295 – 12,306, 1987.

Frauenfelder, H., *Subatomic Physics*, Prentice-Hall, 1974.

Gradshteyn, I. S., and I. M. Ryzhik, *Table of Integrals, Series and Products*, Academic Press, 1965.

Hallinan, T. J., H. C. Stenbaek-Nielsen, and C. S. Deehr, Enhanced aurora, *J. Geophys. Res.*, *90*, 8461 – 8475, 1985.

Hallinan, T. J., J. Kimball, H. C. Stenbaek-Nielsen, and C. S. Deehr, Spectroscopic evidence for suprathermal electrons in enhanced auroras, *JGR*, *102*, 7501 – 7508, 1997.

Helliwell, R. A., A theory of discrete vlf emissions from the magnetosphere, *J. Geophys. Res.*, *72*, 4773 – 4790, 1967.

Hillebrand, O., J. Münch, and R. L. McPherron, Ground – satellite correlative study of a giant pulsation event, *JG*, *51*, 129 – 140, 1982.

Inan, U. S., T. F. Bell, and R. A. Helliwell, Nonlinear pitch angle scattering of energetic electrons by coherent vlf waves in the magnetosphere, *J. Geophys. Res.*, *83*, 3235 – 3253, 1978.

Inan, U. S., T. F. Bell, and H. C. Chang, Particle precipitation induced by short-duration vlf waves in the magnetosphere, *J. Geophys. Res.*, *87*, 6243 – 6264, 1982.

- Johnstone, A. D., Correlation between electron and proton fluxes in post-breakup aurora, *J. Geophys. Res.*, **76**, 5259 – 5267, 1971.
- Johnstone, A. D., Pulsating aurora, *Nature*, **274**, 119 – 126, 1978.
- Johnstone, A. D., The mechanism of pulsating aurora, *Annales Geophysicae*, **1**, 397 – 410, 1983.
- Johnstone, A. D., and J. D. Winningham, Satellite observations of suprathermal electron bursts, *JGR*, **87**, 2321 – 2329, 1982.
- Kennel, C. F., and H. I. Petschek, Limit on stably trapped particle fluxes, *J. Geophys. Res.*, **71**, 1 – 28, 1966.
- Knoll, G. F., *Radiation Detection and Measurement*, John Wiley and Sons, 1989.
- Krall, N. A., and A. W. Trivelpiece, *Principles of Plasma Physics*, San Francisco Press, Inc., San Francisco, California, 1986.
- Lepine, D. R., D. A. Bryant, and D. S. Hall, A 2.2 hz modulation of auroral electrons imposed at the geomagnetic equator, *NAT*, **286**, 469 – 471, 1980.
- Lummerzheim, D., and J. Liliensten, Electron transport and energy degradation in the ionosphere: evaluation of the numerical solution, comparison with laboratory experiments and auroral observations, *AG*, **12**, 1039 – 1051, 1994.
- Lummerzheim, D., M. H. Rees, and H. R. Anderson, Angular dependent transport of auroral electrons in the upper atmosphere, *PSS*, **37**, 109 – 129, 1989.
- McDiarmid, I. B., D. C. Rose, and E. E. Budzinski, Direct measurement of charged particles associated with auroral-zone radio absorption, *CJP*, **39**, 1888 – 1900, 1961.

McEwen, D. J., E. Yee, B. A. Whalen, and A. W. Yau, Electron energy measurements in pulsating aurora, *Can. J. Phys.*, *59*, 1106 – 1115, 1981.

McPherron, R. L., G. K. Parks, F. V. Coroniti, and S. H. Ward, Studies of the magnetospheric substorm, 2, correlated magnetic micropulsation and electron precipitation occurring during auroral substorms, *J. Geophys. Res.*, *73*, 1697 – 1713, 1968.

Nemzek, R., R. Nakamura, D. N. Baker, R. D. Belian, D. J. McComas, M. F. Thomsen, and T. Yamamoto, The relationship between pulsating auroras observed from the ground and energetic electrons and plasma density measured at geosynchronous orbit, *J. Geophys. Res.*, *100*, 23,935 – 23,944, 1995.

Oguti, T., K. Hayashi, T. Yamamoto, J. Ishida, T. Higuchi, and N. Nishitani, Absence of hydromagnetic waves in the magnetospheric equatorial region conjugate with pulsating auroras, *J. Geophys. Res.*, *91*, 13,711 – 13,715, 1986.

Orear, J., A. H. Rosenfeld, and R. A. Schluter, *Nuclear physics; a course given by Enrico Fermi at the University of Chicago.*, University of Chicago Press, 1949.

Parks, G. K., *Physics of Space Plasmas*, Addison-Wesley Publishing Company, New York, 1991.

Prasad, S. S., D. J. Strickland, and Y. T. Chiu, Auroral electron interaction with the atmosphere in the presence of conjugate field-aligned electrostatic potentials, *J. Geophys. Res.*, *88*, 4123 – 4130, 1983.

Rees, M. H., *Physics and Chemistry of the Upper Atmosphere*, Cambridge University Press, Cambridge, 1989.

- Røyvrik, O., Instabilities in pitch angle diffusion and their possible relation to a 3 hz modulation in pulsating aurora, *J. Geomag. Geoelectr.*, **40**, 1309 – 1321, 1978.
- Røyvrik, O., and T. N. Davis, Pulsating aurora: Local and global morphology, *J. Geophys. Res.*, **82**, 4720 – 4740, 1977.
- Saito, Y., S. Machida, M. Hirahara, T. Mukai, and H. Miyaoka, Rocket observation of electron fluxes over a pulsating aurora, *Planet. Space Sci.*, **40**, 1043 – 1054, 1992.
- Sandahl, I., Pitch angle scattering and particle precipitation in a pulsating aurora - an experimental study, Ph.D. thesis, Kiruna Geophysical Institute, Kiruna, Sweden, 1984.
- Sandahl, I., L. Eliasson, and R. Lundin, Rocket observations of precipitating electrons over a pulsating aurora, *Geophys. Res. Lett.*, **7**, 309 – 312, 1980.
- Shepherd, G. G., and C. G. Falthammar, Implications of extreme thinness of pulsating auroral structures, *J. Geophys. Res.*, **85**, 217 – 218, 1980.
- Smith, M. J., D. A. Bryant, and T. Edwards, Pulsations in auroral electrons and positive ions, *J. Geomag. Geoelectr.*, **42**, 167 – 178, 1980.
- Steel, R. G. D., and J. H. Torrie, *Principles and Procedures of Statistics*, McGraw-Hill Book Company, 1960.
- Stenbaek-Nielsen, H. C., Pulsating aurora: The importance of the ionosphere, *Geophys. Res. Lett.*, **7**, 353 – 356, 1980.
- Stenbaek-Nielsen, H. C., and T. J. Hallinan, Pulsating auroras: Evidence for noncollisional thermalization of precipitating electrons, *J. Geophys. Res.*, **84**, 3257 – 3271, 1979.

Taylor, M. J., G. Chisham, and D. Orr, Pulsating auroral forms and their association with geomagnetic giant pulsations, *PSS*, 37, 1477, 1989.

Trakhtengerts, V. Y., V. R. Tagirov, and S. A. Chernous, A circulating cyclotron maser and pulsed vlf emissions, *Geomagnetism and Aeronomy*, 26, 77 – 82, 1986.

Whalen, B. A., J. R. Miller, and I. B. McDiarmid, Energetic particle measurements in a pulsating aurora, *J. Geophys. Res.*, 76, 978 – 986, 1971.

Yau, A. W., B. A. Whalen, and D. J. McEwen, Rocket-borne measurements of particle pulsation in pulsating auroras, *J. Geophys. Res.*, 86, 5673 – 5681, 1981.

Appendix A

SOLID STATE TELESCOPE GEOMETRIC FACTOR

This appendix contains a derivation of the geometric factor for the solid state telescopes. The description of the variables and how they are related is given in Figure A.1 where a schematic of the solid state telescopes is given.

The geometric factor relates the counts coming from a source of particles to the counts actually measured by the detector. The geometric factor is solely a function of the mechanical arrangement of shielding and the surface area of the actual detector. This arrangement can be as simple to describe as a detector that accepts information from all directions and all energies or as complicated to describe as a retarding potential electrostatic analyzer. The solid state telescopes used on the rocket launch of March 13, 1997 fall somewhere in the middle and an analytic description is possible, although complicated. For the solid state telescopes the units of the geometric factor are given in $\text{cm}^2 \text{ster}$.

To find an expression for the geometric factor we allow particles to interact with the detector from all possible angles over the entire surface of the detector. An added complication is that the detector is shielded by a series of baffles. These baffles cut down on the ability of the detector to see particles so that we can have a more accurate idea of where a particle actually came from when it hit the detector. In order to get the total number of counts we sum over all of the area of the detector for all angles of incidence. This results in an integration

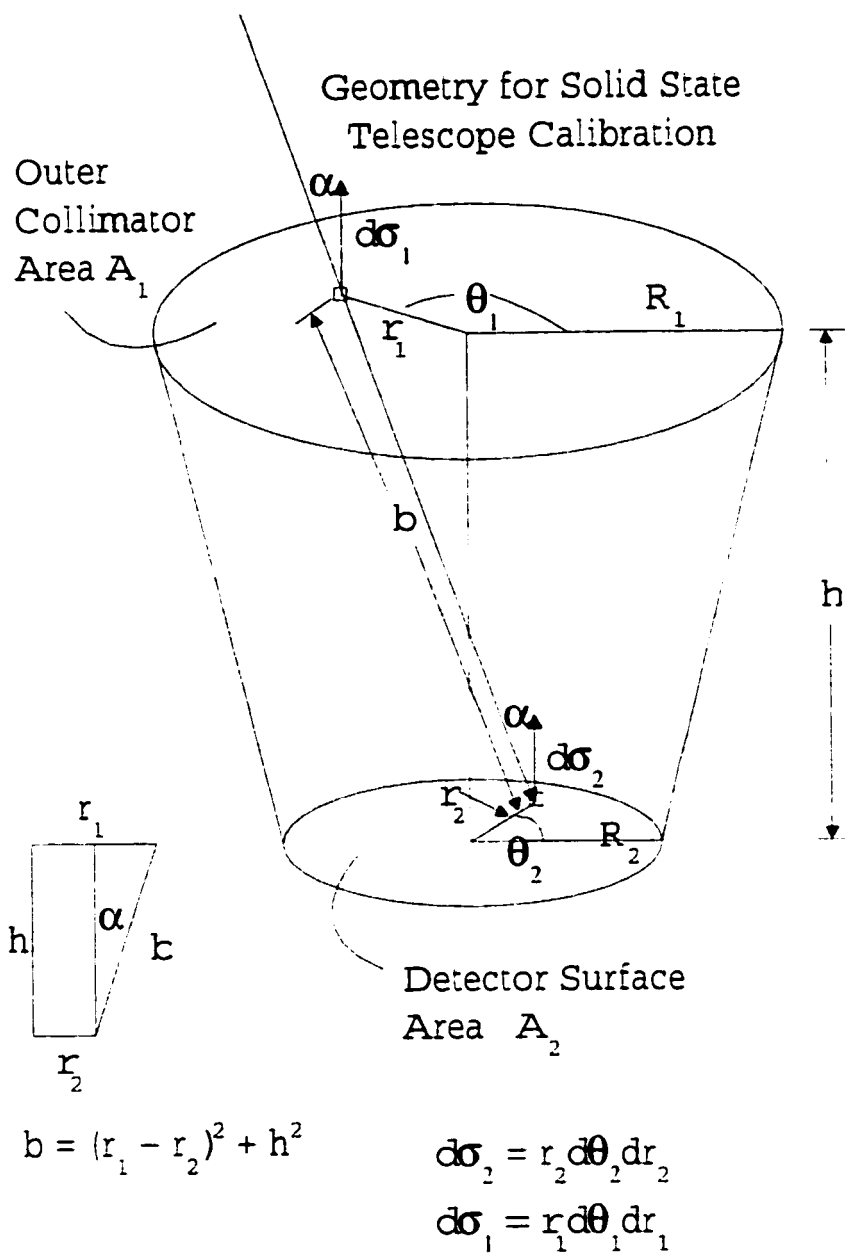


Figure A.1: Geometry of solid state telescope field of view. This is used to set up the integral that will determine the geometric factor.

over 4 variables which describe all of the solid angles and surface areas.

Since this is a complicated integral I will be making a lot of substitutions. Also the form of the integrals after the substitutions is still complicated enough that I resorted to using a table of integrals by *Gradshteyn and Ryzhik* [1965]. I will reference these integrals by page number.

From the drawing we can see that the geometric factor is defined as:

$$G = \int_0^{2\pi} \int_0^{2\pi} \int_0^{R_2} \int_0^{R_1} \frac{r_1 dr_1 r_2 dr_2 d\theta_1 d\theta_2 \cos^2 \phi}{b^2} \quad (\text{A.1})$$

where the variable R_1 is the radius variable of the outer collimator and θ_1 is the azimuthal variable of the outer collimator. Further, R_2 is the radius variable of the actual detector and θ_2 is the azimuthal variable of the detector. Also h is the distance between the outer collimator and the detector surface and b is the distance from a single point on the outer collimator to a single point on detector's surface. This distance is written as:

$$b = r_1^2 + r_2^2 + h^2 - 2r_1 r_2 \cos(\theta_1 - \theta_2)$$

Finally $\cos^2 \phi$ relates the direction of the particle to the normal of the detector and is written as:

$$\cos^2 \phi = \frac{h^2}{b^2}$$

With all these substitutions we rewrite Eq. A.1 as:

$$G = h^2 \int_0^{2\pi} \int_0^{2\pi} \int_0^{R_2} \int_0^{R_1} \frac{r_1 dr_1 r_2 dr_2 d\theta_1 d\theta_2}{[r_1^2 + r_2^2 + h^2 - 2r_1 r_2 \cos(\theta_1 - \theta_2)]^2}$$

Now I am going to integrate a single variable at a time. The first variable will be one of the angle variables. It does not matter which one so I will start with the integration over θ_1 .

We make the following substitutions:

$$\begin{aligned} \alpha &= r_1^2 + r_2^2 + h^2 & x &= \theta_1 - \theta_2 \\ \beta &= 2r_1 r_2 & dx &= d\theta_1 \end{aligned}$$

This changes the limits of integration to:

$$\begin{aligned} \theta_1 = 0 & & x &= -\theta_2. \\ \theta_1 = 2\pi & & x &= 2\pi - \theta_2. \end{aligned}$$

This gives

$$G = h^2 \int_0^{R_2} \int_0^{R_1} \int_0^{2\pi} \int_{-\theta_2}^{2\pi - \theta_2} \frac{r_1 dr_1 r_2 dr_2 d\theta_2 dx}{(\alpha - \beta \cos(x))^2}. \quad (\text{A.2})$$

This integral can be done as a contour integral but can also be found in Gradshteyn and Ryzhik on page 425. The result is in the form of Legendre polynomials and is written as:

$$G = h^2 \int_0^{R_2} \int_0^{R_1} \int_0^{2\pi} r_1 dr_1 r_2 dr_2 d\theta_2 \frac{2\pi}{(\alpha^2 - \beta^2)} P_1 \left(\frac{\alpha}{(\alpha^2 - \beta^2)^{1/2}} \right).$$

From above neither α or β depend on θ_2 and so we can do the integration over the detector surface area and we are left with only the radial variables over which to integrate. Also the Legendre polynomial of order 1 is its argument. This gives

$$G = 4\pi^2 h^2 \int_0^{R_2} \int_0^{R_1} r_1 dr_1 r_2 dr_2 \frac{h^2 + r_1^2 + r_2^2}{\left[(h^2 + r_1^2 + r_2^2)^2 - (2r_1 r_2)^2 \right]^{3/2}} \quad (\text{A.3})$$

We make the following substitutions:

$$p = h^2 + r_1^2 + r_2^2 \quad dp = 2r_1 dr_1 \quad r_1^2 = p - h^2 - r_2^2.$$

The new limits become:

$$\begin{aligned} r_1 = 0 & \quad p = h^2 + r_2^2 \\ r_1 = R_1 & \quad p = h^2 + R_1^2 + r_2^2. \end{aligned}$$

This gives:

$$G = 4\pi^2 h^2 \int_0^{R_2} \int_{h^2+r_2^2}^{h^2+R_1^2+r_2^2} r_2 dr_2 \frac{dp}{2} \frac{p}{(p^2 - 4r_1^2 r_2^2)^{3/2}} \quad (\text{A.4})$$

To further simplify we write :

$$4r_1^2 r_2^2 = 4r_2^2(p - h^2 - r_2^2) = 4r_2^2 p - 4r_2^2(h^2 + r_2^2).$$

Using this in Equation A.4 gives:

$$G = 2\pi^2 h^2 \int_0^{R_2} \int_{h^2+r_1^2}^{h^2+R_1^2+r_2^2} r_2 dr_2 \frac{p dp}{(p^2 - 4r_2^2 p + 4r_2^2(h^2 + r_2^2))^{3/2}}. \quad (\text{A.5})$$

Let

$$\delta = 4r_2^2(h^2 + r_2^2)$$

$$\epsilon = -4r_2^2$$

$$\Upsilon = \delta + \epsilon p + p^2$$

$$q = 4\delta - \epsilon^2.$$

Using these substitutions in Equation A.5 gives:

$$G = 2\pi^2 h^2 \int_0^{R_2} \int_{h^2+r_1^2}^{h^2+R_1^2+r_2^2} r_2 dr_2 \frac{p dp}{\Upsilon^{3/2}}. \quad (\text{A.6})$$

This integral can be found in Gradshteyn and Ryzhik on page 101, and has the following solution:

$$G = 2\pi^2 h^2 \int_0^{R_2} r_2 dr_2 \left. \frac{-2(2\delta + \epsilon p)}{q \Upsilon^{1/2}} \right|_{h^2+r_1^2}^{h^2+r_2^2+R_1^2}.$$

Rearranging gives:

$$G = 4\pi^2 h^2 \int_0^{R_2} \frac{r_2 dr_2}{q} \left(\frac{(2\delta + \epsilon p)}{\Upsilon^{1/2}} \Big|_{h^2+r_2^2} - \frac{(2\delta + \epsilon p)}{\Upsilon^{1/2}} \Big|_{h^2+r_2^2+R_1^2} \right) \quad (\text{A.7})$$

We write $q = 16r_2^2 h^2$ and with a lot of messy algebra we rewrite

$$\frac{(2\delta + \epsilon p)}{\Upsilon^{1/2}} \Big|_{h^2+r_2^2} = 4r_2^2$$

$$\frac{(2\delta + \epsilon p)}{\Upsilon^{1/2}} \Big|_{h^2+r_2^2+R_1^2} = \frac{4r_2^2(h^2 + r_2^2 - R_1^2)}{((h^2 + r_2^2 - R_1^2)^2 + 4h^2 R_1^2)^{1/2}}.$$

Using these results in equation A.7 gives:

$$G = 4\pi^2 h^2 \int_0^{R_2} \frac{r_2 dr_2}{16r_2^2 h^2} \left[4r_2^2 - \frac{4r_2^2(h^2 + r_2^2 - R_1^2)}{((h^2 + r_2^2 - R_1^2)^2 + 4h^2 R_1^2)^{1/2}} \right].$$

Pulling constants outside the integral and rearranging results in:

$$G = \pi^2 \int_0^{R_2} r_2 dr_2 \left[1 - \frac{(h^2 + r_2^2 - R_1^2)}{((h^2 + r_2^2 - R_1^2)^2 + 4h^2 R_1^2)^{1/2}} \right].$$

The first term inside the integral is easily integrated and gives:

$$G = \frac{\pi^2 R_2}{2} - \pi^2 \int_0^{R_2} \frac{r_2 dr_2 (h^2 + r_2^2 - R_1^2)}{((h^2 + r_2^2 - R_1^2)^2 + 4h^2 R_1^2)^{1/2}}.$$

We make the following substitutions:

$$\begin{aligned}\eta &= 4h^2 R_1^2 \\ s &= h^2 + r_2^2 - R_1^2 \\ ds &= 2r_2 dr_2.\end{aligned}$$

This changes the limits of integration to:

$$\begin{aligned}r_2 = 0 & \quad s = h^2 - R_1^2 \\ r_2 = R_2 & \quad s = h^2 + R_2^2 - R_1^2.\end{aligned}$$

Using these substitutions gives the integral the form:

$$G = \frac{\pi^2 R_2}{2} - \frac{\pi^2}{2} \int_{h^2 - R_1^2}^{h^2 + R_2^2 - R_1^2} \frac{s ds}{(s^2 + \eta)^{1/2}}$$

Let $u = (\eta + s^2)^{1/2}$. This gives

$$G = \frac{\pi^2 R_2}{2} - \frac{\pi^2}{2} \int_{h^2 - R_1^2}^{h^2 + R_2^2 - R_1^2} \frac{s ds}{u^{2n+1}} \quad (\text{A.8})$$

This integral is found on page 105 of Gradshteyn and Ryzhik and in our case for $n = 0$ we write :

$$G = \frac{\pi^2 R_2}{2} - \frac{\pi^2}{2} \left(\frac{1}{u^{-1}} \Big|_{h^2 - R_1^2}^{h^2 + R_2^2 - R_1^2} \right).$$

This gives:

$$G = \frac{\pi^2 R_2}{2} + \frac{\pi^2}{2} \left(u|_{h^2 - R_1^2} - u|_{h^2 + R_2^2 - R_1^2} \right).$$

Substituting for u , s and η gives:

$$G = \frac{\pi^2 R_2}{2} + \frac{\pi^2}{2} \left[(4h^2 R_1^2 + (h^2 - R_1^2)^2)^{1/2} - (4h^2 R_1^2 + (h^2 + R_2^2 - R_1^2)^2)^{1/2} \right]. \quad (\text{A.9})$$

We rewrite

$$4h^2 R_1^2 + (h^2 - R_1^2)^2 = (h^2 + R_1^2)^2$$

and putting this into equation A.9 and simplifying the last term gives:

$$G = \frac{\pi^2}{2} \left[R_2^2 + h^2 + R_1^2 - (h^2 + R_2^2 + R_1^2 + 2h^2 R_2^2 + 2h^2 R_1^2 - 2R_1^2 R_2^2)^{1/2} \right]. \quad (\text{A.10})$$

We simplify this result with the following substitution:

$$h^2 + R_2^2 + R_1^2 + 2h^2 R_2^2 + 2h^2 R_1^2 - 2R_1^2 R_2^2 = (h^2 + R_1^2 + R_2^2)^2 - 4R_1^2 R_2^2$$

We finally end up with the following form for the geometric factor for the solid state telescopes:

$$G = \frac{\pi^2}{2} \left[R_2^2 + h^2 + R_1^2 - \left[(h^2 + R_2^2 + R_1^2)^2 - 4R_1^2 R_2^2 \right]^{1/2} \right]. \quad (\text{A.11})$$

This gives the geometric factor as a function of only the distance between the detector surface and the collimator, h , the radius of the outer collimator, R_1 , and the radius of the detector's surface area, R_2 .

Appendix B

PARTICLE FLUX, DISTRIBUTION FUNCTIONS AND MOMENTS

This appendix discusses the relationship between particle counts, particle flux and the distribution function. We also derive the moments of the distribution function used for the analysis of the data. This work is in no way original but I have included it so that others may profit by my effort. Also I have had a difficult time finding the information that I have put here in one single place. Discussions with Dr. Michael McCarthy, Dr. George Parks and Dr. Juan Roederer have contributed to the information provided here. The book Physics of Space Plasmas by *Parks* [1991] has an introductory explanation of the material here as well.

Instruments that measure electrons or charged particles in space are basically counting devices. It is necessary to turn these counts into physically meaningful quantities by connecting the number of counts an instrument records to the population from which the counted particles came. The measurement of counts is a statistical task. We do not count every particle in some region of space, this would be much too difficult and would return a great deal more information than is actually needed or wanted. Aside from confusion there is little to be gained from knowing the trajectories and momenta of every particle in a particular population. What is of more interest and use is knowing the gross overall properties of the population, such as how many particles there are, or

how they are distributed in momentum space.

Determination of the Relationship Between the Distribution Function and the Particle Flux

We will show how one goes from counts to the distribution function. This is the step that connects theory to experiment. We start by defining the number of counts, δN counted by some measuring device. This quantity δN is determined by a number of factors. δN depends on the collecting area of the detector, the length of time the detector collects counts, the energy range over which counts are detected and finally the solid angle through which particles are allowed to strike the detector. We write this as:

$$\delta N = j(E, \alpha, \phi) \delta A_{\perp} \delta t \delta E \delta \Omega, \quad (\text{B.1})$$

where $\delta \Omega$ is the solid angle, δE is the energy range, δt is the sample time, δA_{\perp} is the surface area of the detector and finally $j(E, \alpha, \phi)$ is differential particle flux, often simply called the flux. Notice that $j(E, \alpha, \phi)$ acts as a constant of proportionality that allows the number of counts to be equated to the physical constraints imposed by a detector.

Now we compare this δN to the number of counts in some sample taken from a population of particles, that is, taken from the distribution function.

$$\delta N = f(E, \alpha, \phi) \delta \vec{r} \delta \vec{v} = f(E, \alpha, \phi) \delta t v \delta A_{\perp} \delta v_1 \delta v_2 \delta v_3, \quad (\text{B.2})$$

where $\delta \vec{r}$ is a volume differential over coordinate space, and $\delta \vec{v}$ is a volume differential over velocity space. We convert the coordinate space integral into

$\delta t v \delta A_{\perp}$ where δt is the time interval, v is the velocity of the particles, and δA_{\perp} is the perpendicular area the particles take up in coordinate space. The velocity space differential is split up into three Cartesian coordinates x , y and z .

We now convert the Cartesian velocities to spherical coordinates. We write:

$$\begin{aligned} d^3v &= v^2 dv \sin \alpha d\alpha d\phi, \\ v &= \left(\frac{2E}{m}\right)^{1/2}, \\ dv &= \frac{1}{m} \left(\frac{m}{2E}\right)^{1/2} dE. \end{aligned}$$

Using the definitions for v and dv and the definition $d\Omega = \sin \alpha d\alpha d\phi$ we can write:

$$d^3v = \frac{1}{m} \left(\frac{2E}{m}\right)^{1/2} dE d\Omega.$$

Using the above relations for the velocity space differential and the velocity in Equation B.2 we have:

$$\delta N = f(E, \alpha, \phi) \delta t \left(\frac{2E}{m}\right)^{1/2} \delta A_{\perp} \frac{1}{m} \left(\frac{2E}{m}\right)^{1/2} dE d\Omega. \quad (\text{B.3})$$

Now since we are talking about the same number of counts we can equate Equations B.1 and B.3 to obtain the following relationship:

$$j(E, \alpha, \phi) \delta A_{\perp} \delta t \delta E \delta \Omega = f(E, \alpha, \phi) \delta t \left(\frac{2E}{m}\right)^{1/2} \delta A_{\perp} \frac{1}{m} \left(\frac{2E}{m}\right)^{1/2} dE d\Omega.$$

Simplifying gives the flux in terms of the distribution function or the distribution function in terms of the flux:

$$j(E, \alpha, \phi) = \frac{2E}{m^2} f(E, \alpha, \phi) \quad (\text{B.4})$$

$$f(E, \alpha, \phi) = \frac{m^2}{2E} j(E, \alpha, \phi). \quad (\text{B.5})$$

There is one other necessary task and that is to convert distribution functions from one variable to another. This is often done so that one can talk about distribution functions that were measured by different detectors. So one can ask how the distribution function $f(\vec{v})$ compares to the distribution function $f(E, \alpha, \phi)$. The only way this can be done is through the Jacobian of an integral. Since both of the distribution functions must have measured the same number of particles from phase space they must be equivalent, but we must make sure that the phase space differentials are of the same size, this is where the Jacobian comes in.

As a simple case we compare the number density measured in two different detectors, one that measures the energy and pitch-angle of the particle and another that measures the perpendicular and parallel velocity components of the particles. We have:

$$n = \int f(v_{\perp}, v_{\parallel}, \phi) d^3v = \int f(E, \alpha, \phi) d^3v. \quad (\text{B.6})$$

Rather than do a formal Jacobian analysis, we just compare the differentials of the two different distribution functions. For these simple geometries this is easier to do than use the formal Jacobian.

The distribution function $f(v_{\perp}, v_{\parallel}, \phi)$ is in the form of a polar coordinate, so we write:

$$d^3v = v_{\perp} dv_{\perp} dv_{\parallel} d\phi.$$

The distribution function $f(E, \alpha, \phi)$ is in the form of spherical coordinates, so we write:

$$d^3v = \frac{1}{m} \left(\frac{2E}{m} \right)^{1/2} dE d\Omega.$$

These two velocity elements must be equal so we have:

$$v_{\perp} dv_{\perp} dv_{\parallel} d\phi = \frac{1}{m} \left(\frac{2E}{m} \right)^{1/2} dE d\Omega.$$

Substituting $v_{\perp} = \left(\frac{2E}{m} \right)^{1/2} \sin \alpha$ in the above equation gives:

$$dv_{\perp} dv_{\parallel} d\phi = \frac{1}{m} dE d\alpha d\phi.$$

Using this relation in Equation B.6 we have:

$$\int f(v_{\perp}, v_{\parallel}, \phi) \left(\frac{2E}{m} \right)^{1/2} \sin \alpha \frac{1}{m} dE d\alpha d\phi = \int f(E, \alpha, \phi) \frac{1}{m} \left(\frac{2E}{m} \right)^{1/2} dE \sin \alpha d\alpha d\phi.$$

Since the differential volume elements are the same we can put both quantities under the same integral:

$$\int [f(v_{\perp}, v_{\parallel}, \phi) - f(E, \alpha, \phi)] \frac{1}{m} \left(\frac{2E}{m} \right)^{1/2} dE \sin \alpha d\alpha d\phi = 0.$$

Since this integral is equal to zero then the argument inside must also be equal to zero. This gives as a final result:

$$f(v_{\perp}, v_{\parallel}, \phi) = f(E, \alpha, \phi). \quad (\text{B.7})$$

The same procedure must be followed whenever a comparing two different distribution functions. Now we can go on to find the moments of the distribution functions that we have measured.

Derivation of the Zeroth Moment of the Distribution

We start with the equation that determines the number density of the distribution function. The integration is over all velocity space. The final result will have units of number per meter³.

$$\langle n \rangle = \int f(\vec{v}) d\vec{v} \quad (\text{B.8})$$

where n is the number density, $f(\vec{v})$ is the velocity space distribution function and $d\vec{v}$ is the three dimensional differential over all of velocity space.

We write:

$$f(\vec{v}) = f(v_{\parallel}, v_{\perp}, \phi) = f(E, \alpha, \phi),$$

$$d\vec{v} = d^3v = \frac{1}{m} \left(\frac{2E}{m} \right)^{1/2} dE \sin \alpha d\alpha d\phi.$$

where E is the energy of the particle and m is the mass of the particle, α is the angle between the particle's trajectory and the ambient magnetic field and ϕ is the azimuthal angle. Using these in Equation B.8 we write:

$$\langle n \rangle = \int f(E, \alpha, \phi) \frac{1}{m} \left(\frac{2E}{m} \right)^{1/2} dE \sin \alpha d\alpha d\phi$$

Now we write the distribution function as:

$$f(E, \alpha, \phi) = \frac{m^2}{2E_k^2} \frac{C_{jk}}{g_j \Delta t}.$$

where C_{jk} is the counts, g_j is the geometric factor and Δt is the time sample length. The change from the continuum to discrete indices is an approximation because we do not sample over every single energy or every possible pitch-angle, however, this approximation is allowed because the difference is considered to be small. The letter k is an index over the different energy channels and j is an index over the different pitch-angles. Using this in the previous

relation, gives:

$$\langle n \rangle = \int \frac{m^2}{2E_k^2} \frac{C_{jk}}{g_j \Delta t} \frac{1}{m} \left(\frac{2E}{m} \right)^{1/2} dE \sin \alpha d\alpha d\phi$$

Rearranging and setting the integration limits on the two angle variables gives:

$$\langle n \rangle = \frac{(2m)^{1/2}}{2\Delta t} \int_{\phi - \frac{\Delta\phi}{2}}^{\phi + \frac{\Delta\phi}{2}} d\phi \int \frac{C_{jk}}{g_j} \frac{dE_k}{E_k^{3/2}} \int_{\alpha_j - \frac{\Delta\alpha}{2}}^{\alpha_j + \frac{\Delta\alpha}{2}} \sin \alpha d\alpha.$$

Doing the ϕ and α integration gives:

$$\langle n \rangle = \frac{(2m)^{1/2} \Delta\phi}{\Delta t} \int \frac{C_{jk}}{g_j} \frac{dE_k}{E_k^{3/2}} \sin(\alpha_j) \sin\left(\frac{\Delta\alpha}{2}\right).$$

We now change the final integration into a sum over the energy and pitch-angle. This gives:

$$\langle n \rangle = \frac{(2m)^{1/2} \Delta\phi \sin\left(\frac{\Delta\alpha}{2}\right)}{\Delta t} \sum_{jk} \frac{C_{jk}}{g_j} \frac{dE_k}{E_k^{3/2}} \sin(\alpha_j). \quad (\text{B.9})$$

Derivation of the Velocity Moment of the Distribution

The next moment to be determined is the velocity moment. This is defined as:

$$\langle \vec{v} \rangle = \frac{1}{n} \int \vec{v} f(\vec{v}) d\vec{v}. \quad (\text{B.10})$$

Once again we write

$$f(\vec{v}) = f(v_{\parallel}, v_{\perp}, \phi) = f(E, \alpha, \phi),$$

$$d\vec{v} = d^3v = \frac{1}{m} \left(\frac{2E}{m} \right)^{1/2} dE \sin \alpha d\alpha d\phi.$$

Using this in Equation B.10 we obtain:

$$\langle \vec{v} \rangle = \frac{1}{n} \int \vec{v} f(E, \alpha, \phi) \frac{1}{m} \left(\frac{2E}{m} \right)^{1/2} dE \sin \alpha d\alpha d\phi$$

We write the velocity vector in terms of its Cartesian coordinates. These are:

$$v_1 = v_x = \left(\frac{2E}{m}\right)^{1/2} \sin \alpha \cos \phi \quad (\text{B.11})$$

$$v_2 = v_y = \left(\frac{2E}{m}\right)^{1/2} \sin \alpha \sin \phi \quad (\text{B.12})$$

$$v_3 = v_z = \left(\frac{2E}{m}\right)^{1/2} \cos \alpha. \quad (\text{B.13})$$

We rewrite the velocity moment in terms of its components and obtain:

$$\langle v_1 \rangle = \frac{1}{n} \int \left(\frac{2E}{m}\right)^{1/2} \sin \alpha \cos \phi f(E, \alpha, \phi) \frac{1}{m} \left(\frac{2E}{m}\right)^{1/2} dE \sin \alpha d\alpha d\phi$$

$$\langle v_2 \rangle = \frac{1}{n} \int \left(\frac{2E}{m}\right)^{1/2} \sin \alpha \sin \phi f(E, \alpha, \phi) \frac{1}{m} \left(\frac{2E}{m}\right)^{1/2} dE \sin \alpha d\alpha d\phi$$

$$\langle v_3 \rangle = \frac{1}{n} \int \left(\frac{2E}{m}\right)^{1/2} \cos \alpha f(E, \alpha, \phi) \frac{1}{m} \left(\frac{2E}{m}\right)^{1/2} dE \sin \alpha d\alpha d\phi$$

Making all simplifications and substituting the particle flux for the distribution function we obtain:

$$\langle v_1 \rangle = \frac{1}{n\Delta t} \int \frac{C_{jk}}{g_j} \frac{dE_k}{E_k} \sin^2 \alpha d\alpha \cos \phi d\phi \quad (\text{B.14})$$

$$\langle v_2 \rangle = \frac{1}{n\Delta t} \int \frac{C_{jk}}{g_j} \frac{dE_k}{E_k} \sin^2 \alpha d\alpha \sin \phi d\phi \quad (\text{B.15})$$

$$\langle v_3 \rangle = \frac{1}{n\Delta t} \int \frac{C_{jk}}{g_j} \frac{dE_k}{E_k} \sin \alpha \cos \alpha d\alpha d\phi \quad (\text{B.16})$$

Next we take care of the angular integrations for Equations B.14 through B.16.

From Equation B.14 the ϕ integration is:

$$\int_{\phi - \frac{\Delta\phi}{2}}^{\phi + \frac{\Delta\phi}{2}} \cos \phi d\phi = 2 \cos \phi \sin \left(\frac{\Delta\phi}{2}\right).$$

The α integration from Equations B.14 and B.15 gives:

$$\int_{\alpha_j - \frac{\Delta\alpha}{2}}^{\alpha_j + \frac{\Delta\alpha}{2}} \sin^2 \alpha d\alpha = \frac{1}{2} [\Delta\alpha - \cos(2\alpha_j) \sin(\Delta\alpha)]. \quad (\text{B.17})$$

The ϕ integration from Equation B.15 is:

$$\int_{\phi - \frac{\Delta\phi}{2}}^{\phi + \frac{\Delta\phi}{2}} \sin \phi d\phi = 2 \sin \phi \sin \left(\frac{\Delta\phi}{2} \right).$$

The ϕ integration from Equation B.16 gives:

$$\int_{\phi - \frac{\Delta\phi}{2}}^{\phi + \frac{\Delta\phi}{2}} d\phi = \Delta\phi.$$

Finally the α integration from Equation B.16 gives:

$$\int_{\alpha_j - \frac{\Delta\alpha}{2}}^{\alpha_j + \frac{\Delta\alpha}{2}} \cos \alpha \sin \alpha d\alpha = \frac{1}{2} \sin(2\alpha_j) \sin(\Delta\alpha).$$

We rewrite Equations B.14 through B.16 using the above relations. At the same time we change the integrations over the counts into summations. This gives:

$$\langle v_1 \rangle = \frac{\sin \left(\frac{\Delta\phi}{2} \right) \cos \phi}{n\Delta t} \sum_{jk} \frac{C_{jk}}{g_j} \frac{dE_k}{E_k} [\Delta\alpha - \cos(2\alpha_j) \sin(\Delta\alpha)] \quad (\text{B.18})$$

$$\langle v_2 \rangle = \frac{\sin \left(\frac{\Delta\phi}{2} \right) \sin \phi}{n\Delta t} \sum_{jk} \frac{C_{jk}}{g_j} \frac{dE_k}{E_k} [\Delta\alpha - \cos(2\alpha_j) \sin(\Delta\alpha)] \quad (\text{B.19})$$

$$\langle v_3 \rangle = \frac{\Delta\phi}{2n\Delta t} \sum_{jk} \frac{C_{jk}}{g_j} \frac{dE_k}{E_k} \sin(2\alpha_j) \sin(\Delta\alpha). \quad (\text{B.20})$$

There are two more velocity moments that are of interest. Since the magnetic field organizes the distribution function we would like to look at the velocity moment that is perpendicular to the magnetic field and the moment that is parallel to the field. Equation B.20 actually gives the parallel velocity moment but the perpendicular moment needs to be calculated separately. As before we start with:

$$\langle v_{\perp} \rangle = \frac{1}{n} \int v_{\perp} f(\vec{v}) d\vec{v}. \quad (\text{B.21})$$

Once again we write

$$f(\vec{v}) = f(v_{\parallel}, v_{\perp}, \phi) = f(E, \alpha, \phi),$$

$$d\vec{v} = d^3v = \frac{1}{m} \left(\frac{2E}{m} \right)^{1/2} dE \sin \alpha d\alpha d\phi,$$

$$v_{\perp} = \left(\frac{2E}{m} \right)^{1/2} \sin \alpha.$$

Using this in Equation B.21 and substituting the flux for the distribution function we obtain:

$$\langle v_{\perp} \rangle = \frac{1}{n} \int \left(\frac{2E}{m} \right)^{1/2} \sin \alpha \frac{m^2}{2E_k^2} \frac{C_{jk}}{g_j \Delta t} \frac{1}{m} \left(\frac{2E}{m} \right)^{1/2} dE \sin \alpha d\alpha d\phi$$

Simplifying and integrating over the azimuthal variable gives:

$$\langle v_{\perp} \rangle = \frac{\Delta \phi}{n \Delta t} \int \frac{C_{jk}}{g_j} \frac{dE_k}{E_k} \sin^2 \alpha d\alpha$$

From Equation B.17 we take the value of the α integration and convert from an integral to a summation and obtain:

$$\langle v_{\perp} \rangle = \frac{\Delta \phi}{2n \Delta t} \sum_{jk} \frac{C_{jk}}{g_j} \frac{dE_k}{E_k} [\Delta \alpha - \cos(2\alpha_j) \sin(\Delta \alpha)]. \quad (\text{B.22})$$

Derivation of the Total Pressure Moment of the Distribution

The next highest moment of the distribution function gives information about the energy and the pressure. From this moment the temperature can be calculated as well. Since temperature is generally defined for a system in equilibrium its value does not have the same meaning for the situation we encounter

during pulsating aurora. However, we can still calculate the temperature and use it as a measure of the distribution function.

As we get to higher and higher order moments we go from scalar to vector to tensor quantities. The second order moment is a tensor quantity with nine components, thus, the derivation is more complicated. The derivation of the pressure tensor is done in many places [Parks, 1991; Krall and Trivelpiece, 1986] but the basic idea is to find the kinetic pressure of a population and subtract from that quantity the bulk motion of the population.

So we start with the following relation:

$$\langle P \rangle = m \int \vec{v} \vec{v} f(\vec{v}) d\vec{v} - mn \vec{V} \vec{V} = \overline{\overline{K}} - \overline{\overline{D}}. \quad (\text{B.23})$$

where P stands for the total pressure, $\overline{\overline{K}} = \vec{v}_i \vec{v}_j$ is the kinetic energy tensor, $\overline{\overline{D}}$ is the bulk velocity tensor and $\vec{V} \vec{V}$ is the bulk velocity dyadic. A dyadic is given as:

$$\vec{V} \vec{V} = (x_1 + x_2 + x_3)(x_1 + x_2 + x_3)$$

$$\vec{V} \vec{V} = \begin{bmatrix} x_1 x_1 & x_1 x_2 & x_1 x_3 \\ x_2 x_1 & x_2 x_2 & x_2 x_3 \\ x_3 x_1 & x_3 x_2 & x_3 x_3 \end{bmatrix}$$

We have already calculated the values of \vec{V} in the velocity moment calculations and now only need to combine them in the proper combinations to obtain the bulk velocity tensor. The kinetic velocity tensor is given as:

$$\begin{aligned} K_{11} &= m \int f(\vec{v}) v_1 v_1 d\vec{v} & K_{12} &= m \int f(\vec{v}) v_1 v_2 d\vec{v} & K_{13} &= m \int f(\vec{v}) v_1 v_3 d\vec{v} \\ K_{21} &= m \int f(\vec{v}) v_2 v_1 d\vec{v} & K_{22} &= m \int f(\vec{v}) v_2 v_2 d\vec{v} & K_{23} &= m \int f(\vec{v}) v_2 v_3 d\vec{v} \\ K_{31} &= m \int f(\vec{v}) v_3 v_1 d\vec{v} & K_{32} &= m \int f(\vec{v}) v_3 v_2 d\vec{v} & K_{33} &= m \int f(\vec{v}) v_3 v_3 d\vec{v} \end{aligned}$$

Using the relations for the Cartesian components of the velocity given in Equations B.11 through B.13 as well as the substitutions for the velocity differential and the particle flux we write:

$$K_{11} = \frac{(2m)^{1/2}}{\Delta t} \int \frac{C_{ij}}{g_j} \frac{dE_k}{E_k^{1/2}} \sin^3 \alpha \cos^2 \phi d\alpha d\phi \quad (\text{B.24})$$

$$K_{12} = \frac{(2m)^{1/2}}{\Delta t} \int \frac{C_{ij}}{g_j} \frac{dE_k}{E_k^{1/2}} \sin^3 \alpha \cos \phi \sin \phi d\alpha d\phi \quad (\text{B.25})$$

$$K_{13} = \frac{(2m)^{1/2}}{\Delta t} \int \frac{C_{ij}}{g_j} \frac{dE_k}{E_k^{1/2}} \sin^2 \alpha \cos \alpha \sin \phi d\alpha d\phi \quad (\text{B.26})$$

$$K_{21} = \frac{(2m)^{1/2}}{\Delta t} \int \frac{C_{ij}}{g_j} \frac{dE_k}{E_k^{1/2}} \sin^3 \alpha \cos \phi \sin \phi d\alpha d\phi \quad (\text{B.27})$$

$$K_{22} = \frac{(2m)^{1/2}}{\Delta t} \int \frac{C_{ij}}{g_j} \frac{dE_k}{E_k^{1/2}} \sin^3 \alpha \sin^2 \phi d\alpha d\phi \quad (\text{B.28})$$

$$K_{23} = \frac{(2m)^{1/2}}{\Delta t} \int \frac{C_{ij}}{g_j} \frac{dE_k}{E_k^{1/2}} \sin^2 \alpha \cos \alpha \sin \phi d\alpha d\phi \quad (\text{B.29})$$

$$K_{31} = \frac{(2m)^{1/2}}{\Delta t} \int \frac{C_{ij}}{g_j} \frac{dE_k}{E_k^{1/2}} \sin^2 \alpha \cos \alpha \cos \phi d\alpha d\phi \quad (\text{B.30})$$

$$K_{32} = \frac{(2m)^{1/2}}{\Delta t} \int \frac{C_{ij}}{g_j} \frac{dE_k}{E_k^{1/2}} \sin^2 \alpha \cos \alpha \sin \phi d\alpha d\phi \quad (\text{B.31})$$

$$K_{33} = \frac{(2m)^{1/2}}{\Delta t} \int \frac{C_{ij}}{g_j} \frac{dE_k}{E_k^{1/2}} \sin \alpha \cos^2 \alpha d\alpha d\phi \quad (\text{B.32})$$

Now most of the kinetic pressure components have similar integrals so we only have to do some of them. There are six separate integrals over the azimuthal variable ϕ and three separate integrals over the pitch-angle variable α . We do the ϕ integrations first.

Let:

$$\Phi_1 = \int_{\phi - \frac{\Delta\phi}{2}}^{\phi + \frac{\Delta\phi}{2}} \cos^2 \phi d\phi = \frac{1}{2} [\Delta\phi + \cos(2\phi) \sin(\Delta\phi)].$$

$$\Phi_2 = \int_{\phi - \frac{\Delta\phi}{2}}^{\phi + \frac{\Delta\phi}{2}} \cos \phi \sin \phi d\phi = \frac{1}{2} \sin(2\phi) \sin(\Delta\phi).$$

$$\Phi_3 = \int_{\phi - \frac{\Delta\phi}{2}}^{\phi + \frac{\Delta\phi}{2}} \cos \phi d\phi = 2 \cos \phi \sin \left(\frac{\Delta\phi}{2} \right),$$

$$\Phi_4 = \int_{\phi - \frac{\Delta\phi}{2}}^{\phi + \frac{\Delta\phi}{2}} \sin^2 \phi d\phi = \frac{1}{2} [\Delta\phi - \cos(2\phi) \sin(\Delta\phi)],$$

$$\Phi_5 = \int_{\phi - \frac{\Delta\phi}{2}}^{\phi + \frac{\Delta\phi}{2}} \sin \phi d\phi = 2 \sin \phi \sin \left(\frac{\Delta\phi}{2} \right).$$

$$\Phi_6 = \int_{\phi - \frac{\Delta\phi}{2}}^{\phi + \frac{\Delta\phi}{2}} d\phi = \Delta\phi.$$

We do the same thing for the pitch-angle integrals. In this case great effort was made to simplify the resulting expressions so that the least amount of multiplications and additions were used.

Let

$$\lambda_1(\alpha) = \int_{\alpha_1 - \frac{\Delta\alpha}{2}}^{\alpha_1 + \frac{\Delta\alpha}{2}} \sin^3 \alpha d\alpha = \frac{1}{6} [9 \sin(\alpha_1) \sin \left(\frac{\Delta\alpha}{2} \right) - \sin(3\alpha_1) \sin \left(\frac{3\Delta\alpha}{2} \right)].$$

$$\lambda_2(\alpha) = \int_{\alpha_1 - \frac{\Delta\alpha}{2}}^{\alpha_1 + \frac{\Delta\alpha}{2}} \sin^2 \alpha \cos \alpha d\alpha = \frac{1}{6} [3 \cos(\alpha_1) \sin \left(\frac{\Delta\alpha}{2} \right) - \cos(3\alpha_1) \sin \left(\frac{3\Delta\alpha}{2} \right)].$$

$$\lambda_3(\alpha) = \int_{\alpha_1 - \frac{\Delta\alpha}{2}}^{\alpha_1 + \frac{\Delta\alpha}{2}} \cos^2 \alpha \sin \alpha d\alpha = \frac{1}{6} [3 \sin(\alpha_1) \sin \left(\frac{\Delta\alpha}{2} \right) + \sin(3\alpha_1) \sin \left(\frac{3\Delta\alpha}{2} \right)].$$

Changing the integration over energy into a summation over energy and pitch-angle and using the above substitutions we now rewrite Equations B.24 – B.32

as:

$$K_{11} = \frac{(2m)^{1/2}}{\Delta t} \sum_{jk} \frac{C_{ij}}{g_j} \frac{dE_k}{E_k^{1/2}} \lambda_1(\alpha) \Phi_1, \quad (\text{B.33})$$

$$K_{12} = \frac{(2m)^{1/2}}{\Delta t} \sum_{jk} \frac{C_{ij}}{g_j} \frac{dE_k}{E_k^{1/2}} \lambda_1(\alpha) \Phi_2, \quad (\text{B.34})$$

$$K_{13} = \frac{(2m)^{1/2}}{\Delta t} \sum_{jk} \frac{C_{ij}}{g_j} \frac{dE_k}{E_k^{1/2}} \lambda_2(\alpha) \Phi_3, \quad (\text{B.35})$$

$$K_{21} = \frac{(2m)^{1/2}}{\Delta t} \sum_{jk} \frac{C_{ij}}{g_j} \frac{dE_k}{E_k^{1/2}} \lambda_1(\alpha) \Phi_2. \quad (\text{B.36})$$

$$K_{22} = \frac{(2m)^{1/2}}{\Delta t} \sum_{jk} \frac{C_{ij}}{g_j} \frac{dE_k}{E_k^{1/2}} \lambda_1(\alpha) \Phi_4, \quad (\text{B.37})$$

$$K_{23} = \frac{(2m)^{1/2}}{\Delta t} \sum_{jk} \frac{C_{ij}}{g_j} \frac{dE_k}{E_k^{1/2}} \lambda_2(\alpha) \Phi_5. \quad (\text{B.38})$$

$$K_{31} = \frac{(2m)^{1/2}}{\Delta t} \sum_{jk} \frac{C_{ij}}{g_j} \frac{dE_k}{E_k^{1/2}} \lambda_2(\alpha) \Phi_3. \quad (\text{B.39})$$

$$K_{32} = \frac{(2m)^{1/2}}{\Delta t} \sum_{jk} \frac{C_{ij}}{g_j} \frac{dE_k}{E_k^{1/2}} \lambda_2(\alpha) \Phi_5. \quad (\text{B.40})$$

$$K_{33} = \frac{(2m)^{1/2}}{\Delta t} \sum_{jk} \frac{C_{ij}}{g_j} \frac{dE_k}{E_k^{1/2}} \lambda_3(\alpha) \Phi_6. \quad (\text{B.41})$$

This can be written more compactly as:

$$\bar{\bar{K}} = \frac{(2m)^{1/2}}{\Delta t} \sum_{jk} \frac{C_{ij}}{g_j} \frac{dE_k}{E_k^{1/2}} \begin{bmatrix} \lambda_1(\alpha) \Phi_1 & \lambda_1(\alpha) \Phi_2 & \lambda_2(\alpha) \Phi_3 \\ \lambda_1(\alpha) \Phi_2 & \lambda_1(\alpha) \Phi_4 & \lambda_2(\alpha) \Phi_5 \\ \lambda_2(\alpha) \Phi_3 & \lambda_2(\alpha) \Phi_5 & \lambda_3(\alpha) \Phi_6 \end{bmatrix}$$

Knowing the pressure one can now determine the temperature of the distribution function. The temperature is defined as:

$$\text{Temperature} = \frac{1}{3n} \text{Tr}(P)$$

where $\text{Tr}(P)$ is the trace of the pressure tensor. There are of course higher order

moments that can be calculated but it becomes more difficult to attach physical meaning to them, so we will stop here after the second order moment.

Appendix C

SOLID STATE TELESCOPE ELECTRONICS

This appendix explains in greater detail how the collision of an electron with a piece of silicon was changed into a count that was recorded on the ground and finally gave us information about how pulsating auroras are generated. The workings of the silicon detector were covered in Chapter 2, but further clarifications will explain why the solid state telescopes detected the energies I have reported.

The basic chain of action is as follows. The electron collides with the silicon wafer in the front of the detector. This causes a current to be set up, with current size being related to the energy of the electron that impacted. This current is changed into a voltage and amplified in the preamp. The voltage output of the preamp is sent to a peak hold and detect (PH) board where the pulse is shaped and spread out so that the next board, the analog-to-digital converter (ADC) can change the analog pulse into a digital signal.

Once the signal is in digital format it is counted and directed into separate energy bins. This information is sent to another board which was able to handle three different detector outputs. The signal was then sent to a slave digital processing unit (DPU), which communicated with the master DPU, which made a signal that could be sent to the ground by the NASA telemetry.

The signal from the detector was in the form of a current. This current is sent

to the preamp where it is converted into a voltage. Table C shows the gain of the preamp boards for the different detectors.

Table C.1: The solid state telescope preamp charge gain in volts per picoColumb

Detector (degrees)	Gain (V/pC)
0 electron	0.90
22.5	0.81
45.0	0.74
67.5	0.92
90.0	0.86
0 proton	0.90

Once the current was converted into a voltage the signal was sent to the peak hold boards. The information carried by the signal is the height of the voltage, which indicates the energy of the particular electron that has been detected and rapidity with which the signal is repeated which indicates when the electrons are detected.

A brief explanation about dead time is required to explain some of the counting limitations of the instrument. If an electron hit the silicon wafer too quickly behind the previous one then the second electron would not be counted. For instance, if two electrons hit within 1 picosecond of each other only a single count would be recorded. This is an example of the solid state telescope dead time. By dead time we mean that the detector is unable to count electrons. It is as if it were dead.

After the voltage signal had gone from the preamps to the peak hold boards

many things were done to it. This is because the analog signal was not in a form conducive to digital conversion. The peak hold board was responsible for making the analog signal into one that could be converted accurately into a digital one. The peak hold board amplified the signal and shaped it into one that was flat topped and steeply rising. It was this signal form that could be easily and accurately converted into a digital format.

Also on the peak hold board the high and low energy levels were set. The peak hold board rejected any signal coming from the preamps that was below a certain voltage, thereby setting the low energy level. Any signal above a certain value was also rejected. This high level voltage was set by the requirements of the ADC we were using.

The gains of the peak hold boards set the energy range that the instrument was capable of detecting. If the gain is low then the instrument can see higher energies because it takes higher energies to get to the high level cutoff. If the gain is high then the instrument is unable to see to higher energies. So depending on the particular gain of the instrument a different energy range is measured.

So far we have been discussing the energy or voltage response of the peak hold boards but they also process signals as a function of time. The ADC requires that each signal it converts be of a certain duration. If a signal is too short the ADC cannot convert it. So in the interest of measuring the environment as completely as possible we want to send the shortest readable signal to ADC as possible.

This is another example of instrument dead time which is separate from the one discussed earlier but which also results in electrons not being counted. The duration or length in time of a countable signal was on the order of 1 to 10 mi-

croseconds. Thus, a single detector could not count more than approximately 100 thousand counts per second.

So far we have explained how the energy ranges were set for each of the solid state telescopes. We still haven't explained the energy bins for each of the detectors. The detectors are capable of detecting a continuous range of energies. If an electron of 41.23 keV were to hit the detector it would create a detectable signal, likewise an electron of 41.33 keV would also produce a detectable signal. The electronics have enough noise and uncertainty that they are unable to distinguish between such a small energy difference but both electrons would create a unique signal.

So the detectors can put out a signal of any voltage and we had to determine how we were going to convert this signal into meaningful science. Here is where the limitations, or capabilities, of the ADC come into play. We used a 12 bit ADC, but we only looked at the 8 most significant bits. In this way we ignored the noisy fluctuations of the signal and lost the ability to distinguish between a 41.23 keV electron and a 41.33 keV electron. The actual energy measurement ability of each instrument was exhaustively investigated and most of the instruments were able to distinguish energies that were separated by approximately 7 keV at full width half max (FWHM). The end result is that an electron of 25 keV is indistinguishable from one of 26 keV.

Aside from the intrinsic ability of the ADC to convert signals, the telemetry limitations also played a role in determining the energy bins of the detectors. From other observations of pulsating aurora we knew that most of the particle precipitation occurred in energies that were below the detection capability of the solid state telescopes. We figured that the flux at the higher energies, say above 100 keV, would be quite small. So we made bin widths that increased in

size as the energy of the electron increased. So the width of the energy bin at 200 keV was 13 keV rather than the instrument limitation of 7 keV.

Another factor that helped to determine the energies that went into a particular bin is that we made the number of counts a single bin could hold vary with the energy of the bin. This means that bins at higher energies had smaller sizes, *i.e.* they could hold less counts. This is okay since we were pretty certain that the higher energies would have less counts.

Finally, all of this playing around with how many counts could be held in a single bin helped to determine the geometric factor of the instruments. If we set the telemetry but allowed the detectors to collect huge amounts of particles then we would be saturated for most of the time. Likewise if the counts we received were too small the intrinsic uncertainty of the measurement starts to get more and more important, this is where statistics come into play. We want the instrument to be detecting counts in the middle of its range of ability. That way a sudden decrease or increase would be easily visible.

All of these requirements seem to pull the instrument in too many directions. Too many counts or not enough, big energy ranges or small, small energy bins or large. It is a delicate balance in the end and it often amazes me that space instruments can work at all. Since we do not know a priori what we will be measuring we just make a best guess at what will be seen and try to keep enough flexibility to be able to see something if we have guessed incorrectly.

Finally I reproduce here the energy ranges and geometric factors of all of the solid state telescopes.

Table C.2: 0° detector energy bin setup. Geometric factor = 0.0211 cm² sr.

Channel Number	Low Energy (keV)	Center Energy (keV)	High Energy (keV)	Energy Bin Width (keV)
1	22.332	24.115	25.897	3.565
2	27.747	29.597	31.447	3.700
3	33.296	36.071	38.846	5.549
4	40.696	42.545	44.395	3.700
5	46.245	49.020	51.794	5.549
6	53.644	56.419	59.194	5.549
7	61.043	64.743	68.443	7.399
8	70.292	73.992	77.692	7.399
9	79.541	83.241	86.941	7.399
10	88.791	93.415	98.040	9.249
11	99.889	104.51	109.14	9.249
12	110.99	115.61	120.24	9.249
13	122.09	127.64	133.19	11.10
14	135.04	140.59	146.13	11.10
15	147.98	153.53	159.08	11.10
16	160.93	167.41	173.88	12.95
17	175.73	183.13	190.53	14.80
18	192.38	198.85	205.33	12.95
19	207.18	214.58	221.98	14.80
20	223.83	231.23	238.62	14.80
21	240.47	248.80	257.12	16.65
22	258.97	267.30	275.62	16.65
23	277.47	285.79	294.12	16.65
24	295.97	305.22	314.47	18.50
25	316.31	325.57	334.81	18.50
25	336.66	345.91	355.16	18.50
27	357.01	367.19	377.36	20.35
28	379.21	389.38	399.56	20.35

Table C.3: 22.5° detector energy bin setup. Geometric factor = 0.0211 cm² sr.

Channel Number	Low Energy (keV)	Center Energy (keV)	High Energy (keV)	Energy Bin Width (keV)
1	24.160	25.490	26.819	2.660
2	28.735	30.651	32.566	3.831
3	34.482	37.356	40.229	5.747
4	42.145	44.061	45.976	3.831
5	47.892	50.765	53.639	5.747
6	55.555	58.428	61.302	5.747
7	63.217	67.049	70.880	7.663
8	72.796	76.627	80.458	7.663
9	82.374	86.205	90.037	7.663
10	91.952	96.742	101.53	9.578
11	103.45	108.24	113.03	9.578
12	114.94	119.73	124.52	9.578
13	126.44	132.18	137.93	11.45
14	139.84	145.59	151.34	11.45
15	153.25	159.00	164.75	11.45
16	166.66	173.37	180.07	13.41
17	181.99	189.65	197.32	15.33
18	199.23	205.94	212.64	13.41
19	214.56	222.22	229.88	15.33
20	231.80	239.46	247.12	15.33
21	249.04	257.66	266.28	17.24
22	268.20	276.82	285.44	17.24
23	287.35	295.97	304.59	17.24
24	306.51	316.09	325.67	19.16
25	327.58	337.16	346.74	19.16
26	348.65	358.23	367.81	19.16
27	369.73	380.26	390.80	21.07
28	392.71	403.25	413.79	21.07

Table C.4: 45° detector energy bin setup. Geometric factor = 0.0156 cm² sr.

Channel Number	Low Energy (keV)	Center Energy (keV)	High Energy (keV)	Energy Bin Width (keV)
1	20.241	21.854	23.466	3.224
2	25.142	26.818	28.494	3.352
3	30.170	32.685	35.199	5.028
4	36.875	38.551	40.227	3.352
5	41.903	44.418	46.932	5.028
6	48.608	51.122	53.636	5.028
7	55.312	58.665	62.017	6.705
8	63.693	67.045	70.398	6.705
9	72.074	75.426	78.778	6.705
10	80.455	84.645	88.835	8.381
11	90.511	94.702	98.892	8.381
12	100.57	104.76	108.95	8.381
13	110.63	115.65	120.68	10.06
14	122.36	127.39	132.42	10.06
15	134.09	139.12	144.15	10.06
16	145.82	151.69	157.56	11.73
17	159.23	165.94	172.64	13.41
18	174.32	180.19	186.05	11.73
19	187.73	194.43	201.14	13.41
20	202.81	209.52	216.22	13.41
21	217.90	225.44	232.98	15.09
22	234.66	242.20	249.74	15.09
23	251.42	258.96	266.51	15.09
24	268.18	276.56	284.94	16.76
25	286.62	295.00	303.38	16.76
26	305.06	313.44	321.82	16.76
27	323.49	332.71	341.93	18.44
28	343.61	352.83	362.05	18.44

Table C.5: 67.5° detector energy bin setup. Geometric factor = 0.0143 cm² sr.

Channel Number	Low Energy (keV)	Center Energy (keV)	High Energy (keV)	Energy Bin Width (keV)
1	22.139	24.483	26.826	4.687
2	28.742	30.658	32.574	3.832
3	34.491	37.365	40.239	5.748
4	42.155	44.071	45.987	3.832
5	47.904	50.778	53.652	5.748
6	55.568	58.442	61.317	5.748
7	63.233	67.065	70.897	7.665
8	72.813	76.646	80.478	7.665
9	82.394	86.226	90.059	7.665
10	91.975	96.765	101.56	9.581
11	103.47	108.26	113.05	9.581
12	114.97	119.76	124.55	9.581
13	126.47	132.21	137.96	11.50
14	139.88	145.63	151.38	11.50
15	153.29	159.04	164.79	11.50
16	166.71	173.41	180.12	13.41
17	182.03	189.70	197.36	15.33
18	199.28	205.99	212.69	13.41
19	214.61	222.27	229.94	15.33
20	231.85	239.52	247.18	15.33
21	249.10	257.72	266.34	17.25
22	268.26	276.88	285.51	17.25
23	287.42	296.04	304.67	17.25
24	306.58	316.16	325.75	19.16
25	327.66	337.24	346.82	19.16
26	348.74	358.32	367.90	19.16
27	369.82	380.36	390.89	21.08
28	392.81	403.35	413.89	21.08

Table C.6: 90° detector energy bin setup. Geometric factor = 0.0145 cm² sr.

Channel Number	Low Energy (keV)	Center Energy (keV)	High Energy (keV)	Energy Bin Width (keV)
1	22.377	24.292	26.206	3.829
2	28.078	29.950	31.822	3.744
3	33.694	36.502	39.310	5.616
4	41.182	43.053	44.925	3.744
5	46.797	49.605	52.413	5.616
6	54.285	57.093	59.900	5.616
7	61.772	65.516	69.260	7.488
8	71.132	74.875	78.619	7.488
9	80.491	84.235	87.979	7.488
10	89.851	94.530	99.210	9.359
11	101.08	105.76	110.44	9.359
12	112.31	116.99	121.67	9.359
13	123.55	129.16	134.78	11.23
14	136.65	142.26	147.88	11.23
15	149.75	155.37	160.98	11.23
16	162.85	169.41	175.96	13.10
17	177.83	185.32	192.80	14.98
18	194.68	201.23	207.78	13.10
19	209.65	217.14	224.63	14.98
20	226.50	233.99	241.47	14.98
21	243.35	251.77	260.19	16.85
22	262.06	270.49	278.91	16.85
23	280.78	289.21	297.63	16.85
24	299.50	308.86	318.22	18.72
25	320.09	329.45	338.81	18.72
26	340.68	350.04	359.40	18.72
27	361.27	371.57	381.87	20.59
28	383.74	394.03	404.33	20.59

Table C.7: Proton detector energy bin setup. Geometric factor = 0.98 cm² sr.

Channel Number	Low Energy (keV)	Center Energy (keV)	High Energy (keV)	Energy Bin Width (keV)
1	114.96	116.20	117.44	2.483
2	119.40	121.36	123.32	3.920
3	125.28	128.22	131.16	5.880
4	133.12	135.08	137.04	3.920
5	139.00	141.94	144.88	5.880
6	146.84	149.78	152.72	5.880
7	154.68	158.60	162.52	7.840
8	164.48	168.40	172.33	7.840
9	174.29	178.21	182.13	7.840
10	184.09	188.99	193.89	9.801
11	195.84	200.75	205.65	9.801
12	207.61	212.51	217.41	9.801
13	219.37	225.25	231.13	11.76
14	233.09	238.97	244.85	11.76
15	246.81	252.69	258.57	11.76
16	260.53	267.39	274.25	13.72
17	276.21	284.05	291.89	15.68
18	293.85	300.71	307.57	13.72
19	309.53	317.37	325.21	15.68
20	327.17	335.01	342.85	15.68
21	344.81	353.64	362.46	17.64
22	364.42	373.24	382.06	17.64
23	384.02	392.84	401.66	17.64
24	403.62	413.42	423.22	19.60
25	425.18	434.98	444.78	19.60
26	446.74	456.54	466.34	19.60
27	468.30	479.08	489.86	21.56
28	491.82	502.60	513.38	21.56

Appendix D

TEMPORAL VERSUS SPATIAL DYNAMICS

In order to determine whether the rocket measurements were spatial or temporal, the electron precipitation was compared with the optical intensity measured by the all-sky cameras at Poker Flat and Fort Yukon. While these instruments cannot directly measure the electron precipitation it has been shown that electron precipitation is closely tied to the changes in optical brightness [Yau *et al.*, 1981; McEwen *et al.*, 1981] as measured by all-sky cameras.

The method is to find the position of the rocket in the field of view of the all-sky camera. This is accomplished by mapping the rocket's position in space down to 100 km using a dipole magnetic field model. Once the position has been found, the optical brightness from a group of pixels surrounding the point is averaged together with the result becoming a single point in a time series. As the rocket traverses across the field of view a series of brightness measurements is built up. Since the cameras are looking at a single point in space, each measurement consists of temporal changes. The next step is to compare this temporal measurement to the measurements returned by the rocket. If the rocket and the all-sky measurements are similar then we assume that the measurements returned by the rocket are temporal in nature and not spatial.

Figure D.1 shows a time series of the optical brightness from the all-sky cameras from Poker Flat and Fort Yukon as well the downgoing electron measure-

ments returned from the rocket. Because the rocket spent much of the flight time in view of the Fort Yukon camera the correlation between the Fort Yukon measurements and the electron measurements is excellent. Not only do the gross features match up but also some of the smaller substructures appear in both measurements. This correlation leads us to conclude that the measurements made by the rocket can be considered to be temporal in nature.

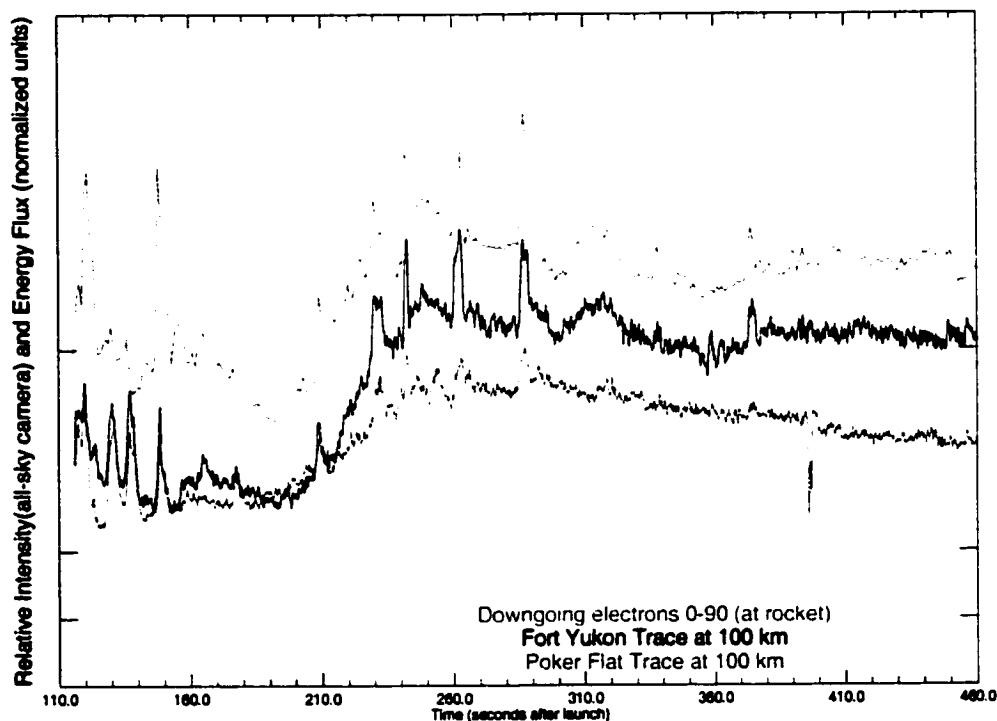


Figure D.1: The optical signatures of the all-sky cameras from Fort Yukon and Poker Flat with the electron flux as measured on board the rocket for the entire rocket flight. The rocket spent much of its flight time within view of the Fort Yukon all-sky camera. The correlation between the optical and flux signatures indicates that the rocket observed temporal electron precipitation.

Appendix E

X-RAYS PRODUCED BY BREMSSTRAHLUNG

In order to be certain that the low energy electrons observed during pulsation events are real we checked that X-rays were not responsible for the observed counts. The following appendix gives details on how we made certain that the counts we measured in the low energy channels were really due to electrons and not X-rays.

The hemispheres in front of the electrostatic analyser are used to steer electrons of a specific energy range onto the microchannel plates; as well as to reject positively charged and neutral particles. X-rays, which have no charge, are capable of penetrating through the hemispheres, colliding with the microchannel plates and being recorded as legitimate counts. These X-rays (bremsstrahlung) are produced when high energy (> 1 keV) electrons collide with any of the aluminum parts of the rocket body.

In order to estimate the number of counts that are actually produced by X-rays a calculation of X-ray flux is made. Given the complexity of the geometry of the rocket instruments and housing as well as the uncertainty in the number of X-rays that will actually make it to the microchannel plates a number of simplifications were made. The production of X-rays by the collision of energetic electrons with a target is a product of the flux of the incoming electrons, the collision cross section of those electrons with aluminum and the number of

scattering centers on the rocket body. After these X-rays have been produced they have to travel through some unknown thickness of aluminum, therefore, also included in the calculation is an attenuation factor, $A(E_\gamma)$. This entire process must be integrated over the energy range of the electrons which may produce X-rays as well as the energy range of the produced X-rays. We can write the above description as:

$$N = \int_{E_\gamma=1}^{E_\gamma=60} \int_{E_e=0}^{E_e=\infty} \Delta f(E_e) \cdot N \sigma_B(E_\gamma, E_e) \cdot A(E_\gamma) dE_e dE_\gamma$$

As an example, a 60 keV electron can produce X-rays that continuously ranges from 60 keV down to approximately 1 keV. The range of X-rays which can be produced has a lower limit of approximately 1 keV because lower energy X-rays cannot make it through the aluminum shielding around the instrument body. The variable $\Delta f(E_e)$ is the change in electron flux produced during a pulsation event. We are interested in the change in flux because we can assume that X-rays are constantly bombarding the instrument and producing a steady background count. It is the increased flux during a pulsation that may be able to produce extra X-ray counts that we need to account for. The cross section, $\sigma_B(E_\gamma, E_e)$ is the described in lecture notes from Enrico Fermi [Orear *et al.*, 1949]. The number of scattering centers, N , increases with increasing electron impact energy but for this calculation we assume that the number of scattering centers remains independent of the electron energy. Since we are only interested in the change in electron flux the range of integration for the electron energy is governed by the range of energies in which pulsations were observed, thus we change the upper integration limit from infinite energy down to 60 keV.

Of all of these factors the one that is least known is the number of scattering centers or target atoms. This is because of the odd shape of the rocket body

and the metal surrounding the instrument. All of the metal parts from the rocket body produce X-rays and some fraction of those can reach the detector. In order to make a reasonable estimate of this quantity we assume that the surface area of the X-ray emitting region is equivalent to the surface area of the detector directly underneath the metal hemispheres of the instrument. It can be shown that the flux of X-rays on a small area element dA from a surface that is infinite in extent is π times larger than the flux of X-rays from a limited but unknown surface area such as we have on the rocket body. Thus we assume that the X-ray producing area is infinite in extent, thereby overestimating the total flux of X-rays produced by bremsstrahlung.

The attenuation of X-rays through matter follows an exponential decay law and can be written as:

$$I = I_0 \exp^{-\mu x}$$

where I is the flux leaving the aluminum, I_0 is the flux entering the aluminum, μ is the energy dependent mass absorption coefficient and x is the distance traveled through the aluminum. Roughly the greatest attenuation occurs for X-rays that have the lowest energy. We can write the attenuation as $A = I/I_0$

For every instance in which a simplification was made the choice was governed by which would produce the most X-rays. In this way we get an overestimate of the X-ray production. Our results indicate that no more than 10% of the flux in the low energy channels can be accounted for by the production of bremsstrahlung. Given that the change in the flux at these low energies is greater than 10% we have concluded that the counts appearing in the low energy channels are indeed due to the presence of low energy electrons.

Appendix F

LOCAL PRODUCTION OF ELECTRONS

Having made certain that the flux is really electrons we now ask where the electrons may have been produced. It is possible that the low energy electrons were produced in the ionosphere at and above the height of the rocket. If this occurred then the low energy pulsation signatures would be explained as a collision phenomena which leads to no new insight into the physics of pulsating aurora. In order to decide whether or not the low energy electrons were produced via collisions above the rocket an electron transport model was used. The model code was written by Dr. Laura Peticolas and Dr. Dirk Lummerzheim. The transport model[Lummerzheim *et al.*, 1989; Lummerzheim and Lilensten, 1994] comprised a time stationary solution to the Boltzmann equation and took into account major as well as minor species, elastic and inelastic collision cross-sections and incorporated pitch angle and energy information into the solution.

Input model parameters accounted for a normal MSIS (Mass Spectrometer and Incoherent Scatter) Oxygen scale height, a low f10.7 flux($f = 73.3 \times 10^{-22}$ Watts $m^{-2} Hz^{-1}$) as well as low A_p index ($A_p = 12$), the values of which were obtained from published reports. The model runs performed also had as input the energy spectra obtained from the rocket data. Specifically the model used a 5 keV Maxwellian as the particle flux into the ionosphere. The rocket data itself was well modeled as a 5 keV Maxwellian. These electrons were started from a height of 1000 km, well above any collision dominated region, and allowed to

move into the ionosphere. At the various rocket altitudes the particle flux for energies ranging between 0.1 eV and 10 keV is obtained and compared to the observations made on the rocket.

Figure F.1 shows the model results obtained at 380 km. We are interested in comparing the flux of electrons in the downward direction at energies between 10 eV and 200 eV with the measured flux of electrons at these same energies. If the model results show a smaller amount of flux at these energies then we may assume that the low energy electrons measured at the rocket cannot be produced solely via collisional processes above and at the height of the rocket. Figure F.2 shows the observations made on the rocket at the same height of 380 km. Comparison of the two figures shows that the model predicts a much lower amount of flux than is observed at the rocket. In some energies this difference is an order of magnitude. These results show that it is very unlikely that the low energy electrons measured at the rocket were produced via collisional processes at or above the rocket.

It is possible that if the ionosphere were heated then the upgoing flux might be equal to that measured by the rocket. A further model run with inputs of $A_p = 200$, an f10.7 flux of $f = 73.3 \times 10^{-22} \text{ Watts m}^{-2} \text{ Hz}^{-1}$ and an inflated MSIS O scale height showed results similar but not exactly like the rocket observations. These input parameters do not accurately reflect the geophysical conditions during the rocket flight but do offer an explanation as to what might cause the upward and downward particle flux to be similar.

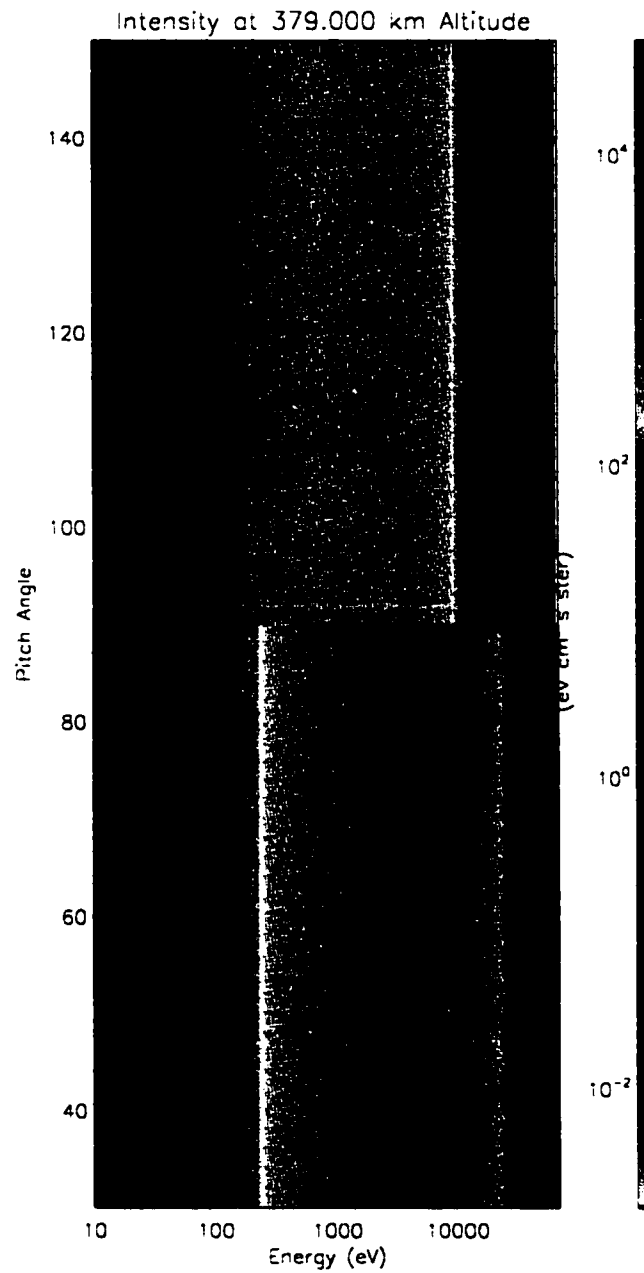


Figure F.1: Model predictions of the downward particle flux as a function of pitch angle and energy at 379 km. This input spectra is obvious as the band of flux centered at 5 keV on the downward portion of the plot.

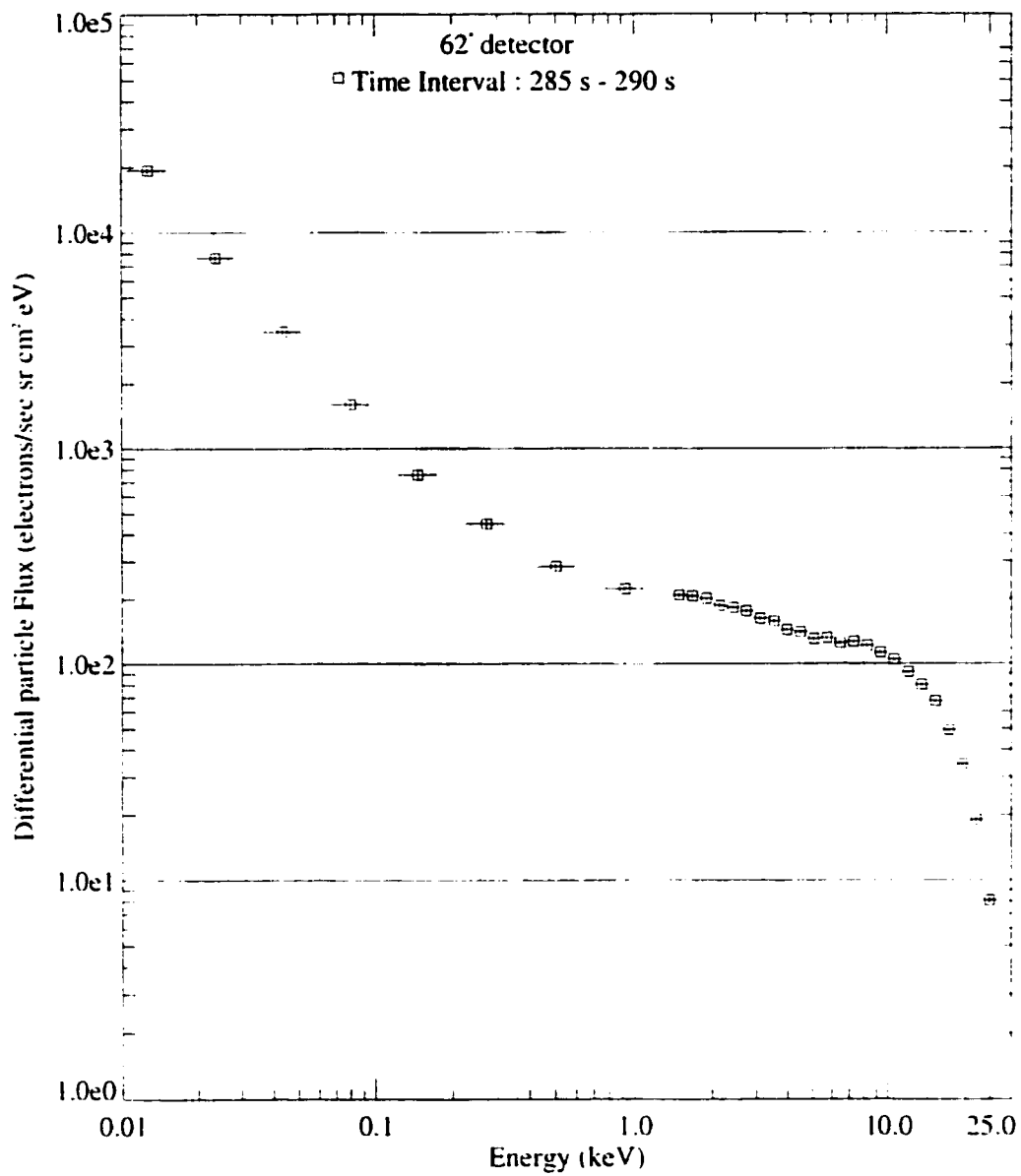


Figure F.2: Measured downward particle flux as a function of energy at 379 km.

INDEX

- Fort Yukon, 32
- Auroral breakup, 1
- Bryant, Duncan, 9
- Canadian Auroral Rocket Campaign,
4
- Conduction band, 22
- Coroniti, Ferd, 12
- Counting efficiency, 19
- Cyclotron frequency
 - electron, 85
- Davidson, Gerald, 13
- Dead time, 20
- Electron cyclotron dispersion relation,
84
- Electron cyclotron waves, 81
- Electrostatic analyzer
 - concentric hemispheres, 30
 - Electric field, 26
 - field of view, 25
 - microchannel plates, 26
 - sample time, 25
 - slit opening, 30
- Evans, Dave, 47
- Fermi, Enrico, 148
- Geometric factor, 109
- Hallinan, Tom, 96
- Kennel, Charles, 10
- Lorentz force, 21
- Ni-63, 27
- Nielsen, Hans, 96
- Pitch-angle, 6
- Plasma frequency
 - electron, 84
- Poker Flat Research Range, 16, 32
- POLAR spacecraft, 32
- Pulsating aurora
 - 3 Hz Modulation, 2, 7, 75
 - Characteristic energy, 3
 - Emission height, 3
 - Emission thickness, 3
 - Energy spectra, 5
 - Length of event, 3
 - Occurrence times, 3
 - Optical Observations, 4
 - Optical observations, 2
 - Period, 2

- Pitch-angle distributions, 6
- Rocket observations, 4–10
- Theoretical models, 10
 - Coroniti and Kennel, 12
 - Cyclotron maser, 13
 - Relaxation oscillator, 13
- Velocity Dispersion, 8

- Solid state telescopes, 109
 - ADC, 24
 - dead time, 22
 - DPU, 24
 - field of view, 23
 - geometric factor, 117
 - integral counter, 23
 - peak hold board, 23
 - power supply, 23
 - preamp, 23
 - sample time, 23

- Transverse resonance condition, 85

- Ultraviolet Imager, 32

- Whistler mode waves, *see* Electron
cyclotron waves

VITA

John Denis Williams was born on March 13, 1966, in Brooklyn, New York to John Michael and Anna Patricia Williams. John graduated from Morris Knolls Regional High School in 1984, and received a Bachelor of Science in physics from State University of New York at Albany in 1990. John attended the University of Alaska in Fairbanks in 1991 and received a Master of Science degree in Physics in 1995. From 1995 to 2002 John was a student at the University of Washington in the Geophysics Program studying matters related to outer space.